# TRINUCLEAR METAL CHALCOGENIDE CLUSTERS AS PRECURSORS FOR SUPERATOMIC SOLIDS AND CLUSTER ORGANIC FRAMEWORKS

by

Jessica Lauren Shott

A thesis submitted to the faculty of
The University of North Carolina at Charlotte
in partial fulfillment of the requirements
for the degree of Master of Science in
Chemistry

Charlotte

2017

Approved by:

_____
Dr. Christopher M. Bejger

_____
Dr. Daniel Rabinovich

_____
Dr. Michael G. Walter

_____
Dr. Yong Zhang

# ABSTRACT

JESSICA LAUREN SHOTT. Trinuclear metal chalcogenide clusters as precursors for superatomic solids and cluster organic frameworks (Under the direction of DR. CHRISTOPHER M. BEJGER)

Inorganic molecular clusters $Ni_3(\mu_3\text{-}I)_2(\mu_2\text{-}dppm)_3$ (**1**), $Ni_3(\mu_3\text{-}Te)_2(\mu_2\text{-}dppm)_3$ (**2**), $Ni_3(\mu_3\text{-}Se)_2(\mu_2\text{-}dppm)_3$ (**3**), $Ni_3(\mu_3\text{-}S)_2(\mu_2\text{-}dppm)_3$ (**4**), $Co_4(\mu_3\text{-}S)_4(PPr^i_3)_4$ (**5**), and $Mo_3(\mu_3\text{-}S)_2(\mu_2\text{-}S)_3(PMe_3)_6$ (**6**) have been used as building block precursors in the formation of binary superatomic solids with fullerenes (**1-6**•$C_{60}$). These solids are crystallized from solution and charge transfer from the electron-rich molecular cluster precursors to fullerene was confirmed using infrared (IR) spectroscopy. Structural data for these superatomic solids was obtained using single-crystal X-ray diffraction (XRD) experiments and suggests that their assembly is directed by noncovalent interactions. Close-contacts, reminiscent of halogen bonds, between cluster capping ligands and fulleride anions are observed in the solid state. Superconducting quantum interference device (SQUID) magnetometry and two-probe conductivity measurements indicate that compounds **1**•$C_{60}$ and **2**•$C_{60}$ are paramagnetic and one hundred times more conductive than the constituent cluster precursors.

Additionally, derivatives of molecular clusters **5** and **6** have been synthesized and investigated for use as superatomic secondary building units for 2D and 3D cluster organic frameworks. Characterization of these novel building blocks was accomplished using NMR spectroscopy as well as matrix-assisted laser desorption ionization mass spectrometry (MALDI-MS) and XRD analysis.

# ACKNOWLEDGEMENTS

First and foremost, I would like to thank my advisor, Dr. Christopher Bejger, for allowing me to join his research group. Working in his laboratory provided me with the valuable opportunity to experience laboratory set-up firsthand and enabled me to utilize the skills I had gained during my undergraduate career for an entirely new purpose. Thanks for supporting me in all of my research endeavors. Your unwavering belief in me was invaluable during times of self-doubt or bouts of nerves before big presentations. Thank you for taking time out of your weekends and evenings to help me practice and revise all of my presentations and for being patient with me during the times I was resistant to change. Thank you for teaching me to be calm under pressure. Most of all, thank you for your advice and encouragement especially during this time of transition. I feel that I have grown so much during my time in your laboratory and feel that other graduate students would be lucky to have the opportunity to work on such unique synthetic projects under such a supportive advisor. I am positive your laboratory will continue to grow and advance and I look forward to seeing what amazing chemical contributions you make in the future!

I would also like to thank my coworkers in the Bejger Lab: Marshall, for his words of wisdom; Matt, for his amazing recrystallization skills; Abdul, for always coming in with a smile; and James, for optimizing our cluster syntheses.

I absolutely need to thank Nemah and Dr. Dan Jones for running all of our single crystal X-ray diffraction experiments. Additionally, I would like to thank Dr. Daniel Paley at Columbia University for taking the time to refine our fullerene structures and Dr.

David Shultz at North Carolina State University for allowing us to use his instrumentation to collect magnetic data on our samples. Thank you to Dr. Rabinovich, Dr. Walter, and Dr. Zhang for agreeing to be members of my thesis committee. Your advice and expertise has been instrumental to the success of this work.

I would like to send an enormous thank you to Dr. Walsh for providing the funding for the Thomas D. Walsh Graduate Research Fellowship. His generous contributions have supported me during my time here and allowed me to focus solely on my research, providing me with more opportunities to grow as a chemist and as a professional.

Furthermore, I would like to express my gratitude toward everyone in the UNC Charlotte Department of Chemistry for being so welcoming when I first arrived and for being so helpful throughout my time here. Specifically, I would like to thank Jerrod for keeping me sane and for making North Carolina feel more like home. I came to Charlotte only to study chemistry but am leaving with a good friend and for that I will always be thankful. I would also like to thank Ashley for being a great friend while keeping me balanced and active by attending classes at the gym with me multiple times a week. Zach and Adam: thank you for being the best lab neighbors a chemist could ask for. Not only were you always willing to lend a helping hand, but you also brightened each day by stopping by to say hello. I would also like to thank Richard for being so welcoming and for showing me all of the fun places worth visiting around Charlotte.

I would be remiss if I did not give thanks to my undergraduate research advisor at James Madison University, Dr. Brycelyn Boardman. It is from her that I inherited my special brand of poster and presentation OCD and, while it sounds like a nightmare, those

presentation skills have proved to be the most valuable lesson I learned at JMU. B taught me that presentations should be fun, colorful, creative, and full of smiles. She taught me to love chemistry, love my research, and love sharing it with others. So, thank you for teaching me how to be a chemist and being the best role model I could have asked for. Thank you for always pushing me. Thank you for teaching me to make my own decisions and trust my intuition. Mostly, thank you for giving me the confidence to be my awkwardly charming self! B, I absolutely would not be where I am today without you.

Additionally, I would like to thank my family for their constant love and support. It is what has gotten me through many long nights and failed experiments. To my mother and father, thank you for being two of the smartest, hardest working people I know. You have always encouraged me to pursue my dreams, no matter what they are. You both make me proud every day and I work every day to try to do the same for you. To Cati, thank you for being my older sister, my best friend, and for making me smile at least once a day. I have wanted to be just like you since I was three, so thank you for being the cool older sister that everybody wants but few are lucky enough to have. Thank you Grandie for being the most inspirationally stubborn woman on the planet and Pappy for teaching me from a young age that not all intelligence comes from a book.

Finally, I would like to thank John. Thank you for being my rock, keeping me calm, and supporting me constantly. Thank you for encouraging to pursue this degree and for listening to me vent my frustrations from nearly 400 miles away. You make me feel like I can do anything. You are the light at the end of the tunnel. You are my family, my heart, and my home and I cannot wait to start the next chapter of my life with you.

TABLE OF CONTENTS

LIST OF FIGURES ..... xi

LIST OF SCHEMES ..... xvi

LIST OF EQUATIONS ..... xvii

LIST OF ABBREVIATIONS ..... xviii

CHAPTER 1: TRINUCLEAR METAL CHALCOGENIDE CLUSTERS FOR SUPERATOMIC SOLIDS ..... 1

1.1 Introduction ..... 1

1.1.1 Hierarchical Design ..... 1

1.1.2 Metal Clusters as Building Blocks ..... 6

1.1.3 Fulleride-based Self-Assembled Materials ..... 12

1.1.4 Research Objectives ..... 15

1.2 Results and Discussion ..... 20

1.2.1 Synthesis and Structural Characterization of **1**•$C_{60}$ ..... 20

1.2.2 Synthesis and Structural Characterization of **2**•$C_{60}$ ..... 24

1.2.3 Structural Characterization of **1**•$C_{70}$ and **2**•$C_{70}$ ..... 26

1.2.4 Structural Characterization of 3•$C_{60}$ ..... 27

1.2.5 Synthesis and Structural Characterization of **4**•$C_{60}$ ..... 29

1.2.6 Attempted Synthesis of **5**•$C_{60}$ ..... 31

1.2.7 Structural Characterization of **6**•$C_{60}$ ..... 33

1.2.8 Charge Transfer in **1**•$C_{60}$ ..... 36

1.2.9 Bonding Interactions in Superatomic Solids ..... 37

1.2.10 Physical Properties of Solid State Fulleride Materials ..... 41

1.2.11 Charge Transport in Superatomic Solids ..... 42

1.2.12 Magnetic Properties of Superatomic Solids ..... 44

1.3 Experimental Details ..... 47

1.3.1 General Considerations ..... 47

1.3.2 $Ni_3I_2(dppm)_3$ (**1**) ..... 53

1.3.3 $Ni_3Te_2(dppm)_3$ (**2**) ..... 53

1.3.4 $Ni_3Se_2(dppm)_3$ (**3**) ..... 54

1.3.5 $Ni_3S_2(dppm)_3$ (**4**) ..... 54

1.3.6 $Co_4S_4(PPr^i_3)_4$ (**5**) ..... 55

1.3.7 $Mo_3S_5(PMe_3)_6$ (**6**) ..... 55

1.3.8 **1**•$C_{60}$ ..... 56

1.3.9 **1**•$C_{70}$ ..... 57

1.3.10 **1**•TCNQ ..... 57

1.3.11 **2**•$C_{60}$ ..... 57

1.3.12 **2**•$C_{70}$ ..... 58

1.3.13 **3**•$C_{60}$ ..... 58

1.3.14 **4**•$C_{60}$ ..... 58

1.3.15 **6**•$C_{60}$ ..... 59

1.4 Conclusions ..... 60

1.4.1 Conclusions ..... 60

1.4.2 Future Work ..... 61

CHAPTER 2: METAL CHALCOGENIDE CLUSTERS FOR CLUSTER ORGANIC FRAMEWORKS ..... 63

2.1 Introduction ..... 63

2.1.1 Metal Organic Frameworks ..... 63

2.1.2 Covalent Organic Frameworks ..... 65

2.1.3 Atomic Two-Dimensional Materials ..... 70

2.1.4 Coordination Nanosheets (CONASHs) ..... 71

2.1.5 Research Goals ..... 73

2.2 Results and Discussion ..... 77

2.2.1 Synthesis and Characterization of $Mo_3(\mu_3\text{-}S)_2(\mu_2\text{-}S)_3(\kappa^2\text{-}dppbzOMe)_3$ (**8**) 77

2.2.2 Synthesis and Characterization of **11** ..... 81

2.3 Experimental Details ..... 85

2.3.1 General Considerations ..... 85

2.3.2 1,2-bis(diphenylphosphino)-4,5-dimethoxybenzene (**7**) ..... 86

2.3.3 $Mo_3S_5(dppBzOMe)_3$ (**8**) ..... 87

2.3.4 (4-(1,3-Dioxolan-2-yl)phenyldiisopropylphosphine (**9**) ..... 87

2.3.5 4-(diisopropylphosphino)benzaldehyde (**10**) ..... 88

2.3.6 $Co_4S_4(P(Pr^i)_2(C_6H_4CHO))_4$ (**11**) ..... 89

2.4 Conclusions ..... 90

2.4.1 Conclusions ..... 90

2.4.2 Future Work ..... 90

REFERENCES ..... 93

APPENDIX A: CYRSTAL DATA FOR **1**•$C_{60}$ ..... 102

APPENDIX B: CYRSTAL DATA FOR **2**•$C_{60}$ ..... 103

APPENDIX C: CYRSTAL DATA FOR **1**•$C_{70}$ ..... 104

APPENDIX D: CYRSTAL DATA FOR **2**•$C_{70}$ ..... 105

APPENDIX E: CYRSTAL DATA FOR **3**•$C_{60}$ ..... 106

APPENDIX F: CYRSTAL DATA FOR **4**•$C_{60}$ ..... 107

APPENDIX G: CYRSTAL DATA FOR **6**•$C_{60}$ ..... 108

APPENDIX H: CYRSTAL DATA FOR **1**•TCNQ ..... 109

APPENDIX I: CYRSTAL DATA FOR **8** ..... 110

APPENDIX J: I-V CURVE FOR **1** and **1**•$C_{60}$ ..... 111

APPENDIX K: I-V CURVE FOR **2** and **2**•$C_{60}$ ..... 112

APPENDIX L: I-V CURVE FOR **1** and **1**•$C_{70}$ ..... 113

APPENDIX M: I-V CURVE FOR **2** and **2**•$C_{70}$ ..... 114

# LIST OF FIGURES

Figure 1.1. Critical hierarchical design parameters (CHDPs) as they apply to nanoscale materials. (Reprinted with permission from ref 3. Copyright 2014 John Wiley and Sons.) ..... 3

Figure 1.2. TEM images of BNSLs and corresponding atomic lattice structures for superlattices assembled from a) 13.4 nm γ-$Fe_2O_3$ and 5.0 nm Au; b) 7.6 nm PbSe and 5.0 nm Au; c) 6.2 nm PbSe and 3.0 nm Pd; d) 6.7 nm PbS and 3.0 nm Pd; 6.2 nm PbSe and 3.0 nm Pd; f) 5.8 nm PbSe and 3.0 nm Pd; g) 7.2 nm PbSe and 4.2 nm Ag; h) 6.2 nm PbSe and 3.0 nm Pd; 1) 7.2 nm PbSe and 5.0 nm Au; j) 5.8 nm PbSe and 3.0 nm Pd; k) 7.2 nm PbSe and 4.2 nm Ag; and l) 6.2 nm PbSe and 3.0 nm Pd nanoparticles. (Reprinted with permission from ref 5. Copyright 2006 Nature Publishing Group.) ..... 5

Figure 1.3. Crystal structure of intercluster compound $[Au_9(PPh_3)_8][V_{10}O_{28}H_3]_2$ viewed down the *a*-axis. (Reprinted with permission from ref 24. Copyright 2007 American Chemical Society.) ..... 7

Figure 1.4. a) Crystal structure of $[Ag_{14}(C{\equiv}C\textit{t}Bu)_{12}Cl(CH_3CN)]_2[W_6O_{19}]$ (ligands have been removed for clarity, unit cell shown in red) and b) crystal structure of $(\textit{n}Bu_4N)[Ag_{14}(C{\equiv}C\textit{t}Bu)_{12}Cl(CH_3CN)]_2[PW_{12}O_{40}]$ (ligands have been removed for clarity). (Reprinted with permission from ref 23. Copyright 2010 John Wiley and Sons.) ..... 8

Figure 1.5. Crystal structures of a) $[Co_6Te_8(PEt_3)_6][Fe_8O_4pz_{12}Cl_4]$ and b) $[Co_6Te_8(PEt_2Ph)_6][Fe_8O_4pz_{12}Cl_4]$ (iron, dark and light red; oxygen, yellow; cobalt, dark blue; tellurium, teal; phosphorus, orange; nitrogen, light blue; chlorine, green; carbon, black. Hydrogen atoms removed for clarity) as well as c) cyclic voltammogram of $[Co_6Te_8(PPr^n{}_3)_6][Fe_8O_4pz_{12}Cl_4]$. (Adapted with permission from ref 27. Copyright 2014 American Chemical Society.) ..... 9

Figure 1.6. Crystal packing of $[Au_7(PPh_3)_7][C_{60}]{\bullet}THF$ viewed along the *b*-axis. Solvent molecules and phenyl substituents have been removed to clarify the view. (Adapted with permission from ref 29. Copyright 2008 Angewandte Chemie International Edition.) ..... 11

Figure 1.7. Crystal structures of $[Au_8(PPh_3)_8][C_{60}]_2$ viewed down the c-axis at a) 230 K and b) 100 K showing fulleride dimerization at low temperatures (phenyl substituents removed for clarity). (Adapted with permission from ref 29. Copyright 2008 Angewandte Chemie International Edition.) ..... 11

Figure 1.8. Cyclic voltammogram of Fullerene (Reprinted with permission from ref 31. Copyright 1992 American Chemical Society.) ..... 12

Figure 1.9. Crystal structures of TPC ($D_{II}$) and $MDABCO^+$ ($D_I^+$). a) Crystal packing showing host-guest interaction of TPC and $MDABCO^+$. b, c) Orthogonal views of ($MDABCO^+$)•(TPC)•($C_{60}^{\bullet-}$) indicating key-keyhole docking of fulleride anions. Carbon, gold; nitrogen, dark blue; hydrogen, cyan. (Reprinted with permission from ref 37. Copyright 2010 Angewandte Chemie International Edition.) ..... 14

Figure 1.10. Superatom precursors and crystal packing of corresponding superatomic solids. (Reprinted with permission from ref 31. Copyright 2013 The American Association for the Advancement of Science.) ..... 15

Figure 1.11. Relationship between metal cluster capping ligands and potential coordination sites for fullerene. ..... 17

Figure 1.12. a) Ball and stick side view and b) space-filled top view of crystal structure of $Ni_3(\mu_3\text{-}I)_2(\mu_2\text{-}dppm)_3$. (Nickel, red; iodine, purple; phosphorus, orange; carbon, black. Hydrogen substituents removed for clarity). c) Symbolic representation of proposed trinuclear nickel cluster packing with $C_{60}$ fullerene. ..... 18

Figure 1.13. Cone angles of selected phosphine ligands. ..... 19

Figure 1.14. Scanning electron microscopy images of crystalline **1**•$C_{60}$. Crystal lengths range from 100 μm to 900 μm (left). ..... 21

Figure 1.15. Crystal structure of **1**•$C_{60}$ viewed down the a) *b*-axis and b) *c*-axis. Phenyl and methylene substituents and hydrogen atoms have been removed to clarify the view. Nickel, red; iodine, purple; phosphorus, orange; carbon, black. ..... 22

Figure 1.16. Close contacts between iodide capping ligands and hexagonal face of fulleride anions in **1**•$C_{60}$ (hydrogen atoms removed for clarity). Nickel, red; iodine, purple; phosphorus, orange; carbon, black. ..... 23

Figure 1.17. Space-filled crystal structure of **2**•$C_{60}$. Phenyl moieties, methylene carbon atoms, and hydrogen atoms have been removed to clarify the view. Nickel, red; tellurium, teal; phosphorus, orange; carbon, black. ..... 25

Figure 1.18. Partial space-filling structure of **1**•$C_{70}$ (phenyl substituents, methylene carbons, and hydrogen atoms have been removed for clarity). Nickel, red; iodine, purple; phosphorus, orange; carbon; black. ..... 27

Figure 1.19. Space-filling crystal structure of **3**•$C_{60}$ viewed down the *c*-axis (phenyl substituents, methylene carbon atoms, and hydrogen atoms have been removed to clarify the view). Nickel, red; selenium, green; phosphorus, orange; carbon, black. ..... 29

Figure 1.20. Crystal packing of **4**•$C_{60}$. Phenyl substituents, methylene carbon atoms, and hydrogen atoms have been removed for clarity. Nickel, red; sulfur yellow; phosphorus, orange; carbon; black. ..... 31

Figure 1.21. a) Ball and stick (hydrogen atoms removed) b) space filled crystal structure of cluster **5**. Cobalt, blue; sulfur, yellow; phosphorus, orange; carbon, black; hydrogen, white. ..... 33

Figure 1.22. a) Top and b) side views of the crystal structure of cluster **6** (methyl moieties removed for clarity). Molybdenum, cyan; sulfur, yellow; phosphorus, orange. ..... 35

Figure 1.23. Ball and stick representation of crystal packing in **6**•$C_{60}$ viewed down the *b*-axis ($CH_3$ groups have been removed to clarify the view). Molybdenum, cyan; sulfur, yellow; phosphorus, orange; carbon, black. ..... 36

Figure 1.24. Normalized solid state infrared spectra for $Ni_3I_2(dppm)_3$•$C_{60}$ (blue), $Ni_3I_2(dppm)_3$ (black), and $C_{60}$ (red). ..... 37

Figure 1.25. Crystal packing of **1**•TCNQ viewed down the a) *a*-axis and b) *b*-axis (phenyl substituents, methylene carbon atoms, and hydrogen atoms removed for clarity). Nickel, red; iodine, purple; phosphorus, orange; nitrogen, lavender; carbon black. ..... 40

Figure 1.26. TCNQ capping ligand interaction (phenyl substituents removed for clarity). Nickel, red; iodine, purple; phosphorus, orange; nitrogen, lavender; carbon black. ..... 40

Figure 1.27. a) Semiconducting behavior of $[Co_6Se_8(PEt_3)_8][C_{60}]_2$ and b) ferromagnetic behavior of $[Ni_9Te_6(PEt_3)_8][C_{60}]$. (Adapted with permission from ref. 17. Copyright 2013 The American Association for the Advancement of Science.) ..... 42

Figure 1.28. Plot of electric field strength versus current density for clusters **1** and **2** as well as their corresponding $C_{60}$ and $C_{70}$ superatomic solids. ..... 43

Figure 1.29. Curie-Weiss plots for **1**•$C_{60}$ and **2**•$C_{60}$. ..... 45

Figure 1.30. Temperature dependence of the effective magnetic moments of **1**•$C_{60}$ and **2**•$C_{60}$. ..... 46

Figure 1.31. Different ordered possibilities for the fulleride substructure of $Ni_3I_2$-$C_{70}$. Left, staggered in $P2_1/n11$; right, eclipsed in $P112_1/a$. Views along 001 with 010 up. ..... 51

Figure 1.32. $C_{140}$ disordered over mirror plane..... 51

Figure 1.33. A defect in $Ni_3I_2$-$C_{70}$ in which one $C_{70}$ monomer occurs between two $C_{140}$ dimers. ..... 52

Figure 1.34. Structures of a) $Ni_3S_2(dppe)_3$ and b) $Ni_3Se_2(PEt_3)_6$. Nickel, red; sulfur, yellow; selenium, green; phosphorus, orange; carbon, gray. Hydrogen atoms removed to clarify the view. ..... 62

Figure 2.1. Structural variations of MOF-5 topology achieved through utilization of differing organic linkers. (Reprinted with permission from ref 73. Copyright 2015 Royal Society of Chemistry.)..... 64

Figure 2.2. Structural representation of COF-1 generated from powder diffraction data viewed down the *c*-axis (carbon, gray; boron, orange; oxygen, red). (Reprinted with permission from ref 80. Copyright 2005 The American Association for the Advancement of Science.)..... 67

Figure 2.3. a) 3D COF building blocks b) and structural representations of resulting COFs 102, 105, and 108. (Adapted with permission from ref 82. Copyright 2007 The American Association for the Advancement of Science.)..... 68

Figure 2.4. Selected a) porphyrin-based (adapted with permission from ref 85. Copyright 2011 American Chemical Society.) b) luminescent (adapted with permission from , ref 84. Copyright 2008 Angewandte Chemie International Edition.) and c) catalytic COFs. (Adapted with permission from ref 86. Copyright 2011 American Chemical Society.)..... 69

Figure 2.5. Structural representations of selected atomic 2D materials. (Adapted with permission from ref. 88. Copyright 2014 Royal Society of Chemistry.)..... 70

Figure 2.6. Structure of molybdenum disulfide viewed from the a) top and b) side (molybdenum, teal; sulfur, yellow). ..... 71

Figure 2.7. Bottom up concept behind the formation of coordination nanosheets. (Reprinted with permission from ref 94. Copyright 2016 The American Chemical Society.) ..... 72

Figure 2.8. Example of coordination nanosheet structure. (Reprinted with permission from ref 95. Copyright 2013 The American Chemical Society.) ..... 73

Figure 2.9. Structural comparison of a) bicapped molybdenum cluster and b) $MoS_2$ (molybdenum, blue/teal; sulfur, yellow; phosphorus, orange). ..... 74

Figure 2.10. Pictorial representation of proposed $Mo_3S_5$ COF (top view). ..... 75

Figure 2.11. Crystal structure of **8** viewed from the a) top and b) side (phenyl substituents and hydrogen atoms removed to clarify the view). Molybdenum, cyan; sulfur, yellow; oxygen, red; carbon, black. ..... 78

Figure 2.12. $^{31}P$ NMR spectrum of solid material obtained from crystallization of **8.** ..... 79

Figure 2.13. $^{31}P$ NMR spectrum of $(dppBzOMe)S_2$. ..... 79

Figure 2.14. $^{31}P$ NMR spectrum dppBzOMe ligand. ..... 80

Figure 2.15. Cyclic voltammograms of a) **8** in PC and b) **6** in DCM. Measurements were taken at 100 mV/s against $Fc/Fc^+$ with TBA•$PF_6$ supporting electrolyte, glassy carbon working electrode and Pt counter electrode. ..... 81

Figure 2.16. $^{31}P$ NMR spectrum of cluster **5**. ..... 83

Figure 2.17. $^{31}P$ NMR spectrum of b) crude product of cluster **11** reaction. ..... 84

# LIST OF SCHEMES

Scheme 1.1. Synthesis of Cluster **1** from $Ni(COD)_2$ and $NiI_2$ in Solution. ..... 20

Scheme 1.2. Formation of **1**•$C_{60}$ via diffusion of **1** in Toluene and $C_{60}$ in 1-methylnaphthalene. ..... 21

Scheme 1.3. Synthesis of Cluster **2**..... 24

Scheme 1.4. Synthesis of Cluster **3**..... 28

Scheme 1.6. Synthesis of Cluster **5**..... 32

Scheme 1.7. Synthesis of Cluster **6**..... 34

Scheme 1.8. Selected Bond Lengths and Angles in Neutral, Mono-, and Dianionic TCNQ (Reprinted with permission from ref 56. Copyright 1969 Royal Society of Chemistry.) ..... 38

Scheme 2.1. Synthesis of COF-1. (Reprinted with permission from ref 80. Copyright 2005 The American Association for the Advancement of Science.)..... 67

Scheme 2.2. Proposed Synthesis for Cobalt Cubane Cluster-based COF. ..... 76

Scheme 2.3. Synthesis of Cluster **8**..... 77

Scheme 2.4. Proposed Synthesis of Cluster **11**..... 82

# LIST OF EQUATIONS

Equation 1.1. $\chi_{MT} = C(T-\Theta) + \chi_D + \chi_{TIC}$ ..... 44

# LIST OF ABBREVIATIONS

| | |
|---|---|
| BET | Brunauer-Emmet-Teller |
| BNSLs | Binary Nanoparticle Superlattices |
| CHDPs | Critical Hierarchical Design Parameters |
| CNDPs | Critical Nanoscale Design Parameters |
| COD | Cyclooctadiene |
| COF | Covalent organic framework |
| CONASH | Coordination nanosheet |
| dmpm | Bis(dimethylphosphino)methane |
| dppBzOMe | 1,2-bis(diphenylphosphino)dimethoxybenzene |
| dppCAT | 1,2-bis(diphenylphosphino)catechol |
| dppe | Bis(diphenylphosphino)ethane |
| dppm | Bis(diphenylphosphino)methane |
| EPR | Electron paramagnetic resonance |
| f.c.c. | Face-centered-cubic |
| h-BN | Hexagonal boron nitride |
| HDS | Hydrodesulfurization |
| HHTP | Hexahydroxytriphenylene |
| HOMO | Highest occupied molecular orbital |
| IR | Infrared |
| I-V | Current-voltage |
| $MDABCO^+$ | N-methyldiazabicyclooctane |
| MO | Molecular orbital |

| | |
|---|---|
| MOF | Metal-organic framework |
| NMR | Nuclear magnetic resonance |
| PTSA | *p*-toluene sulfonic acid |
| SBU | Secondary building unit |
| SCE | Saturated Calomel Electrode |
| SQUID | Superconducting quantum interference device |
| TBPM | *Tetra*(4-dihydoxyborylphenyl)methane |
| TBPS | *Tetra*(4-dihydoxyborylphenyl)silane |
| TCNQ | 7,7,8,8-tetracyanoquinodimethane |
| TDAE | Tetrakis(dimethylamino)ethane |
| THF | Tetrahydrofuran |
| TMDCs | Transition metal dichalcogenides |
| TPC | Triptycene |
| VOC | Volatile organic compound |
| XRD | X-ray Diffraction |
| 2D | Two-dimensional |
| 3D | Three-dimensional |

# CHAPTER 1: TRINUCLEAR METAL CHALCOGENIDE CLUSTERS FOR SUPERATOMIC SOLIDS

## 1.1 Introduction

### 1.1.1 Hierarchical Design

Historically, work in the physical sciences has been made possible due to the unique characteristics and properties of atoms. Classification of atoms based upon these elemental properties has enabled predictive, product directed synthesis and more thorough understanding of chemical relationships. This broad identification and organization of periodic patterns led to the emergence of chemistry and physics as areas of study. Furthermore, these critical manipulations enabled the development of unifying principles that were proven to hold across the different physical science disciplines. This *central dogma* has been used to rationalize the arrangement of subatomic particles to yield atoms and the interaction of atoms to form subnanoscale materials such as simple molecules.[1]

The complexity of the rapidly developing field of nanoscience has led to the emergance of larger, more complex materials with unique, size dependent properties of their own.[2] Controlled synthesis of these materials is often a challenge as their assembly relies upon spontaneous nucleation events and unpredictable surface interactions. Often, uncontrollable solution phase phenomena (i.e. Otswald ripening) broaden the dispersity of nanoscale morphologies obtained and decrease the synthetic reproducibility. The wide

range of achievable materials and resulting properties has made establishment of overarching principles for nanoscience difficult and hindered the growth of the emerging field. In a recent review, Tomalia and Khanna have highlighted some of the efforts currently being made to derive a "Mendeleev-like taxonomy" applicable to nanoscale materials.

These efforts are centered upon a "bottom up" synthetic approach. Such an approach enables application of existing atomic trends to more complex systems. This school of thought allows complex molecules and small nanoclusters to be considered as building blocks that can be assembled in ways directed by nanoperiodic rules known as critical nanoscale design parameters (CNDPs); namely: size, shape, surface chemistry, flexibility, architecture, and elemental composition (Figure 1.1).[1,3] Utilization of well-defined molecular building blocks has led to greater synthetic control in the assembly of hierarchical solids.

Cademartiri *et al.* identify five major milestones scientists will need to overcome in achieving hierarchical/self assembled materials of life-like structure and function: i) synthesize the necessary building blocks; ii) exercise control over the binary interaction of these building blocks; iii) predict the interaction of a variety of building blocks in a designated environment; iv) determine which blocks will form a specified product; and v) generate functional self-assembled materials.[4] The maturity of chemistry as a science and established periodic trends has made mastery of small building block synthesis achievable, though strategies for structural perfection on the nanoscale are slightly less developed. Current research attempts are focused on the second milestone – understanding and controlling the binary interactions of building blocks. Self-assembled

materials can be reliably formed from simple building blocks. However, steps toward predictable assembly have been limited by lack of understanding of the interactions (surface chemistry, van der Waals and noncovalent forces) between constituent building blocks.

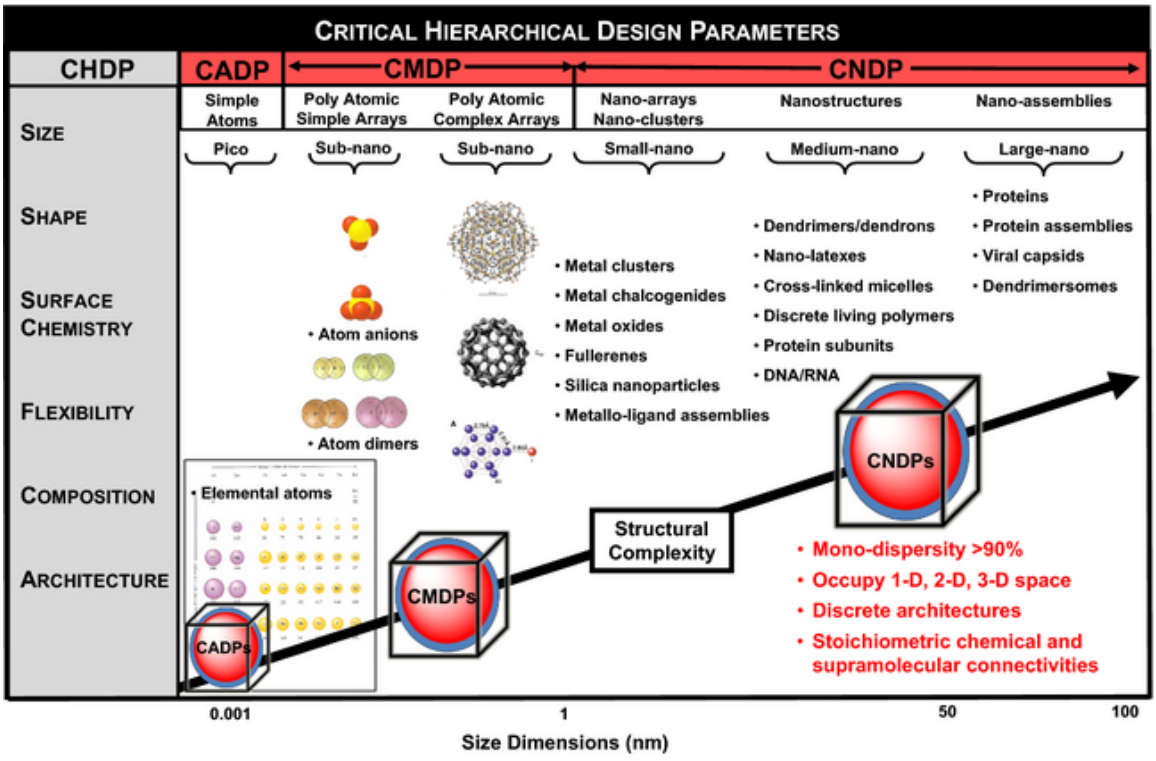


Figure 1.1. Critical hierarchical design parameters (CHDPs) as they apply to nanoscale materials. (Reprinted with permission from ref 3. Copyright 2014 John Wiley and Sons.)

This "bottom up" approach has proven to be particularly successful for synthesis of binary nanoparticle superlattices (BNSLs).[5] It is known that, in liquid, monodisperse spheres prefer face-centered-cubic (f.c.c) packing.[6,7] This orientation enhances the total entropy of the system as it provides larger local free space for each sphere and drives the

ordering phase transition.[5] Overall packing depends upon the morphologies of the hard spheres. Application of this principle to systems containing mixtures of two different nanoparticles yields BNSLs. The formation of these superlattices on substrates results in materials that are isostructural to known atomic compounds (Figure 1.2).[5] However, use of identical nanoparticle mixtures results in the formation of a multitude of BNSL architectures. Murray and coworkers report the synthesis of eleven different BNSLs using the same batches of PbSe and Pd nanoparticles. The variety of achievable structures and deviation from f.c.c. packing suggests that entropy is not the structure directing force in these hierarchical solids.[5] Coulombic attractions between constituent nanoparticles have been shown impart selectivity for specific arrangements.[8] As the charges of the nanocrystals can be controlled through surfactant modification, interactions between the building blocks become increasingly important in the hierarchical assembly of these nanoscale materials.

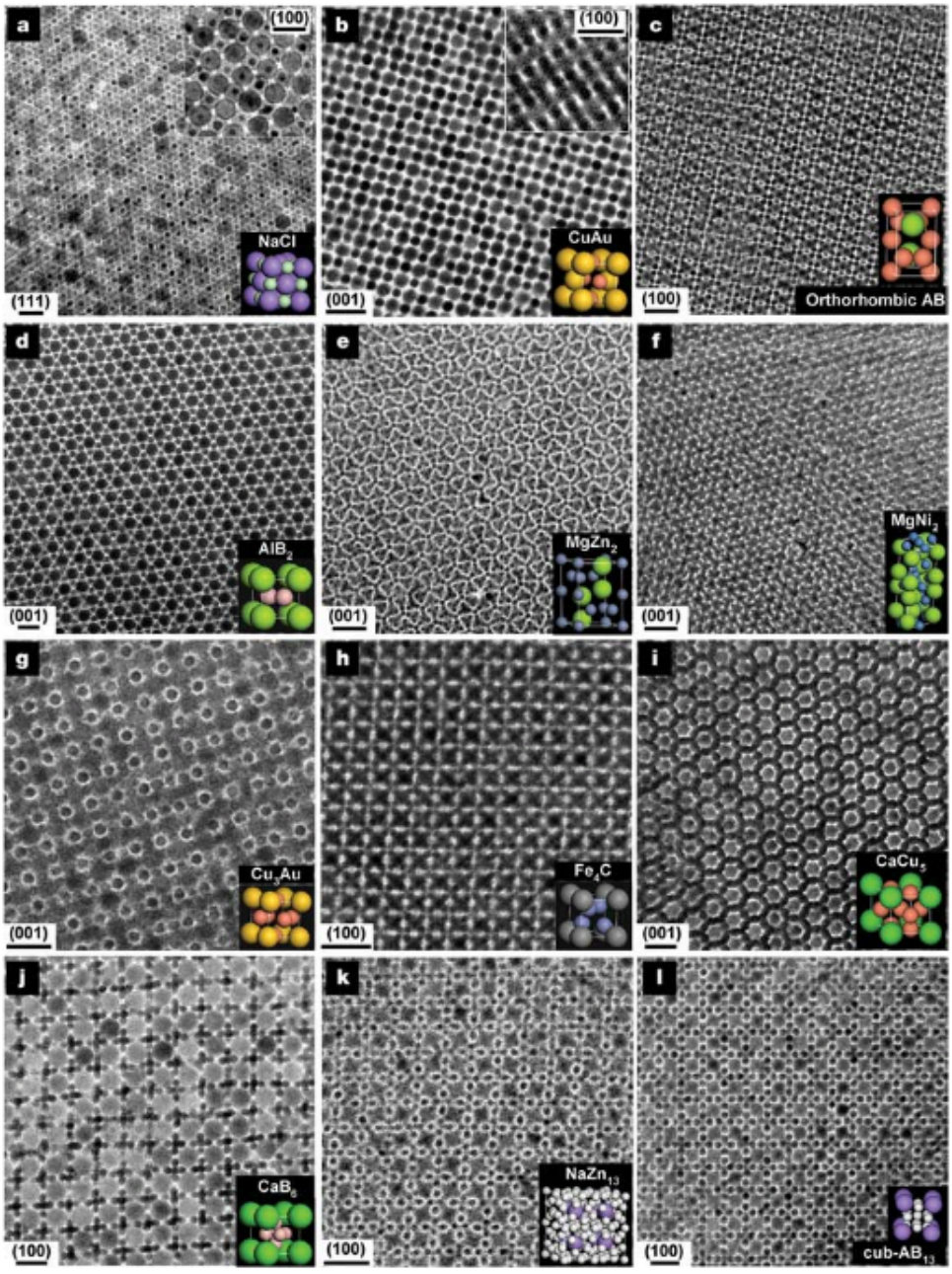


Figure 1.2. TEM images of BNSLs and corresponding atomic lattice structures for superlattices assembled from a) 13.4 nm γ-$Fe_2O_3$ and 5.0 nm Au; b) 7.6 nm PbSe and 5.0 nm Au; c) 6.2 nm PbSe and 3.0 nm Pd; d) 6.7 nm PbS and 3.0 nm Pd; 6.2 nm PbSe and 3.0 nm Pd; f) 5.8 nm PbSe and 3.0 nm Pd; g) 7.2 nm PbSe and 4.2 nm Ag; h) 6.2 nm PbSe and 3.0 nm Pd; 1) 7.2 nm PbSe and 5.0 nm Au; j) 5.8 nm PbSe and 3.0 nm Pd; k) 7.2 nm PbSe and 4.2 nm Ag; and l) 6.2 nm PbSe and 3.0 nm Pd nanoparticles. (Reprinted with permission from ref 5. Copyright 2006 Nature Publishing Group.)

### 1.1.2 Metal Clusters as Building Blocks

Metal clusters are attractive for investigation of these inter-building block interactions due to their easily controlled synthesis and atomically precise architectures.[9,10] This class of materials pairs the well-defined structures of molecular precursors with the size of nanoparticles.[11,12] Many of these clusters are regarded as atom-like due to their delocalized electronic structures and ability to undergo reversible multielectron transfer while maintaining structural integrity.[13] Therefore, these highly tunable clusters have been designated as *superatoms*.[1,14,15,16] Recently, several materials have been prepared through careful selection and hierarchical assembly of monodisperse superatoms.[17,18–20]

Jansen and coworkers have extensively studied the structure directing interactions in a range of metal cluster-based intercluster compounds.[21–25] One example of these solids is comprised of cationic gold clusters and polyanionic polyoxometallates. The Coulombic interactions provided through the use of charged species lends stability to these systems, leading to high crystal quality.[24] In crystals of $[Au_9(PPh_3)_8][V_{10}O_{28}H_3]_2$ dimers of the decavanadates are formed through hydrogen bonding and confirmed through crystallographic structure analysis.[26] These dimers are arranged in a distorted hexagonal close packing structure and bond distances confirm direct interactions with the cationic gold clusters (Figure 1.3).[24] Each gold cluster exhibits close-contacts to eight surrounding gold clusters via C-H/π interactions of the cluster phenyl rings. The overall $Cs_2S$ packing structure observed is stabilized by these hydrogen-bonding and π interactions.[24]

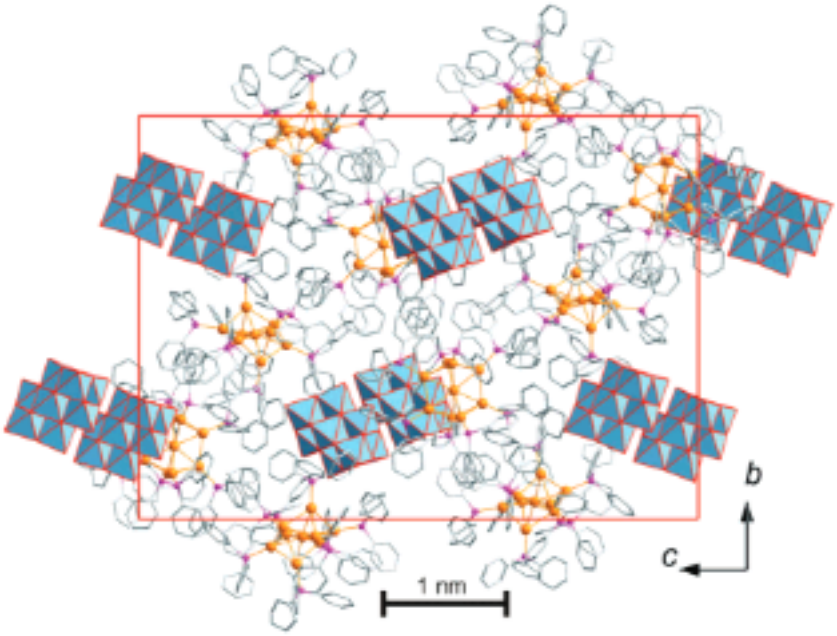


Figure 1.3. Crystal structure of intercluster compound $[Au_9(PPh_3)_8][V_{10}O_{28}H_3]_2$ viewed down the *a*-axis. (Reprinted with permission from ref 24. Copyright 2007 American Chemical Society.)

Comparable stabilizing forces have been observed in intercluster compounds of large cationic silver clusters and polyoxometallates. Rather than abide by commonly observed ion pairing, the equally charged clusters were found to form aggregates.[23] This indicates that that the Coulombic contribution to the lattice energy does not act as a structure-directing force.[23] Short-range attractive forces such as hydrogen-bonding or dispersion interactions dominate in compounds $[Ag_{14}(C\equiv CtBu)_{12}Cl(CH_3CN)]_2[W_6O_{19}]$ and $(nBu_4N)[Ag_{14}(C\equiv CtBu)_{12}Cl(CH_3CN)]_2[PW_{12}O_{40}]$. The former assembles into a CsCl-type layered packing structure while the latter forms double rows that are between hexagonal and tetragonal rod packing arrangements (Figure 1.4).[23]

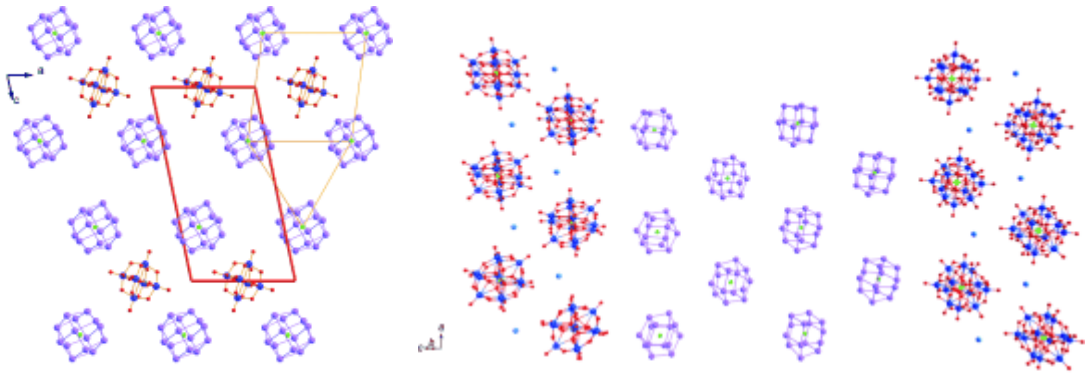

Figure 1.4. a) Crystal structure of $[Ag_{14}(C\equiv C\mathit{t}Bu)_{12}Cl(CH_3CN)]_2[W_6O_{19}]$ (ligands have been removed for clarity, unit cell shown in red) and b) crystal structure of $(\mathit{n}Bu_4N)[Ag_{14}(C\equiv C\mathit{t}Bu)_{12}Cl(CH_3CN)]_2[PW_{12}O_{40}]$ (ligands have been removed for clarity). (Reprinted with permission from ref 23. Copyright 2010 John Wiley and Sons.)

Binary solids have also been prepared through *in situ* charge transfer between metal cluster building blocks.[17,18,27] Roy and coworkers have assembled hierarchical solids from cobalt chalcogenide ($Co_6E_8$, E = Se or Te) and iron oxide molecular cluster building blocks.[27] These clusters were selected due to their complementary oxidation and reduction potentials with the intent that charge transfer from one cluster to the next would be the driving force for crystallization. The structures of the crystalline material obtained indicate that slight variation of the structure and electronic properties of the cobalt chalcogenide precursors result in minor changes in crystalline arrangement. Compounds $[Co_6Se_8(PEt_3)_6][Fe_8O_4pz_{12}Cl_4]$, $[Co_6Te_8(PEt_2Ph)_6][Fe_8O_4pz_{12}Cl_4]$, and $[Co_6Te_8(PEt_3)_6][Fe_8O_4pz_{12}Br_4]$ exhibit CsCl-type packing (Figure 1.5).[27] Electronic absorption spectroscopy confirms the transfer of one electron from the cobalt clusters to the iron clusters during solid formation. Additionally, cyclic voltammetry (CV) measurements of $[Co_6Te_8(PPr^n_3)_6][Fe_8O_4pz_{12}Cl_4]$ in dicholormethane show that the

compound exhibits eight reversible redox events signifying the reversible transfer of electrons into and out of the cluster building blocks (Figure 1.5).[27]

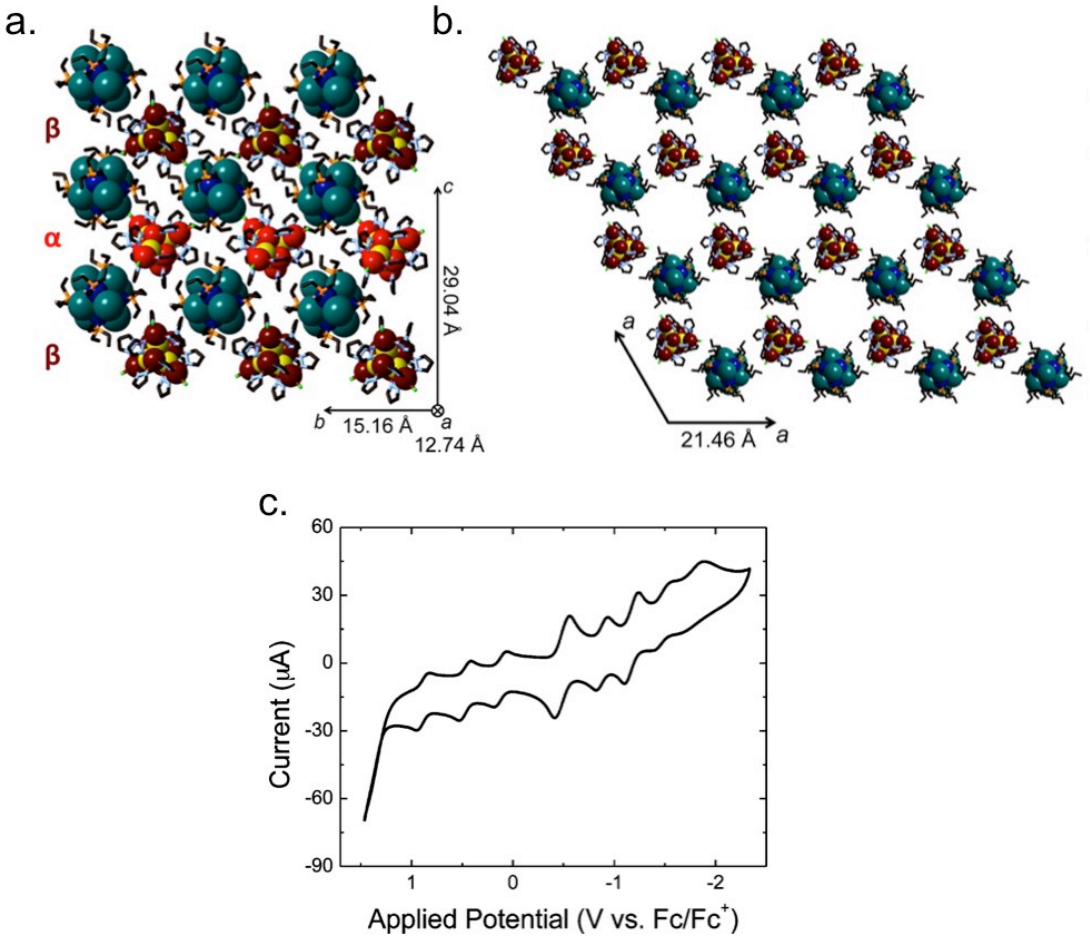


Figure 1.5. Crystal structures of a) $[Co_6Te_8(PEt_3)_6][Fe_8O_4pz_{12}Cl_4]$ and b) $[Co_6Te_8(PEt_2Ph)_6][Fe_8O_4pz_{12}Cl_4]$ (iron, dark and light red; oxygen, yellow; cobalt, dark blue; tellurium, teal; phosphorus, orange; nitrogen, light blue; chlorine, green; carbon, black. Hydrogen atoms removed for clarity) as well as c) cyclic voltammogram of $[Co_6Te_8(PPr^n_3)_6][Fe_8O_4pz_{12}Cl_4]$. (Adapted with permission from ref 27. Copyright 2014 American Chemical Society.)

Jansen and coworkers have expanded their structural investigations of intercluster compounds to include materials containing $C_{60}$ fullerides. Metathesis reactions between solutions containing charged precursors yields black crystalline solids.[26,29] Incorporation of cationic gold clusters with minor structural differences leads to discrepancies in crystal packing. Crystals of $[Au_7(PPh_3)_7][C_{60}]$•THF contain double layers of gold clusters separated by zig-zag chains of fulleride monoanions (Figure 1.6).[29] The unfavorable localization of these charged species suggests that the structure is stabilized by short-range attractive forces between precursors (C-H-π and π-π interactions). Solids containing the dicationic cluster $[Au_8(PPh_3)_8]^{2+}$ and two fulleride anions give a more disordered structure containing hexagonal layers of gold clusters with fulleride monoanions filling the all trigonal-prismatic voids ($AlB_2$-type packing).[29] Again, short-range attractive interactions between the gold clusters and fullerides stabilize the layered structure. Furthermore, dimerization of the fulleride anions in $[Au_8(PPh_3)_8][C_{60}]_2$ is observed at low temperatures due to the close contacts between the molecular clusters (Figure 1.7).[26,29] These structural studies have provided valuable insight into the structure directing forces in self-assembly of fulleride-based solids.

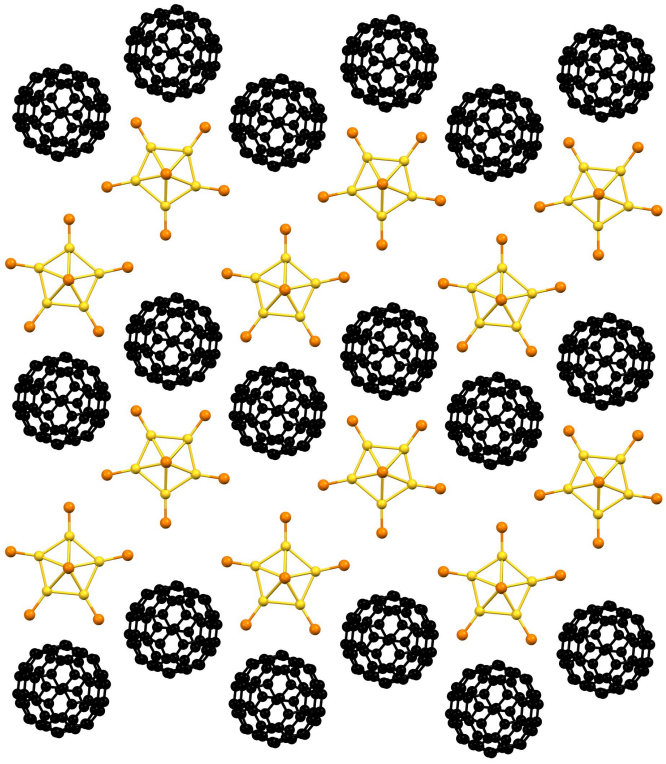

Figure 1.6. Crystal packing of $[Au_7(PPh_3)_7][C_{60}]$•THF viewed along the *b*-axis. Solvent molecules and phenyl substituents have been removed to clarify the view. (Adapted with permission from ref 29. Copyright 2008 Angewandte Chemie International Edition.)

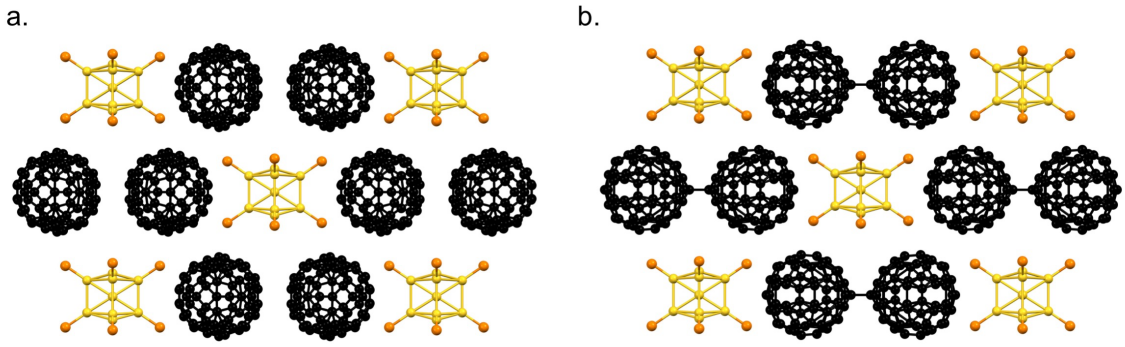


Figure 1.7. Crystal structures of $[Au_8(PPh_3)_8][C_{60}]_2$ viewed down the c-axis at a) 230 K and b) 100 K showing fulleride dimerization at low temperatures (phenyl substituents removed for clarity). (Adapted with permission from ref 29. Copyright 2008 Angewandte Chemie International Edition.)

### 1.1.3 Fulleride-based Self-Assembled Materials

The incorporation of fullerene into hierarchical materials has gained attention in recent years.[30–32] These round, cage-like molecules are attractive for use in hierarchical assemblies due to their electron-accepting ability and high electron affinity (2.69 eV).[32] Specifically, $C_{60}$ is able to undergo six reversible reductions to yield discrete anions known as fullerides (Figure 1.8).[32,33] Fullerides have been used to produce solid-state materials that exhibit noteworthy properties. For example, superconducting phases can be achieved when $C_{60}$ anions are doped with alkali metal cations ($A_3C_{60}$).[34,35] Ferromagnetic phases can be obtained when the spherical anions are integrated into solids with the strong organic electron donor tetrakis(dimethylamino)ethane) ([TDAE][$C_{60}$]).[36–38] There have been numerous techniques employed to incorporate fullerenes into self-assembled materials in an attempt to utilize these physical properties.

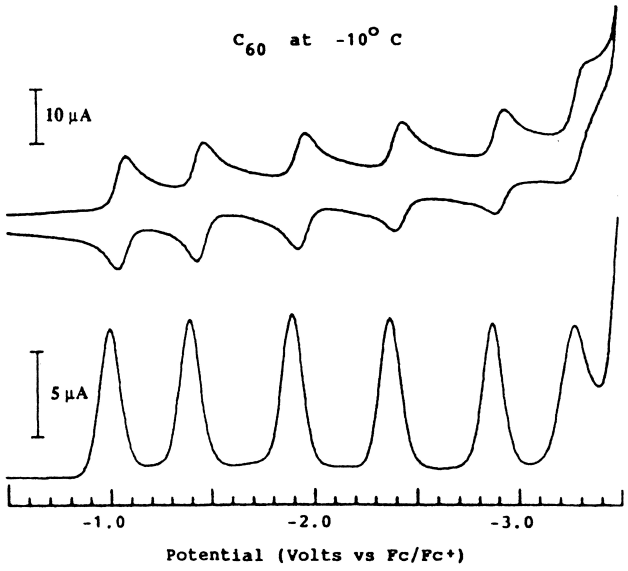


Figure 1.8. Cyclic voltammogram of Fullerene (Reprinted with permission from ref 31. Copyright 1992 American Chemical Society.)

Lyubovskaya and coworkers have engineered one such material through ligand directed assembly.[39] Specifically, their multicomponent approach utilizes two different ligands to synthesize the first fulleride organic metal of the form $D_I^+ \bullet D_{II} \bullet C_{60}^{\bullet -}$. The first of these ligands, $D_I^+$, is small, strong organic donor N-methyldiazabicyclooctane ($MDABCO^+$) which reduces neutral $C_{60}$ to the radical anion ($C_{60}^{\bullet -}$).[39] Triptycene (TPC) acts as $D_{II}$, the second component of this material. The large, neutral ligand directs the crystal packing of the organic complex, enabling the fulleride anions to adopt a close-packed structure without approaching so closely that dimerization to form diamagnetic $(C_{60}^-)_2$ occurs. Furthermore, the shape of TPC allows formation of hexagonal layers with voids for cationic guest molecule $D_I^+$. This key-keyhole relationship leads to formation of shape complementary sites for fulleride anion docking, resulting in hexagonally packed fulleride layers (Figure 1.9).[39] The layered salt $(MDABCO^+)\bullet(TPC)\bullet(C_{60}^{\bullet -})$ is highly conductive with metallic behavior. However, this behavior is interrupted by temperature dependent structural transitions (rhombohedral to triclinic) within the material.[39]

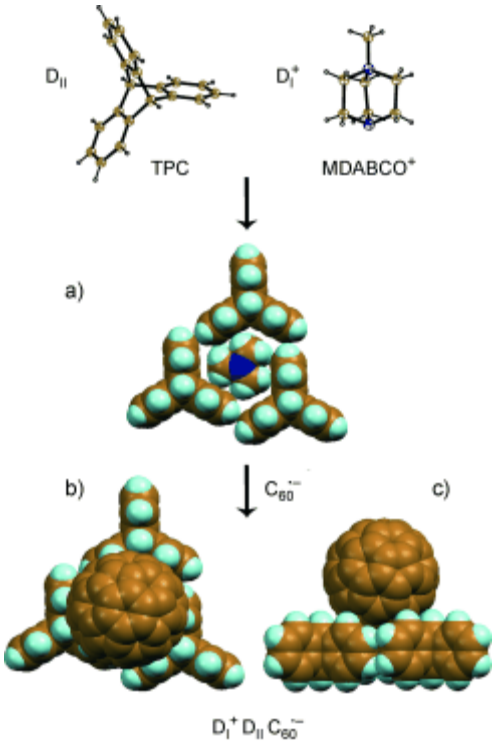


Figure 1.9. Crystal structures of TPC ($D_{II}$) and $MDABCO^+$ ($D_I^+$). a) Crystal packing showing host-guest interaction of TPC and $MDABCO^+$. b, c) Orthogonal views of $(MDABCO^+)$•(TPC)•($C_{60}^{\bullet-}$) indicating key-keyhole docking of fulleride anions. Carbon, gold; nitrogen, dark blue; hydrogen, cyan. (Reprinted with permission from ref 37. Copyright 2010 Angewandte Chemie International Edition.)

Nuckolls, Roy, and coworkers have recently reported the synthesis and characterization of binary ionic solids, termed superatomic solids or superatomic crystals, from fullerene and metal chalcogenide cluster precursors.[17,18] These materials are formed in solution when the metal clusters reduce the neutral fullerene precursors via spontaneous electron transfer. The structure and properties of these superatomic solids differ depending on the cluster precursor selected. For example, $[Ni_9Te_6(PEt_3)_8][C_{60}]$ is a 1:1 rock–salt lattice that undergoes a ferromagnetic phase transition at low temperature (4 K) (Figure 1.10).[18] Conversely, $[Cr_6Se_8(PEt_3)_8][C_{60}]_2$ and $[Co_6Se_8(PEt_3)_8][C_{60}]_2$ both form $CdI_2$-type close packed hexagonal lattices (Figure 1.10).[17] Interactions between

adjacent fullerides in these superatomic solids enable semiconducting behavior. Furthermore, crystals of $[Co_6Se_8(PEt_3)_8][C_{60}]_2$ exhibit thermal conductivity that increases with decreasing temperature, as the superatomic crystal transitions to an orientationally ordered structure.[20]

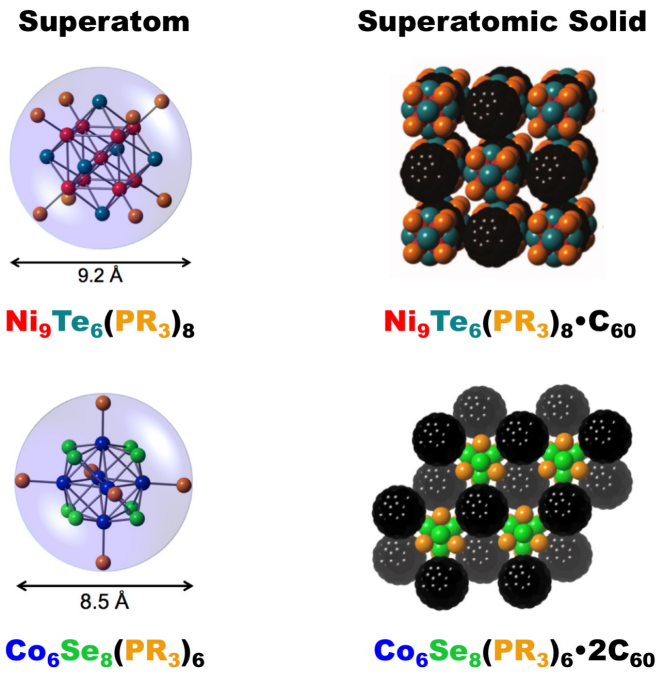


Figure 1.10. Superatom precursors and crystal packing of corresponding superatomic solids. (Reprinted with permission from ref 31. Copyright 2013 The American Association for the Advancement of Science.)

### 1.1.4 Research Objectives

It is clear from Nuckoll's work that the arrangement of fullerene around the individual metal chalcogenide clusters significantly impacts the physical properties of these superatomic solids. This suggests that control over these properties can be accomplished through judicious cluster selection. However, strategic precursor selection

for designer materials requires a deeper understanding of the forces that direct the assembly of these superatom precursors in solution. Therefore, one of the primary objectives of this work is to investigate the relationship between the metal cluster precursor and the resulting arrangement of the fulleride anions within the superatomic lattice. In depth understanding of this relationship should allow for elucidation of the supramolecular structure directing forces within these materials.

As shown above, Nuckolls and coworkers have successfully synthesized superatomic solids with a range of metal chalcogenide cluster precursors.[16–18] The passivating phosphine ligands that stabilize these clusters surround the mixed-valent metal and bridging capping ligand cores.[9] The polarizable capping ligands are left exposed as the phosphine ligands form dative covalent bonds to the individual metal atoms. Comparison of the packing within the cobalt, chromium, and nickel cluster based superatomic solids reveals that, upon charge transfer to fullerene, the chalcogen capping ligands seem to act as "coordination sites" for fulleride anions.[17–20] The repeated occurrence of this coordination of fullerides suggests that (1) the phosphine ligands produce shape complementary cavities that enable fullerene to pack more closely to the cationic cluster core and (2) supramolecular interactions between the exposed capping ligands and fulleride anions direct ionic solid formation (Figure 1.11). Therefore, modification of the metal chalcogenide cluster architecture, through exchanging the phosphine or the capping ligands, may allow predictive structural control leading to a class of designer hierarchical solids.

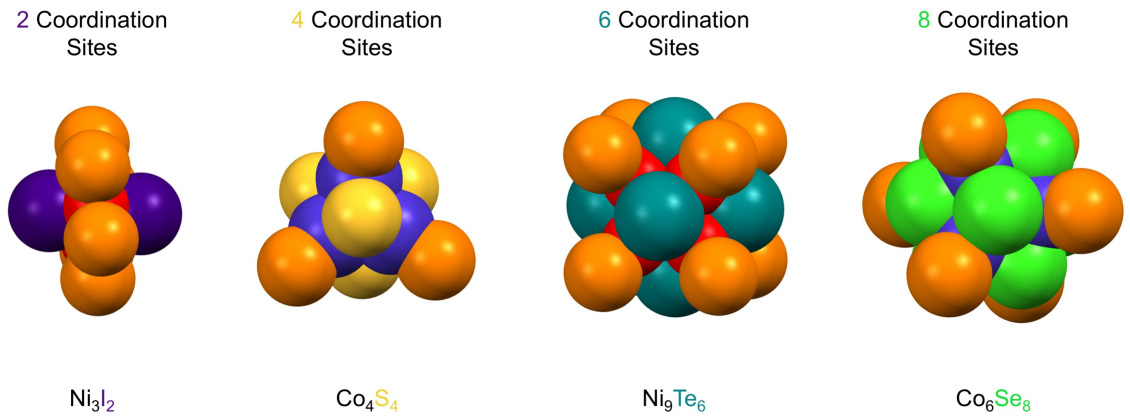


Figure 1.11. Relationship between metal cluster capping ligands and potential coordination sites for fullerene.

Work in this thesis is centered around using trinuclear nickel clusters of the type $Ni_3(\mu_3\text{-}X)_2(\mu_2\text{-}dppm)_3$ (X = I) and $Ni_3(\mu_3\text{-}Q)_2(\mu_2\text{-}dppm)_3$ (Q = S, Se, or Te) as building block precursors to prepare superatomic solids with $C_{60}$ and $C_{70}$ fullerenes. Kubiak and coworkers have extensively studied the structure and electronic properties of trinuclear nickel clusters since their initial synthesis in the 1990's.[40,41] Moreover, the simplicity of these clusters, which contain only two capping ligands, make them excellent candidates to investigate the relationship between the number of fulleride "coordination sites" and superatomic-lattice structure (Figure 1.12). The $\mu_3$- capping ligands are situated 180° apart, above and below the triangular trimer of nickel atoms. Additionally, the use of bulky, bridging diphosphine ligands leaves these capping ligands sterically unhindered while simultaneously providing a cavity of similar size to $C_{60}$ fullerene. These structural considerations suggest that use of these trinuclear nickel clusters as superatomic precursors with fullerenes may lead to ionic solids that pack in a ball and socket arrangement. Therefore, each cluster would coordinate two fulleride anions in a linear

arrangement as opposed to the coordination of six fulleride anions by $Ni_9Te_6(PEt_3)_8$.[18] The synthesis of superatomic solids using trinuclear nickel precursors could give rise to functional materials with differing structural morphologies and, therefore, exotic physical properties.

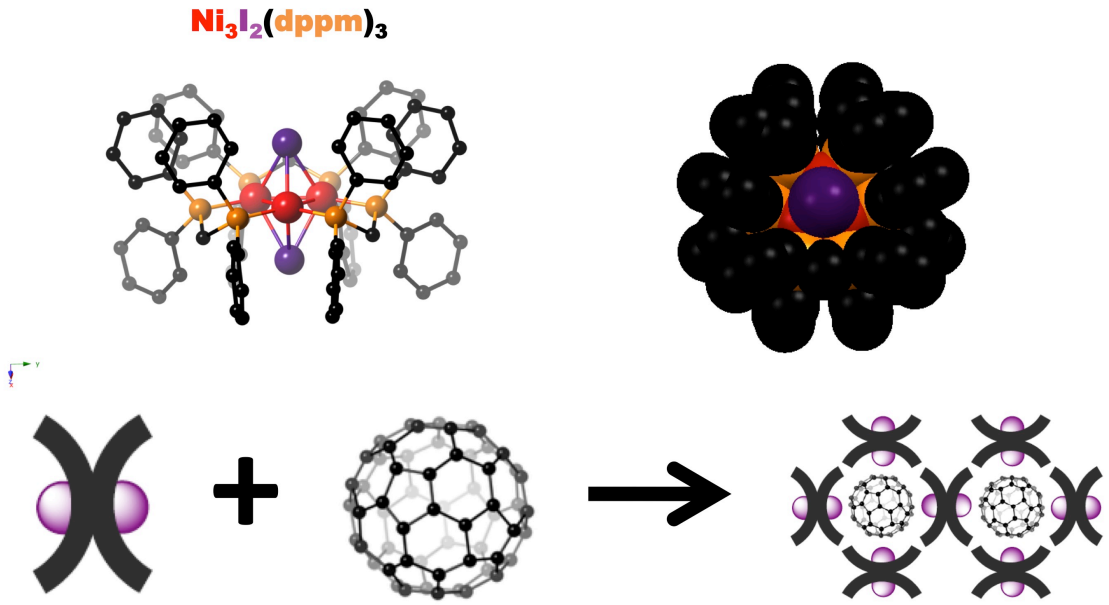


Figure 1.12. a) Ball and stick side view and b) space-filled top view of crystal structure of $Ni_3(\mu_3\text{-}I)_2(\mu_2\text{-}dppm)_3$. (Nickel, red; iodine, purple; phosphorus, orange; carbon, black. Hydrogen substituents removed for clarity). c) Symbolic representation of proposed trinuclear nickel cluster packing with $C_{60}$ fullerene.

The study was also expanded to include clusters of various shapes and number of capping ligands to further investigate the relationship between the number of fulleride "coordination sites" and the resulting superatomic-lattice. Clusters $Co_4(\mu_3\text{-}S_4)(PPr^i_3)_4$ and $Mo_3(\mu_3\text{-}S)_2(\mu_2\text{-}S)_3(PMe_3)_6$ (Me = $CH_3$) were also studied as superatom building blocks containing four and five "coordination sites", respectively.[42,43] These clusters also offer

differing binding environments for fullerene based on their phosphine ligands. The cobalt cubane cluster incorporates bulky, monodentate triisopropylphosphine ($PPr^{i}_{3}$) ligands as opposed to the bridging diphosphine ligands found in the trinuclear nickel clusters. Conversely, the trinuclear molybdenum cluster contains trimethylphosphine ($PMe_3$) ligands, which offer considerably less steric hindrance (Figure 1.13).[44,45] Understanding the structure directing forces within solids comprised of these building blocks and fullerenes could enable predictable assembly of binary superatomic solids. This synthetic predictability could allow derivation of unifying principles, increasing the progress toward further extending classification methods for nanoscale materials, such as a nanoscale periodic table.[1]

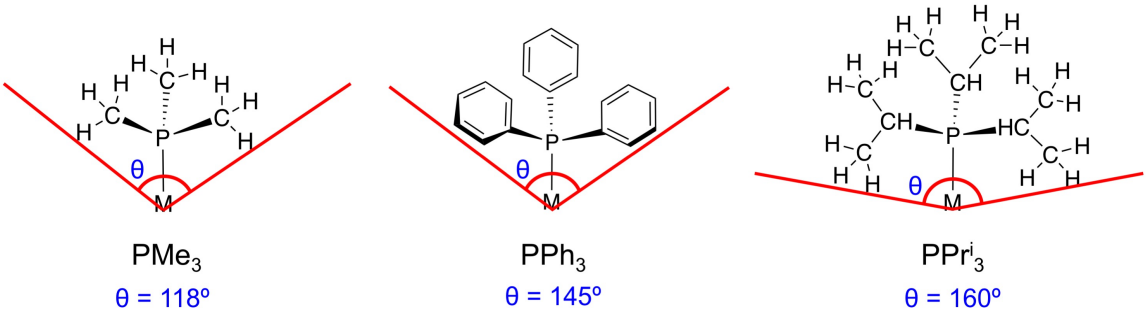


Figure 1.13. Cone angles of selected phosphine ligands.

## 1.2 Results and Discussion

### 1.2.1 Synthesis and Structural Characterization of **1**•$C_{60}$

Cluster **1** was synthesized according literature procedure in which bis-cyclooctadiene nickel(0) ($Ni(COD)_2$) was treated with bis-diphenylphosphinomethane (dppm) in toluene to form intermediate $Ni_2(dppm)_3$.[40] The resulting dark red intermediate was transferred to a solution of nickel(II) iodide ($NiI_2$) in methanol (MeOH), leading to the immediate formation of **1** via a comproportionation reaction between the nickel containing reagents (Scheme 1.1).

Scheme 1.1. Synthesis of Cluster **1** from $Ni(COD)_2$ and $NiI_2$ in Solution.

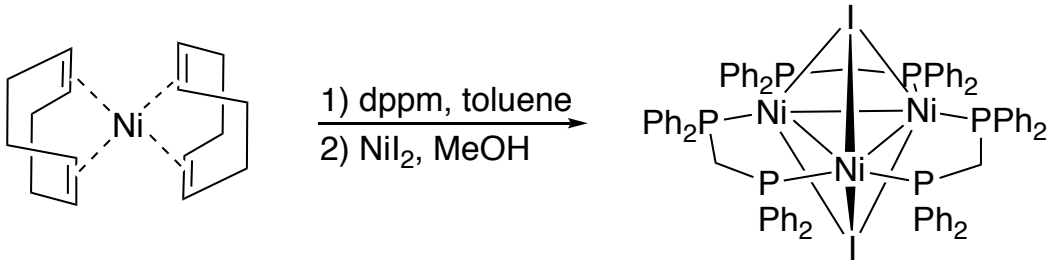


Crystals of **1**•$C_{60}$, obtained through diffusion of solutions of the two precursors, were found to be suitable for single crystal X-ray diffraction (XRD) experiments (Figure 1.14, Scheme 1.2). The nickel trimer core in the binary solid is an isosceles triangle ($d_{Ni\text{-}Ni}$ = 2.505 Å, 2.505 Å, 2.463 Å). This is in agreement with previously reported structural data for $\mathbf{1}^+$ and contrasts from the nearly equilateral core found in neutral cluster **1**.[40] Moreover, this change in the nickel metal core shape indicates that a one-electron charge transfer accompanies the formation of **1**•$C_{60}$. The superatomic solid crystallizes in the

orthorhombic space group *Pnma* and is comprised of zig-zag chains of alternating **1** and $C_{60}$ along the *b*-axis (Figure 1.15). Similar chains of $C_{60}$ zig-zag down the *c*-axis of the crystal (Figure 1.15). The fulleride anions in these chains are closely packed with atom-to-atom distances of 3.57 Å and centroid-to-centroid distances of 10.390 Å. Solvent molecules, one toluene and one 1-methylnaphthalene per formula unit, are also incorporated in the lattice.

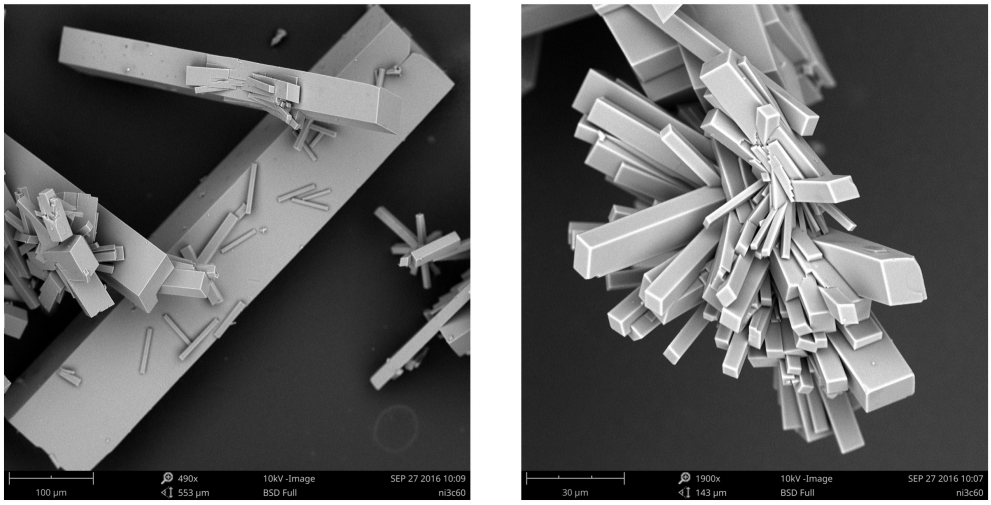


Figure 1.14. Scanning electron microscopy images of crystalline **1**•$C_{60}$. Crystal lengths range from 100 µm to 900 µm (left).

Scheme 1.2. Formation of **1**•$C_{60}$ via diffusion of **1** in Toluene and $C_{60}$ in 1-methylnaphthalene.

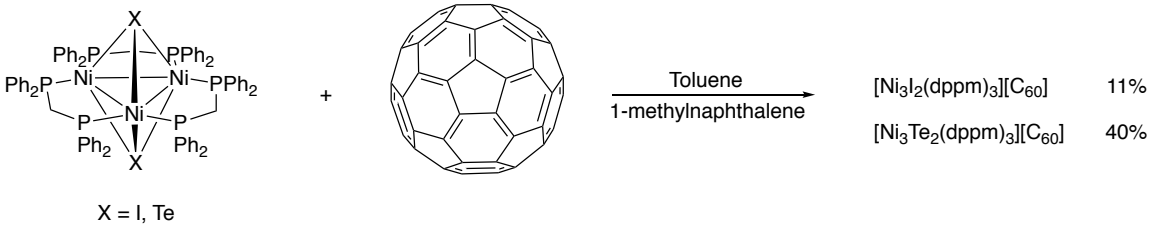

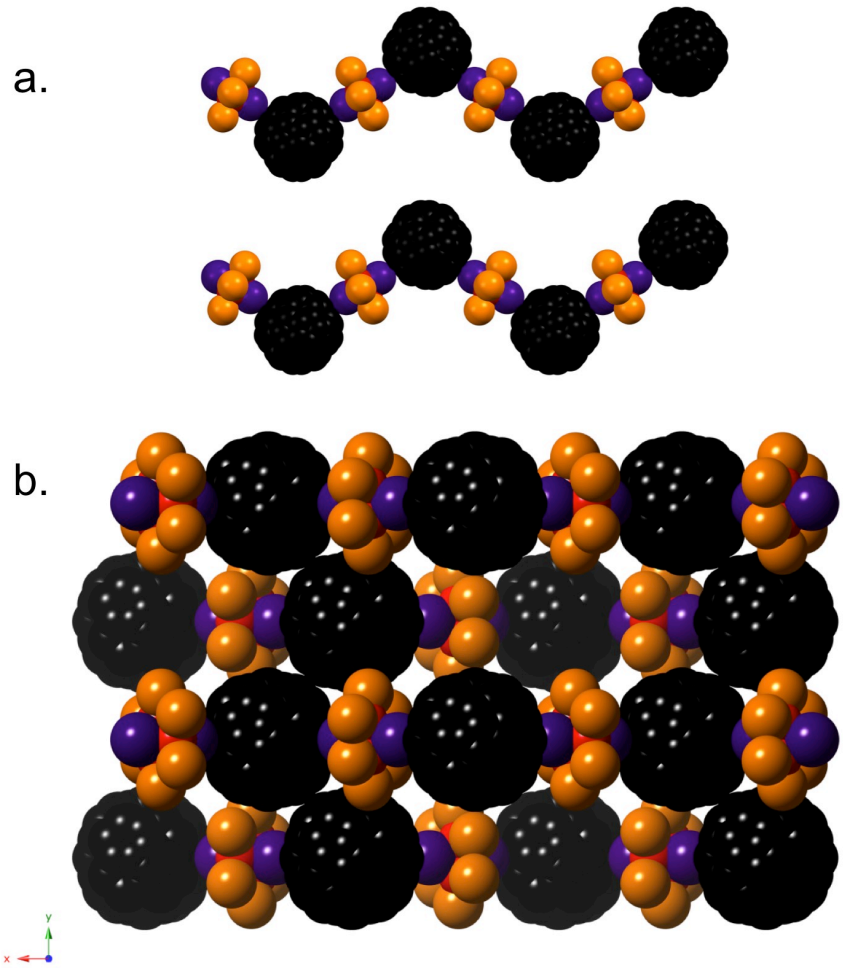


Figure 1.15. Crystal structure of **1**•$C_{60}$ viewed down the a) *b*-axis and b) *c*-axis. Phenyl and methylene substituents and hydrogen atoms have been removed to clarify the view. Nickel, red; iodine, purple; phosphorus, orange; carbon, black.

The most noteworthy features within crystals of **1**•$C_{60}$ are the close-contacts between the triply-bridging capping iodides of the clusters, $(\mu_3\text{-I})_2$, and their neighboring fulleride anions. Compound **1**•$C_{60}$ is the first within this class of superatomic solids with halide cluster capping ligands. Each iodide in **1**•$C_{60}$ exhibits close-contacts to six carbons of one $C_{60}$, with the capping ligand centered over the hexagonal face of the adjacent fulleride. The average distance between the exposed iodide of **1** and the centroid of the

hexagonal face is 3.361 Å (Figure 1.16). This distance is consistent with reported C-I···π halogen bonding interactions.[46,47] Furthermore, the angle $\theta$ between the centroid of the nickel trimer, capping iodide ligand, and centroid of the Lewis-basic hexagonal face is 177.89°, which is close to the frequently observed halogen bonding angle of 180°.[48] These characteristics indicate that the packing of compound **1**•$C_{60}$ is, in part, directed by an inorganic equivalent of this well studied attractive force.[48]

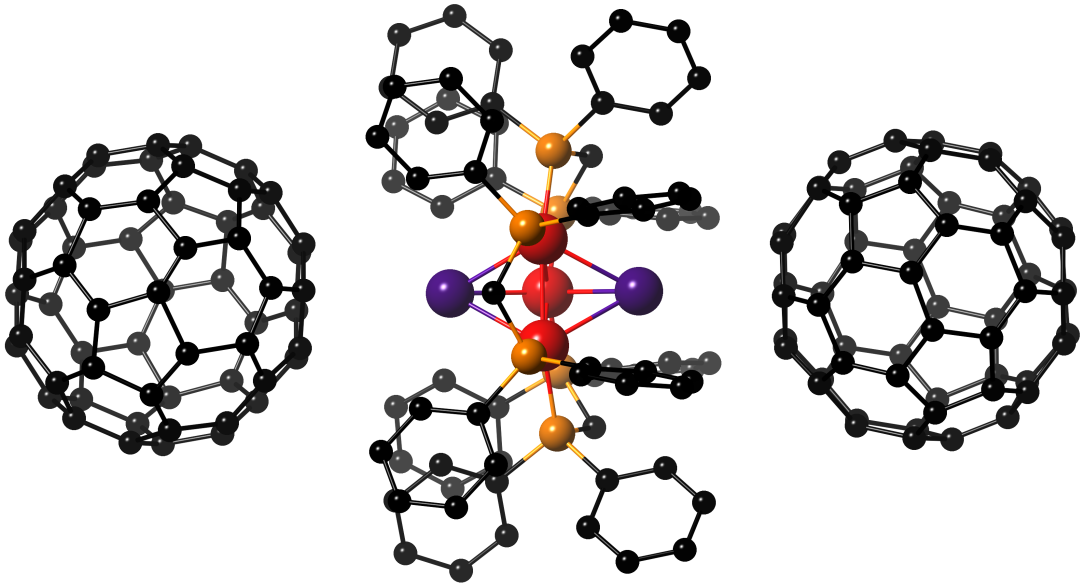

Figure 1.16. Close contacts between iodide capping ligands and hexagonal face of fulleride anions in **1**•$C_{60}$ (hydrogen atoms removed for clarity). Nickel, red; iodine, purple; phosphorus, orange; carbon, black.

1.2.2 Synthesis and Structural Characterization of **2**•$C_{60}$

Cluster **2** was also synthesized according to literature procedure.[41] As for cluster **1**, $Ni(COD)_2$ and dppm were dissolved in toluene to form binuclear A-frame complex $Ni_2(dppm)_3$. This solution was then treated with tri-n-propylphosphine ($PPr^n_3$) telluride (synthesized following literature procedure) which served as a 'Te atom transfer reagent' (Scheme 1.3).[49] The dark brown solution was concentrated under vacuum resulting in precipitation of **2** which was obtained as crystalline solid after recrystallization from 1:1 toluene/hexanes. This solid was then used to form **2**•$C_{60}$ via diffusion of precursor solutions (Scheme 1.2).

Scheme 1.3. Synthesis of Cluster **2**.

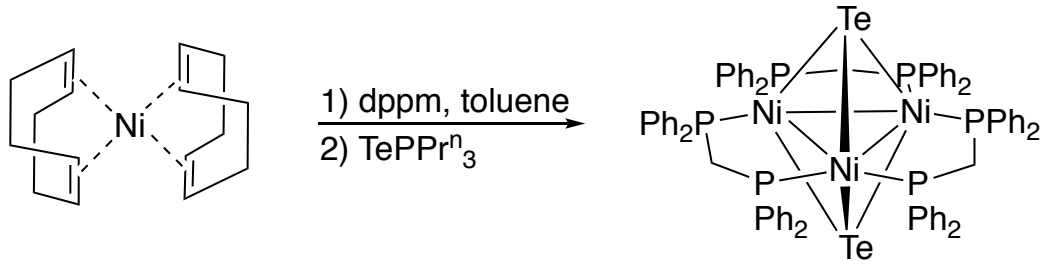


The crystal structure of **2**•$C_{60}$ is remarkably similar to that of the iodide capped binary solid. Charge transfer in the formation of this solid is corroborated through analysis of the nickel atom core within the telluride capped cluster. In **2**•$C_{60}$, the nickel trimer is isosceles rather than equilateral, as expected for neutral **2**, with nickel-nickel distances of 2.570 Å, 2.570 Å, and 2.531 Å. Superatomic solid **2**•$C_{60}$ also crystallizes in the orthorhombic space group *Pnma* and is nearly identical structurally along the *b* and *c*-axes (Figure 1.17). The atom-to-atom distance between adjacent inter-chain fulleride

anions is 3.676 Å with centroid-to-centroid distances of 10.442 Å. Additionally, average close-contacts of 3.532 Å are observed between the telluride capping ligands of **2** and the hexagonal face of the neighboring $C_{60}$. The slightly longer distances observed in **2**•$C_{60}$ are surprising given the slightly larger size of tellurium. However, interactions between chalcogen atom acceptors and Lewis basic donors, known as chalcogen bonding, have been shown to be slightly weaker than related halogen bonding interactions.[50] This chalcogen-based form of σ-hole bonding has been shown to direct crystal packing in the solid state and anion binding in solution.[51–56]

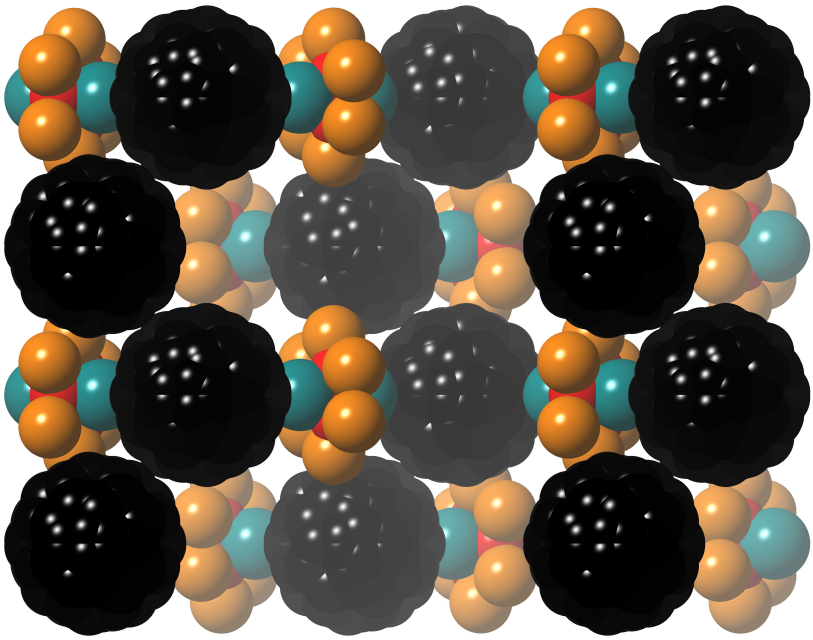

Figure 1.17. Space-filled crystal structure of **2**•$C_{60}$. Phenyl moieties, methylene carbon atoms, and hydrogen atoms have been removed to clarify the view. Nickel, red; tellurium, teal; phosphorus, orange; carbon, black.

### 1.2.3 Structural Characterization of **1**•$C_{70}$ and **2**•$C_{70}$

Increasing the size of the fullerene superatom precursor from $C_{60}$ to $C_{70}$ yields superatomic solids with nearly identical structure as determined by XRD (Scheme 1.2). Both the iodide and telluride containing $C_{70}$ solids crystallize in the orthorhombic space group *Pnma*. The larger diameter of oblong $C_{70}$ causes the *a* and *b* axes within **1**•$C_{70}$ and **2**•$C_{70}$ to be slightly elongated compared to those in **1**•$C_{60}$ and **2**•$C_{60}$. Furthermore, incorporation of the larger fullerene causes the distances between adjacent fulleride anions along the *c*-axis to be shorter, resulting in the formation of singly-bonded dimers $(C_{70}^{-})_2$ (Figure 1.18). This dimerization is a common characteristic of many ionic $C_{70}$ fulleride solids.[57,58] Compounds **1**•$C_{70}$ and **2**•$C_{70}$ also exhibit close-contacts between the capping ligands and fullerides with distances of 3.439 Å and 3.520 Å, respectively. These distances are nearly identical to those observed in the $C_{60}$ ionic solids. This suggests that there is a stabilizing interaction, beyond shape complementarity, directing the assembly of these solids, considering that the size of the phosphine ligand generated cavity remains unchanged.

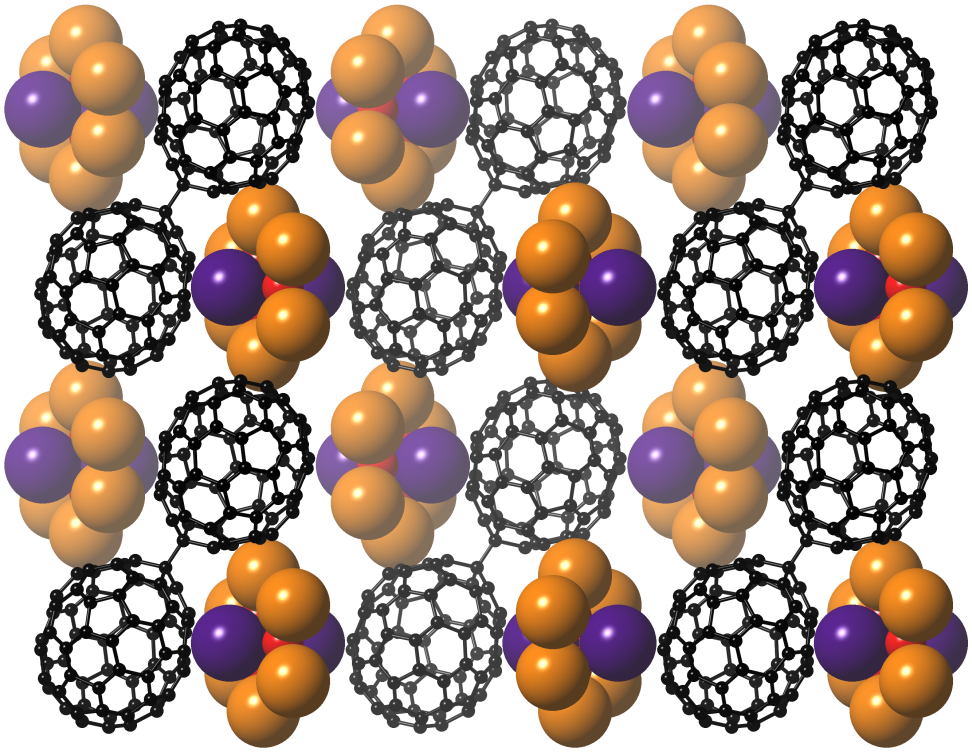

Figure 1.18. Partial space-filling structure of **1**•$C_{70}$ (phenyl substituents, methylene carbons, and hydrogen atoms have been removed for clarity). Nickel, red; iodine, purple; phosphorus, orange; carbon; black.

### 1.2.4 Structural Characterization of 3•$C_{60}$

Cluster **3** was synthesized via modification of the reported procedure for cluster **2**.[41] Rather than synthesize and isolate an external chalcogen transfer reagent such as $TePPr^n_3$, the selenium transfer reagent was generated *in situ* by suspending elemental selenium in a solution of dppm in toluene and allowing the mixture to stir until a homogenous solution was formed. This solution was treated with a red solution of $Ni(COD)_2$ and dppm in toluene (Scheme 1.4). The reaction immediately turned dark brown and was allowed to stir overnight before the solvent volume was reduced and the solid product was isolated via vacuum filtration. Single crystals were obtained from 2:1

toluene/hexanes. This solid was then used to form **3**•$C_{60}$ via diffusion of precursor solutions (Scheme 1.2).

Scheme 1.4. Synthesis of Cluster **3**.

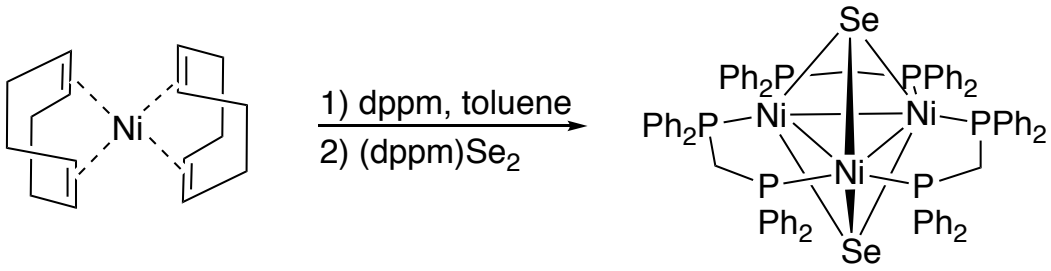


Single crystals of **3**•$C_{60}$ were analyzed via XRD to acquire structural information about the selenide containing superatomic solid. As expected, the packing structure is essentially identical to that of **1**•$C_{60}$ and **2**•$C_{60}$. The nickel trimers within the metal chalcogenide clusters of **3**•$C_{60}$ are isosceles, as observed for the previously mentioned trinuclear cluster-fullerene materials. This distortion from the equilateral core found in the neutral clusters confirms charge transfer between the two superatom precursors. **3**•$C_{60}$ is comprised of zig-zag chains of alternating nickel clusters and fullerides along the *b*-axis with chains of adjacent fullerides along the *c*-axis (Figure 1.19). The atom-to-atom distance between the adjacent inter-chain fulleride anions is 3.841 Å and the centroid-to-centroid distance is 10.414 Å. Furthermore, the average distance between the selenide capping ligands of the clusters and the hexagonal face of the neighboring fulleride anions is 3.600 Å. This distance is longer than what is observed for the iodide and telluride superatomic solids and is in agreement with known chalcogen bonding trends because selenium is known to be a weaker chalcogen bond acceptor than tellurium.[50]

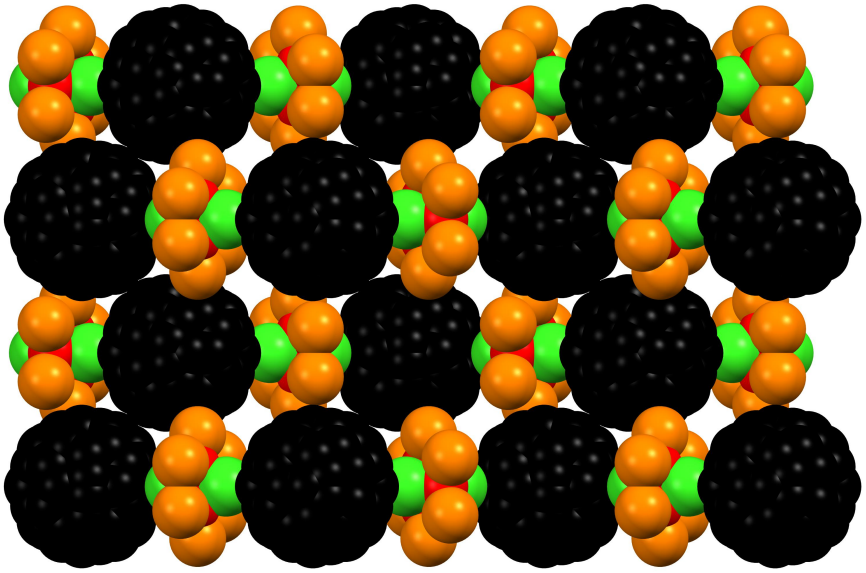

Figure 1.19. Space-filling crystal structure of **3**•$C_{60}$ viewed down the *c*-axis (phenyl substituents, methylene carbon atoms, and hydrogen atoms have been removed to clarify the view). Nickel, red; selenium, green; phosphorus, orange; carbon, black.

### 1.2.5 Synthesis and Structural Characterization of **4**•$C_{60}$

Cluster **4** was prepared in a nearly identical manner as cluster **3**. Rather than form (dppm)$Se_2$ in solution, (dppm)$S_2$ was generated *in situ* by suspending elemental sulfur in a solution of dppm in toluene and allowing it to stir until a clear solution was formed. This solution was treated with a red solution of $Ni(COD)_2$ and dppm in toluene (Scheme 1.5). The reaction immediately turned dark brown and was allowed to stir overnight before the solvent volume was reduced and the solid product was isolated via vacuum filtration. Cluster **4** was recrystallized from 2:1 toluene/hexanes. This solid was then used to form **4**•$C_{60}$ via diffusion of precursor solutions (Scheme 1.2).

Scheme 1.5. Synthesis of Cluster **4**.

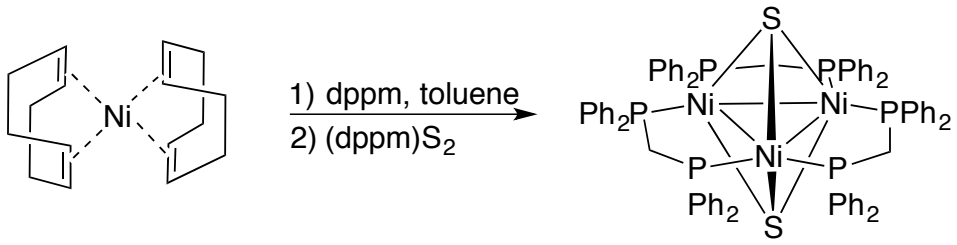


The crystal structure of **4**•$C_{60}$ is nearly identical to that of **1**•$C_{60}$, **2**•$C_{60}$, and **3**•$C_{60}$. Like the aforementioned superatomic solids, charge transfer during solid formation is corroborated through analysis of the bond distances of the nickel cluster core of the sulfide capped cluster. The nickel trimer is isosceles in **4**•$C_{60}$ rather than equilateral, as expected for neutral **4**. The solid crystalizes in the orthorhombic space group *Pnma* and exhibits similar chains of clusters and fulleride molecules along the *b* and *c*-axes (Figure 1.20). The atom-to-atom distance between adjacent inter-chain fulleride anions is 3.658 Å with centroid-to-centroid distances of 10.725 Å. Additionally, average distances of 3.648 Å are observed between the sulfide capping ligands of **4** and the hexagonal face of the neighboring $C_{60}$. These distances are longer than those observed in **1**•$C_{60}$, **2**•$C_{60}$, and **3**•$C_{60}$ and were expected given the weaker chalocogen bonding ability of sulfur as compared to selenium and tellurium.[50]

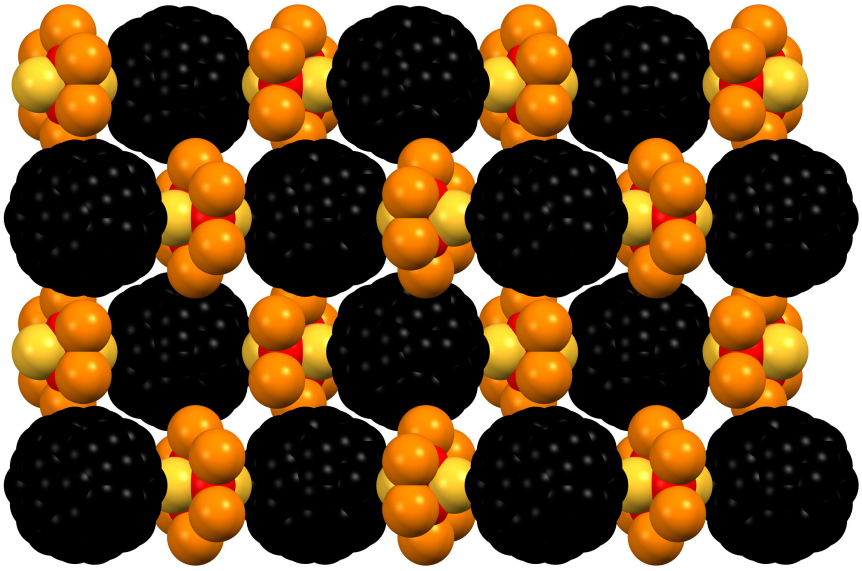

Figure 1.20. Crystal packing of **4**•$C_{60}$. Phenyl substituents, methylene carbon atoms, and hydrogen atoms have been removed for clarity. Nickel, red; sulfur yellow; phosphorus, orange; carbon; black.

### 1.2.6 Attempted Synthesis of **5**•$C_{60}$

The synthesis of cluster **5** was previously reported by Holm *et al*.[42] Cobalt(II) chloride ($CoCl_2$) was suspended in tetrahydrofuran (THF) with triisopropylphosphine. The light blue suspension was treated with one equivalent of bis(trimethylsilyl)sulfide and stirred for two days to yield a black solution (Scheme 1.6). The product solution was concentrated *in vacuo* and **5** was obtained as black crystalline solid from 1:1 THF/acetonitrile.

Scheme 1.6. Synthesis of Cluster **5**.

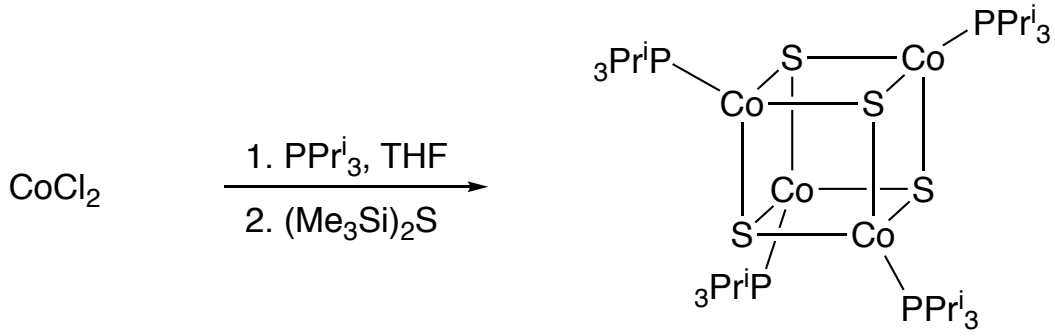


Efforts to synthesize binary solids from cluster **5** and $C_{60}$ proved unsuccessful. The reasoning behind this failure is three-fold. Firstly, the arrangement of the bulky, monodentate diiopropylphosphine ligands does not provide a shape complementary pocket on the cluster for fullerene coordination. Secondly, these phosphine ligands sterically hinder the sulfide capping ligands, essentially blocking all access to the electron-rich cluster core (Figure 1.21). Moreover, reported chalcogen bonding trends indicate that sulfur atoms form the weakest interactions with Lewis basic chalcogen bond acceptors.[50] Finally, cluster **5** lacks the ability to reduce $C_{60}$ fullerene to fulleride anion. This makes spontaneous charge transfer between the two superatoms in solution impossible, hindering the formation of superatomic solids.

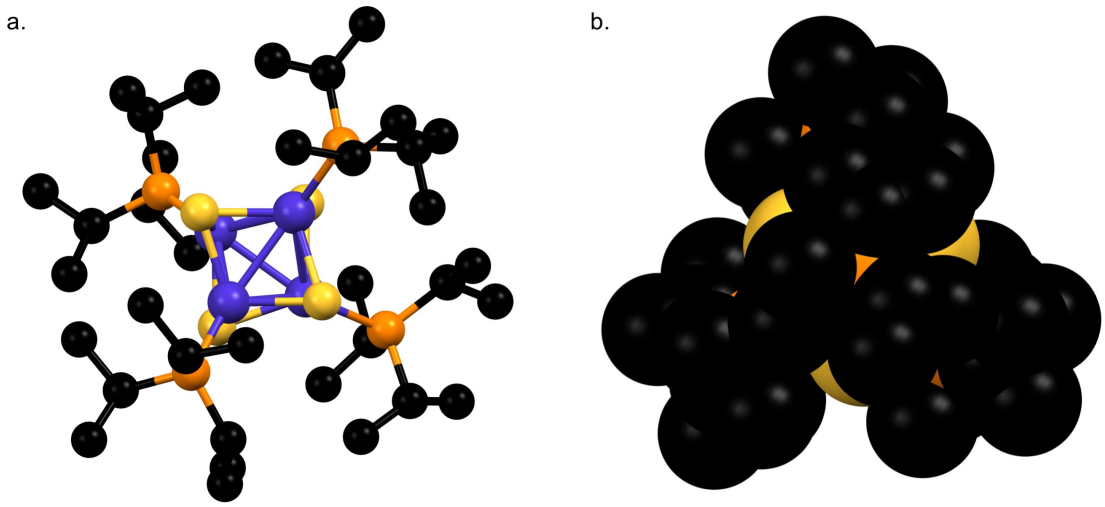


Figure 1.21. a) Ball and stick (hydrogen atoms removed) and b) space filled crystal structure of cluster **5**. Cobalt, blue; sulfur, yellow; phosphorus, orange; carbon, black; hydrogen, white.

### 1.2.7 Structural Characterization of **6**•$C_{60}$

Cluster **6** was obtained by treating a molybdenum precursor cluster, $(NH_4)_2[Mo_3S_{13}]$, with 20 equivalents of $PMe_3$ in THF.[43] The large excess of phosphine is required for this synthesis as the excess sulfur atoms are removed by formation of trimethylphosphine sulfide. Furthermore, the high ratio of phosphine ligand to $[Mo_3S_{13}]^{-2}$ prevents condensation of the $Mo_3$ cores to form larger clusters.[43] During this reaction, the oxidation state of molybdenum is reduced from +4 to +3.33 upon removal of the terminal disulfide ligand.[43] Compound **6**•$C_{60}$ was obtained via diffusion of a solution of **6** in toluene into a solution of $C_{60}$ in 1-methylnaphthalene (Scheme 1.2).

Scheme 1.7. Synthesis of Cluster **6**.

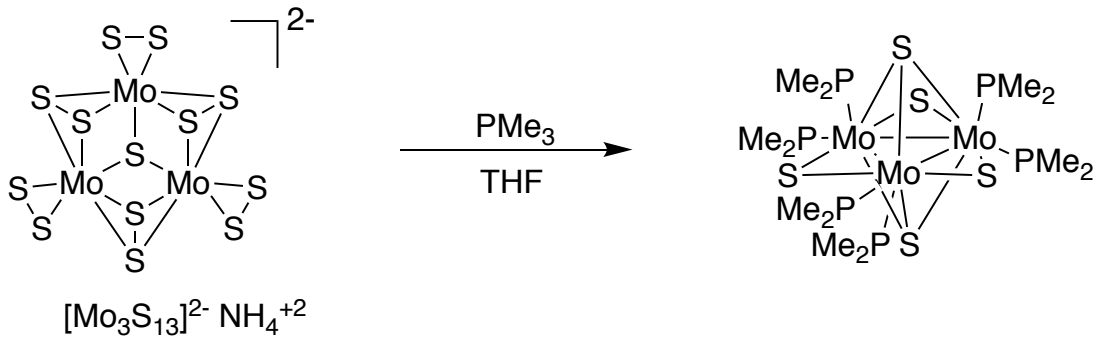


Cluster **6** not only served as superatomic precursor containing five fullerene "coordination sites", but also as a means to determine if interaction between sulfide capping ligands and fulleride anions was achievable in a environment lacking a distinct, phosphine generated binding pocket. Though, the five sulfide capping ligands of **6** are chemically inequivalent.[43] The three capping ligands that lie in the same plane as the molybdenum nickel trimer are doubly bridging ($(\mu_2\text{-S})_3$). Conversely, the remaining two sulfide ligands, above and below the plane, are triply bridging and form bonds to all three molybdenum atoms ($(\mu_3\text{-S})_2$) (Figure 1.22). It was initially believed that this lack of chemical symmetry could limit fulleride "coordination" to the two triply bridging sites. However, XRD experiments have indicated that this was not the case.

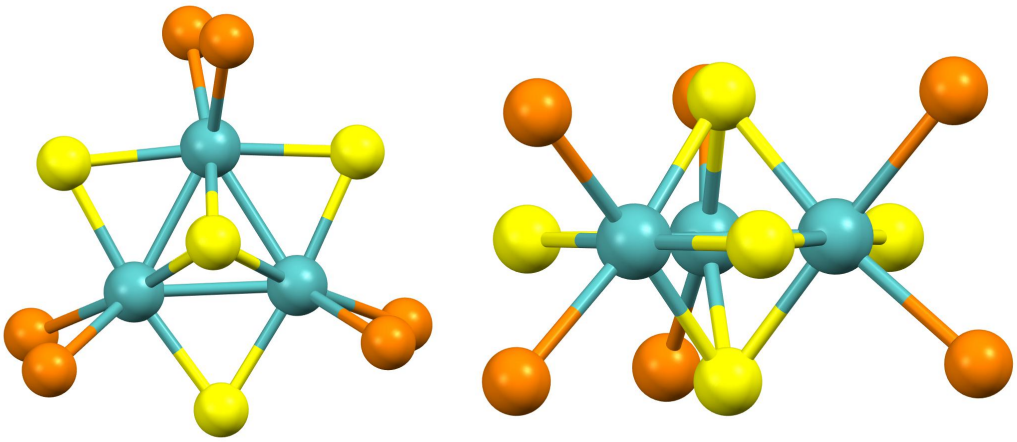

Figure 1.22. a) Top and b) side views of the crystal structure of cluster **6** (methyl moieties removed for clarity). Molybdenum, cyan; sulfur, yellow; phosphorus, orange.

Compound **6**•$C_{60}$ crystallizes in the triclinic space group $P\bar{1}$ and is comprised of mixed stacks of pairs of **6** and dimers of fulleride anions along the *a*-axis. The fulleride dimers are oriented in a hexagonal arrangement above and below each cluster **6** unit as observed through viewing down the *c*-axis. The dimerization of fulleride anions in **6**•$C_{60}$ is prominently displayed down the *b*-axis. Such dimerization has been observed at low temperatures in ionic $C_{60}$ containing solids.[29,59] No close contacts exist between any of the capping sulfide ligands and the fulleride dimers in **6**•$C_{60}$ (Figure 1.23). This lack of interaction stems from a combination of the weak chalcogen bonding donating ability of sulfur and the trimethylphosphine ligands of **6**. The small phosphine ensures that the sulfide capping ligands remain exposed, but generates a much smaller binding cavity for fulleride anions than the bridging phosphine (dppm) in clusters **1**-**4**. The resulting loss of shape complementarity between the two superatoms removes the possibility for ball and socket assembly in the formation of **6**•$C_{60}$.

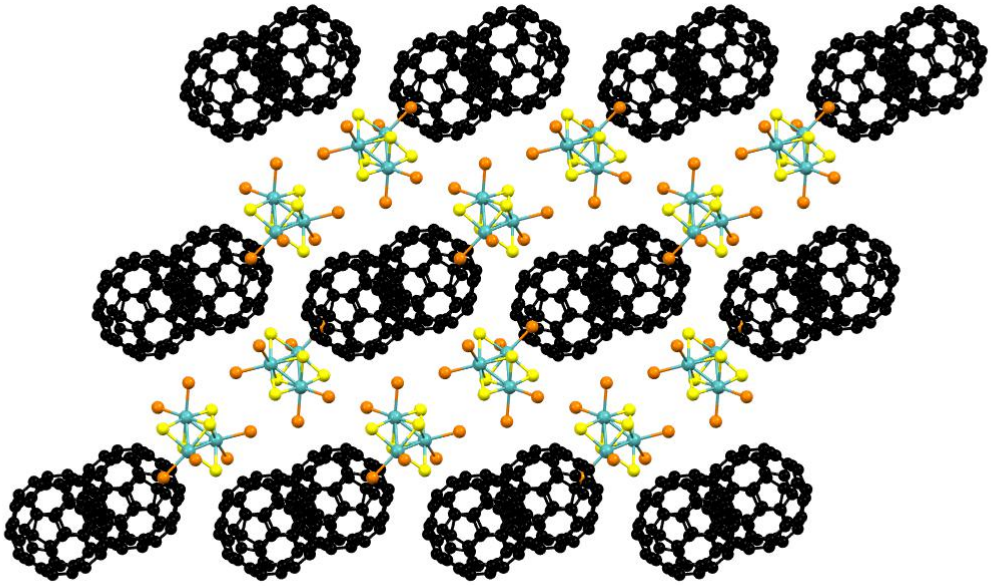

Figure 1.23. Ball and stick representation of crystal packing in **6**•$C_{60}$ viewed down the *b*-axis ($CH_3$ groups have been removed to clarify the view). Molybdenum, cyan; sulfur, yellow; phosphorus, orange; carbon, black.

### 1.2.8 Charge Transfer in **1**•$C_{60}$

Cluster **1** is redox active and electron rich with 52 cluster valence electrons.[40] For this reason, it was expected that **1** would reduce $C_{60}$ during the co-crystallization process. This electron transfer from the trinuclear clusters to $C_{60}$ fullerene was confirmed using infrared spectroscopy. The four IR-active vibrational modes detected for $C_{60}$ ($T_u$ (1-4)) can be used to probe the degree of reduction based on the loss of symmetry as electrons are added, due to Jahn-Teller distortions. Specifically, the $T_u(4)$ mode, which occurs at 1429 $cm^{-1}$ in neutral $C_{60}$, exhibits a diagnostic 34-40 $cm^{-1}$ redshift upon transition to the radical anion.[32] For **1**•$C_{60}$, the peak corresponding to the $T_u(4)$ mode was observed at 1387 $cm^{-1}$ (Figure 1.24). This 40 $cm^{-1}$ downshift is consistent with those reported for known $C_{60}$ fulleride salts.[32]

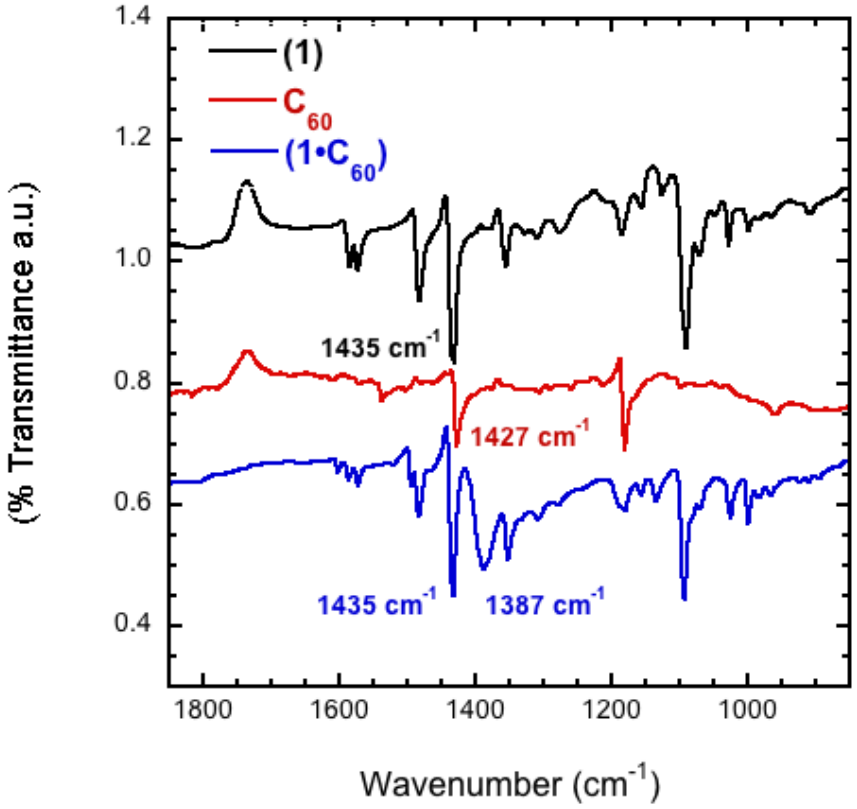


Figure 1.24. Normalized solid state infrared spectra for $Ni_3I_2(dppm)_3 \bullet C_{60}$ (blue), $Ni_3I_2(dppm)_3$ (black), and $C_{60}$ (red).

### 1.2.9 Bonding Interactions in Superatomic Solids

The notable similarities between the arrangement of $C_{60}$ and $C_{70}$ around the trinuclear nickel superatoms (**1**-**4**) suggest that forces beyond shape complementarity may direct the structure of these superatomic solids. This is further corroborated by the presence of contacts shorter than the sum of the van der Waals radii between the capping ligand and fullerene in all structures. The distances of these close-contacts suggest that interactions reminiscent of halogen and chalcogen bonding play a key role in the

assembly of superatomic solids **1**•$C_{60}$, **2**•$C_{60}$, **3**•$C_{60}$, **4**•$C_{60}$, **1**•$C_{70}$, and **2**•$C_{70}$. The influence of these σ-hole bonding interactions was investigated though cocrystallization of 7,7,8,8-tetracyanoquinodimethane (TCNQ) with cluster **1** in toluene. TCNQ is an organic electron acceptor with a low reduction potential (0.21 V vs. SCE in MeCN) that is stable as a monoanionic radical species or as a dianion (Scheme 1.8).[60] Formation of these anionic states is driven by the increase in aromatic character that occurs within the molecule as electrons are donated to the electron poor π system of the quinone (π-acid) (Scheme 1.8).[61] Changing the shape of the electron acceptor, thereby eliminating the ball and socket shape complementarity of the precursors, allowed for observation of the impact of the remaining noncovalent interactions on the resulting binary solid structure.

Scheme 1.8. Selected Bond Lengths and Angles in Neutral, Mono-, and Dianionic TCNQ (Reprinted with permission from ref 56. Copyright 1969 Royal Society of Chemistry.)

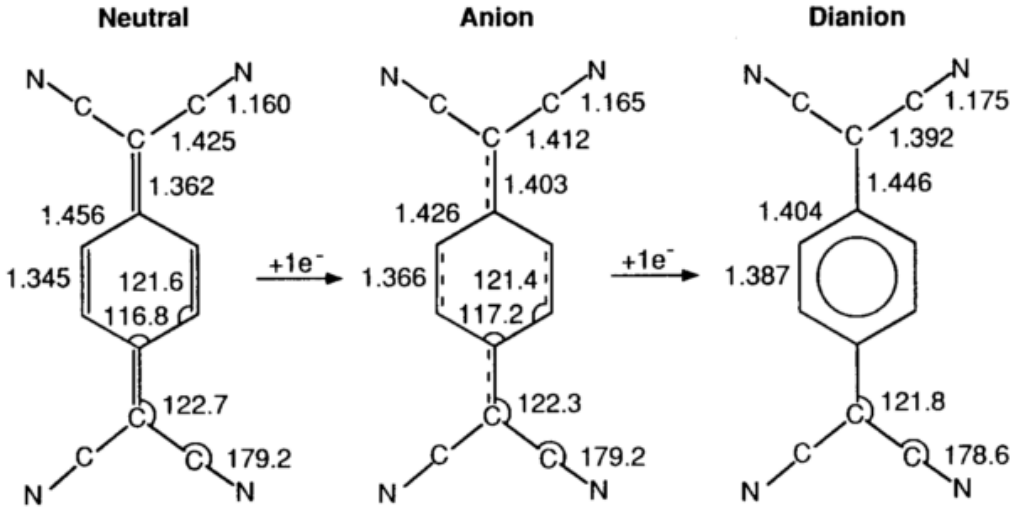

Solutions of cluster **1** and TCNQ in toluene were mixed and left undisturbed for 48 hours. Deep purple, block-like single crystals were isolated by removal of the supernatant and were analyzed by XRD. Full one electron charge transfer between **1** and TCNQ was confirmed through analysis of the bond lengths in TCNQ and the isosceles nickel trimer.[40] Upon acceptance of one electron, the bond between the carbon and nitrogen atoms within the cyano- group of TCNQ and the length of bond between carbon of the six-membered ring and the methylidene carbon both increase.[62,63] The structure of the binary ionic solid **1**•TCNQ differs considerably from the fulleride-based solids, with mixed stacks of **1** and TCNQ along the *b*-axis (Figure 1.25). However, the TCNQ radical anion packs closely to **1** with a close contact (3.679 Å) between one capping iodide and the methylidene carbon of TCNQ (Figure 1.26). The negative charge in TCNQ localizes on this carbon, generating a Lewis basic, halogen bond accepting site on the anion (Scheme 1.8).[64] This provides further evidence that the capping iodides of **1** behave as halogen bond donors within these solid-state materials. Furthermore, this interaction underscores the structure-directing stabilizing force between the capping ligand and the electron acceptor in these hierarchical solids.

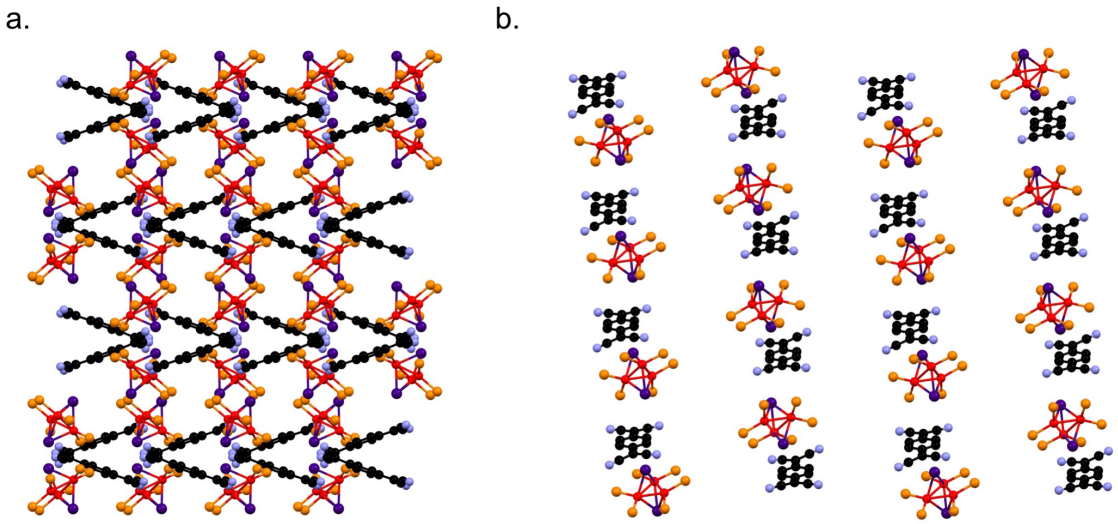


Figure 1.25. Crystal packing of **1**•TCNQ viewed down the a) *a*-axis and b) *b*-axis (phenyl substituents, methylene carbon atoms, and hydrogen atoms removed for clarity). Nickel, red; iodine, purple; phosphorus, orange; nitrogen, lavender; carbon black.

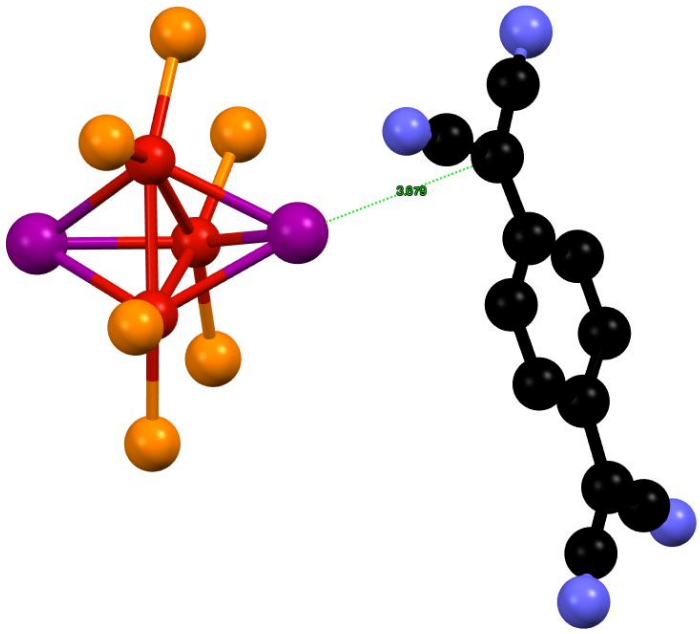


Figure 1.26. TCNQ capping ligand interaction (phenyl substituents removed for clarity). Nickel, red; iodine, purple; phosphorus, orange; nitrogen, lavender; carbon black.

### 1.2.10 Physical Properties of Solid State Fulleride Materials

As discussed, fullerene materials have been shown to exhibit advantageous physical properties such as electron transport, thermal transport, and ferromagnetic ordering. Results of published studies suggest that the presence of these properties is largely dependent upon the selected building block and the arrangement of the fullerene within crystalline assemblies.[17,18,20] In the solid-state, fulleride anions prefer face-centered cubic arrangements. Variation of the structural orientation of fullerene within the solids through crystal engineering approaches can allow for control of the conductivity and magnetism of fullerene-based hierarchical solids.

The face-centered cubic, octahedral packing of fulleride in the rock salt lattice of $[Ni_9Te_6(PEt_3)_8][C_{60}]$ results in a crystalline solid capable of ferromagnetic ordering at low temperatures (Figure 1.27).[18] However, hexagonally close-packed $[Co_6Se_8(PEt_3)_8][C_{60}]_2$ (face-centered cubic unit cell) exhibits no magnetic properties but instead acts as a semiconductor (Figure 1.27).[17] Furthermore, at temperatures below 260 K the unit cell of the solid transitions to a simple cubic structure. This structural change leads to temperature-independent thermal conductivity in $[Co_6Se_8(PEt_3)_8][C_{60}]_2$.[20] The diverse properties observed in this class of binary superatomic solids suggest that the trinuclear nickel cluster-fulleride compounds may offer interesting properties as well.

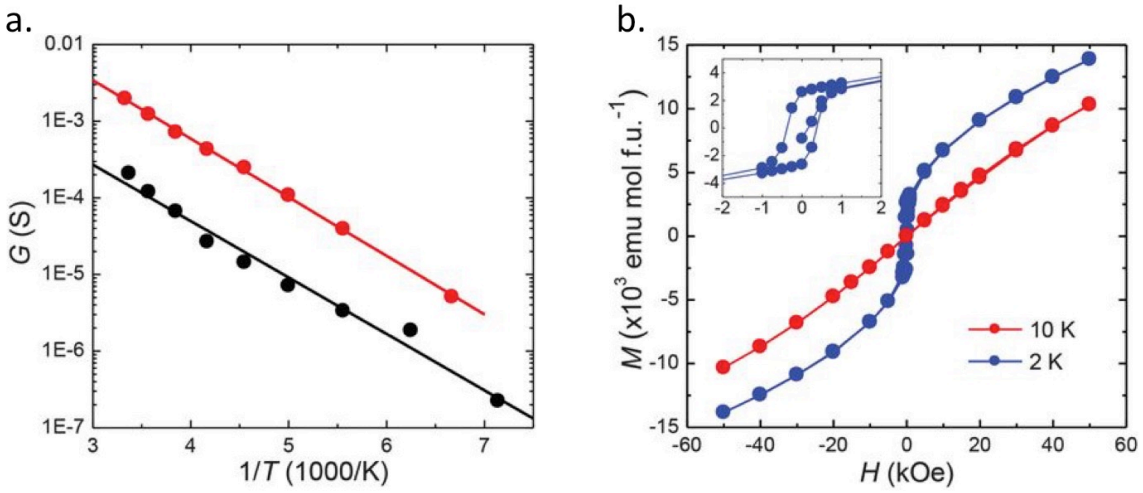


Figure 1.27. a) Semiconducting behavior of $[Co_6Se_8(PEt_3)_8][C_{60}]_2$ and b) ferromagnetic behavior of $[Ni_9Te_6(PEt_3)_8][C_{60}]$. (Adapted with permission from ref. 17. Copyright 2013 The American Association for the Advancement of Science.)

### 1.2.11 Charge Transport in Superatomic Solids

Pressed-pellet conductivity measurements of **1**•$C_{60}$, **2**•$C_{60}$, **1**•$C_{70}$, **2**•$C_{70}$, and nickel cluster precursors **1** and **2** were performed.[65] Ohmic I-V curves were obtained for all samples (Appendix J-M), suggesting metallic conductivity at room temperature. A plot of current density versus electric field strength was used for direct comparison of material conductivities (Figure 1.28).[66] Data indicates that the $C_{60}$ fulleride based superatomic solids (**1**•$C_{60}$ = 2.0 x $10^{-6}$ S $cm^{-1}$; **2**•$C_{60}$ = 8.0 x $10^{-7}$ S $cm^{-1}$) are nearly two orders of magnitude more conductive than their $Ni_3I_2(dppm)_3$ (2.0 x $10^{-8}$ S $cm^{-1}$) and $Ni_3Te_2(dppm)_3$ (1.0 x $10^{-8}$ S $cm^{-1}$) superatom precursors. Furthermore, these superatomic solids display higher conductivities than pure $C_{60}$ single crystals and thin films in the presence of $O_2$.[31] The improved charge transfer in **1**•$C_{60}$ over **2**•$C_{60}$ has been attributed to the inherently better conductivity of the iodide capped cluster as well as the shorter

distances between adjacent fullerides in the superatomic lattice. The $C_{70}$ fulleride salts, **1**•$C_{70}$ and **2**•$C_{70}$, are more conductive than their constituent nickel clusters, both with electrical conductivity values on the order of 1.0 x $10^{-7}$ S $cm^{-1}$. However, these solids are less conductive than the analogous $C_{60}$ materials. It is believed that this decrease in conductivity is due to the minute structural differences between the two lattices (Figures 1.15 and 1.18). Dimerization between adjacent fulleride anions has been observed in both **1**•$C_{70}$ and **2**•$C_{70}$. This could limit delocalization and therefore hinder charge transport across the material.

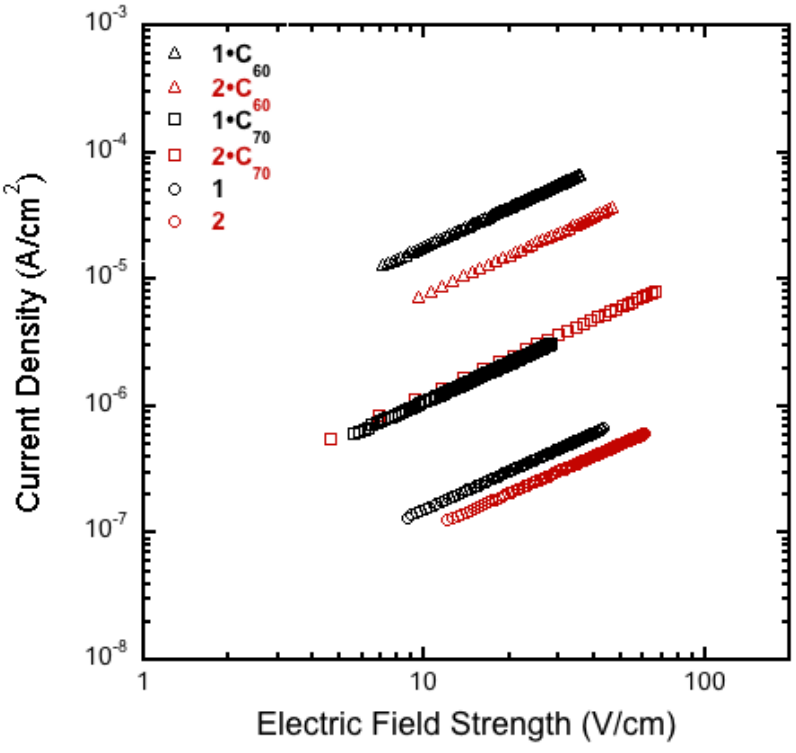


Figure 1.28. Plot of electric field strength versus current density for clusters **1** and **2** as well as their corresponding $C_{60}$ and $C_{70}$ superatomic solids.

### 1.2.12 Magnetic Properties of Superatomic Solids

Although fullerene molecular clusters are known to be diamagnetic, long-range spin coupling has been observed in fulleride salts.[67,68] SQUID magnetometry data was obtained for compounds **1**•$C_{60}$ and **2**•$C_{60}$. Data indicates that the two fulleride based superatomic solids adhere to paramagnetic Curie-Weiss behavior (Figure 1.29). The magnetic susceptibility of these systems can be modeled using Equation 1.1. A diamagnetic contribution ($\chi_D$) of 0.002 emu $Oe^{-1}$ (mol f.u.)$^{-1}$ was used to model both systems. The temperature independent contributions ($\chi_{TIC}$) for **1**•$C_{60}$ and **2**•$C_{60}$, -0.00135 emu $Oe^{-1}$ (mol f.u.)$^{-1}$ and -0.00139 emu $Oe^{-1}$ (mol f.u.)$^{-1}$ respectively, were estimated using the Pascal's constants of the constituent atoms. A Curie constant (C) of 114.94 emu K $Oe^{-1}$ (mol f.u.)$^{-1}$ and a Weiss constant (Θ) of -15.55 K provided the best fit for the susceptibility of **1**•$C_{60}$. A good fit for **2**•$C_{60}$ was obtained with C= 2941.12 emu K $Oe^{-1}$ (mol f.u.)$^{-1}$ and Θ = -13.74 K. Plots of inverse molar magnetic susceptibility indicate that **1**•$C_{60}$ and **2**•$C_{60}$ exhibit weak antiferromagnetic interactions based on the slightly positive y-intercept (Figure 1.28). This is corroborated by the small negative Weiss constants and suggests that individual molecular clusters act as isolated magnetic moments with no long-range ordering.[18]

$$\chi_M(T) = [C/(T - \Theta)] + \chi_D + \chi_{TIC} \qquad (1.1)$$

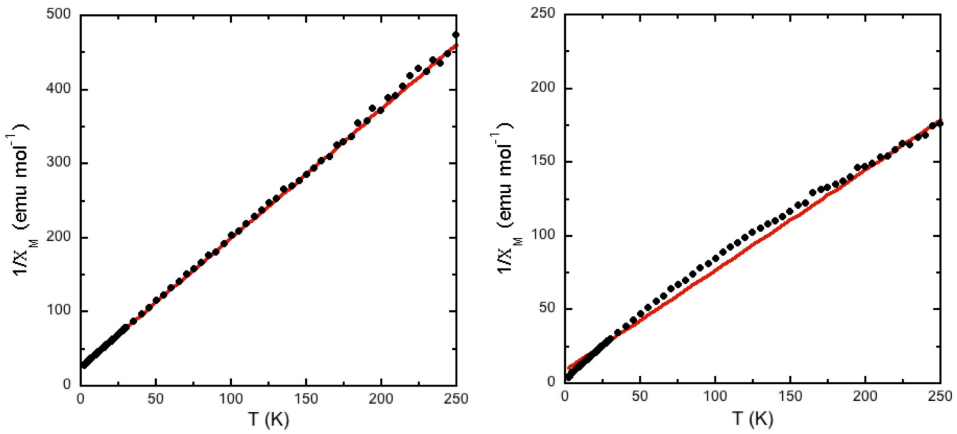


Figure 1.29. Curie-Weiss plots for **1**•$C_{60}$ and **2**•$C_{60}$.

The spin-only effective magnetic moment for a material containing two non-interacting S = ½ spins is 2.45 $\mu_B$ at 300 K.[57] For a similar system with one S = ½ spin $\mu_{eff}$ = 1.73 $\mu_B$.[57] Superatomic solids **1**•$C_{60}$ and **2**•$C_{60}$ were expected to show effective magnetic moments in agreement with a two-spin system. However, moments of 2.06 and 3.39 $\mu_B$ respectively were obtained at room temperature (Figure 1.30). This discrepancy can be attributed to the molecular orbital diagrams for the constituent clusters, **1** and **2**. The reported electronic structure of **1**, determined using MO calculations, contains a fully occupied, doubly degenerate HOMO.[40] Therefore, the HOMO of the 51-electron oxidized species $\mathbf{1}^+$ contains one unpaired electron and the neutral 50-electron nickel telluride cluster contains two unpaired electrons.[40] Kubiak *et al*. report that $\mathbf{1}^+$ exhibits no discernable EPR signal due to rapid spin relaxation in which the single unpaired electron occupies a pair of degenerate orbitals.[40] This relaxation could cause **1**•$C_{60}$ to behave in a manner more closely related to a system containing one unpaired spin, lowering the observed effective magnetic moment. Removal of one electron to yield odd-electron

species $\mathbf{2}^{+}$ leaves one unpaired electron in the HOMO and has been corroborated by magnetic susceptibility measurements using the Evans method.[41]

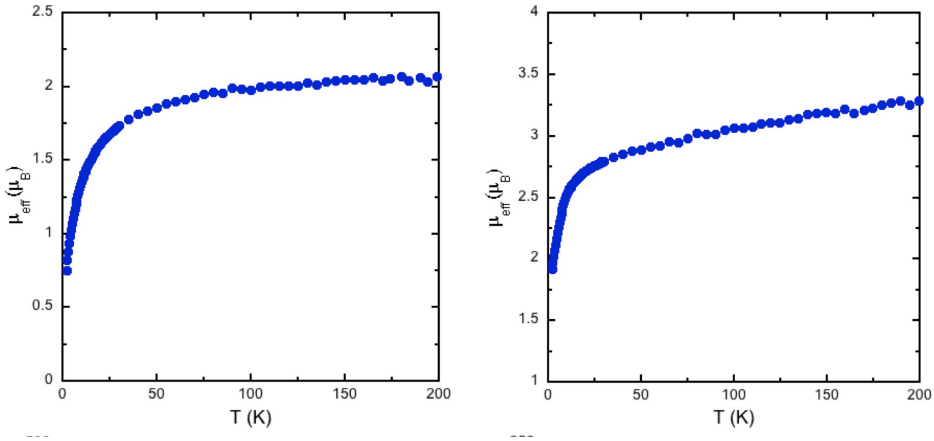


Figure 1.30. Temperature dependence of the effective magnetic moments of **1**•$C_{60}$ and **2**•$C_{60}$.

However, the deviation of the effective magnetic moments for **1**•$C_{60}$ (2.06 $\mu_B$) and **2**•$C_{60}$ (3.39 $\mu_B$) respectively from the expected values can be rationalized considering the oxidation states of the individual nickel atoms in clusters **1** and **2**. Specifically, the core of $\mathbf{1}^{+}$ is comprised of $Ni_3^{3+}$ and the core of **2** is $Ni_3^{5+}$. For this reason, the effective magnetic moment of **1**•$C_{60}$ would be expected to more closely resemble that which would be observed for Ni(I) complexes (2.27 $\mu_B$) and the moment of **2**•$C_{60}$ to be closer to Ni(II) complexes (2.9-3.3 $\mu_B$).[69–73]

## 1.3 Experimental Details

### 1.3.1 General Considerations

All metal cluster precursors were used as obtained from commercial suppliers as follows: nickel(II) iodide (anhydrous) (Strem, 99.5%), bis(cyclooctadiene)nickel(0) ($Ni(COD)_2$) (Beantown Chemical, 96%), diphenylphosphinomethane (dppm) (Sigma-Aldrich, 97%), tri-n-propylphosphine ($PPr^n_3$) (Aldrich, 97%), triphenylphosphine ($PPh_3$) (Sigma-Aldrich, 99%), triisopropylphosphine ($PPr^i_3$) (Sigma Aldrich, 99%), trimethylphosphine ($PMe_3$) (Sigma-Aldrich, 97%). $C_{60}$ and $C_{70}$ fullerene were purchased from Sigma-Aldrich (99.5% and 95%, respectively). Chalcogens (elemental sulfur, selenium, tellurium) were used in powder form as obtained from Acros or Strem. Anhydrous cobalt(II) chloride ($CoCl_2$) (99+%) was used as obtained from Strem and bis(trimethylsilyl)sulfide (98%) was purchased from Alfa Aesar. Ammonium molybdate tetrahydrate ($(NH_4)_6Mo_7O_{24}•4H_2O$) (≥ 99%), ammonium sulfide solution (20 wt. % in $H_2O$), carbon disulfide (anhydrous, ≥99%), and 7,7,8,8-tetracyanoquinodimethane (TCNQ) (98%) were used as purchased from Sigma-Aldrich.

Solvents were obtained from commercial suppliers and purified before use. Toluene, tetrahydrofuran (THF), diethyl ether ($Et_2O$), and hexanes (all obtained from Fisher Scientific) were dried and purified via double column filtration under nitrogen working gas within an M-Braun MB-SPS-800 solvent purification system. Anhydrous acetonitrile (MeCN) (Aldrich, 99.8%) was sparged ($N_2$), degassed (freeze-pump-thaw), and stored over molecular sieves (4 Å, beads 4-8 mesh, Sigma-Aldrich). 1-methylnaphthalene (Aldrich) was dried over $CaCl_2$ (VWR, ACS Grade), sparged ($N_2$),

and degassed (freeze-pump-thaw). Ethanol (EtOH) (KOPTEC, 95%) was used as purchased from VWR. Methanol (MeOH) (Merck Millipore) was purchased anhydrous and was sparged under nitrogen for a minimum of one hour before use. All manipulations were performed under inert atmosphere using standard Schlenk techniques or in a nitrogen-filled glovebox (M-Braun UNIlab Pro SP workstation).

IR spectra were obtained neat under ambient conditions on a Perkin Elmer Spectrum 100 FT-IR Spectrometer.

NMR spectra were obtained in specified deuterated solvents on a JEOL 300 MHz instrument and analyzed using Delta software. Proton decoupled $^{31}P$ spectra were referenced to 85% $H_3PO_4$ as an external reference.

Bright field images were obtained on a PhenomWorld Phenom ProX desktop SEM instrument using a 10kV accelerating voltage. Other parameters were changed as needed and are included with the images.

Conductivity measurements were taken under inert atmosphere using a device comprised of a thick-walled glass capillary (3 mm inner diameter, 9 mm outer diameter, 36 mm length) with two metal rods (3 mm diameter) compressed with a small trigger clamp.[65] Pellet width measurements were taken with a Mitutoyo 293-342-30 Digimatic Outside Micrometer (50.8-76.2 mm) with 0.001 mm resolution. Pellet thicknesses are as follows: **1**, 0.576 mm; **2**, 0.412 mm, **1**•$C_{60}$, 0.701 mm; **2**•$C_{60}$, 0.190 mm; **1**•$C_{70}$, 0.888 mm; **2**•$C_{70}$, 0.087 mm. Potential (-2.5 – 2.5 V, 20 mV step) was applied to the device using a Kiethley 236 Source Measure Unit (SMU) and data was collected with Labview 8.5 software.

Magnetization data was obtained on a Quantum Design MPMS XL7 SQUID Magnetometer. Samples were encapsulated (gelatin, size 4) under Ar and mounted using within the instrument using clear plastic straws. All data was collected with an external applied field of 200 Oe.

Data for all compounds was collected on an Agilent Gemini diffractometer using mirror-monochromated Mo Kα radiation. Data collection, integration, scaling (ABSPACK) and absorption correction (face-indexed Gaussian integration[74] or numeric analytical methods[75]) were performed in CrysAlisPro.[76] Structure solution was performed using ShelXT[77] or SuperFlip.[78] Subsequent refinement was performed by full-matrix least-squares on $F^2$ in ShelXL.[77] Olex2[79] was used for viewing and to prepare CIF files. Many disordered solvent molecules were modeled as rigid fragments from the Idealized Molecular Geometry Library.[80] Rigid-body coordinates for 1-methylnapthalene were taken from a literature structure (CSD reference code ZEBFUH).[81] Rigid-body coordinates for $C_{60}$ were taken from the Idealized Molecular Geometry Library. Rigid-body coordinates for $C_{70}$ were taken from a high-quality, fully ordered literature structure (CSD reference code DUKCET).[82] Rigid-body coordinates for half of a $C_{140}$ dimer were taken from a high-quality unpublished structure.[83]

The crystal structure refinements of $Ni_3I_2$-$C_{60}$, $Ni_3I_2$-$C_{70}$, $Ni_3Te_2$-$C_{60}$, and $Ni_3Te_2$-$C_{70}$ were challenging, and the non-routine details are described here.

For $Ni_3I_2$-$C_{60}$ and $Ni_3Te_2$-$C_{60}$, the fullerene is disordered by symmetry over a mirror plane. A full $C_{60}$ molecule was located as a rigid fragment and subsequently refined with unrestrained coordinates. Anisotropic ADPs were refined but it was necessary to make opposite pairs of atoms (related by non-crystallographic inversion)

equivalent with EADP. Furthermore, two atoms were nearly overlapping when transformed by the crystallographic mirror plane and therefore suffered from unstable ADPs. This pair of atoms was constrained to share common ADP components after transforming by the mirror plane (which multiplies $U_{23}$ and $U_{12}$ by -1).

For $Ni_3I_2$-$C_{70}$ and $Ni_3Te_2$-$C_{70}$, the fullerenes are predominantly (but not exclusively) found in $C_{140}$ dimers. The crystallographic mirror plane at $y$=1/4 passes through the center of each $C_{70}$ unit, so that adjacent dimer chains may have their dimers at the same $y$ height or may be staggered by $b$/2. If the adjacent chains were to order in one or the other of these possibilities, the structure would occur in a monoclinic subgroup of Pnma, either $P2_1/n11$ (adjacent chains staggered) or $P112_1/a$ (adjacent chains eclipsed) (Figure 1.31). Since the systematic absences for the *n*.. and ..*a* glide planes are not measurably violated, it was concluded that the dimer chains are in a disordered mixture of staggered and eclipsed relationships, which means each $C_{70}$ half of a $C_{140}$ dimer is disordered over a mirror plane (Figure 1.32).

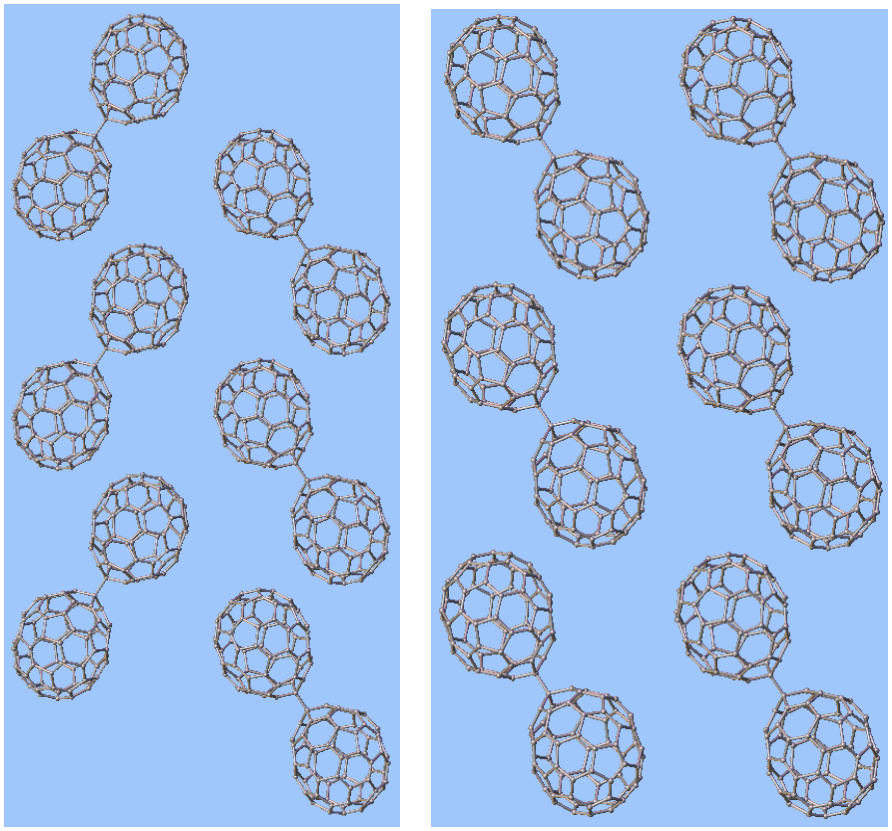

Figure 1.31. Different ordered possibilities for the fulleride substructure of $Ni_3I_2$-$C_{70}$. Left, staggered in $P2_1/n11$; right, eclipsed in $P112_1/a$. Views along 001 with 010 up.

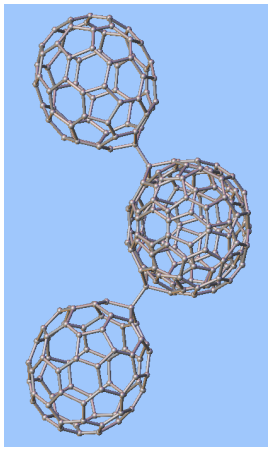

Figure 1.32. $C_{140}$ disordered over mirror plane.

The random relationship of adjacent dimer chains is a consequence of frequent errors in which a $C_{70}$ monomer occurs between two $C_{140}$ dimers. The frequency of defects is 10.4(2) % in $Ni_3I_2$-$C_{70}$ and 25.0(4) % in $Ni_3Te_2$-$C_{70}$. Since the $C_{70}$ monomers are partially occupied and disordered by symmetry, it was difficult to locate them in difference maps. Instead, a rigid $C_{70}$ fragment was placed on the site and rotated randomly in 3 dimensions for several hundred trials. The best agreement factors were obtained when the long axis of the $C_{70}$ monomer was roughly perpendicular to the packing axis of the dimer chains; this arrangement is reasonable because it avoids too-close intermolecular contacts between the $C_{70}$ and the adjacent $C_{140}$s (Figure 1.33).

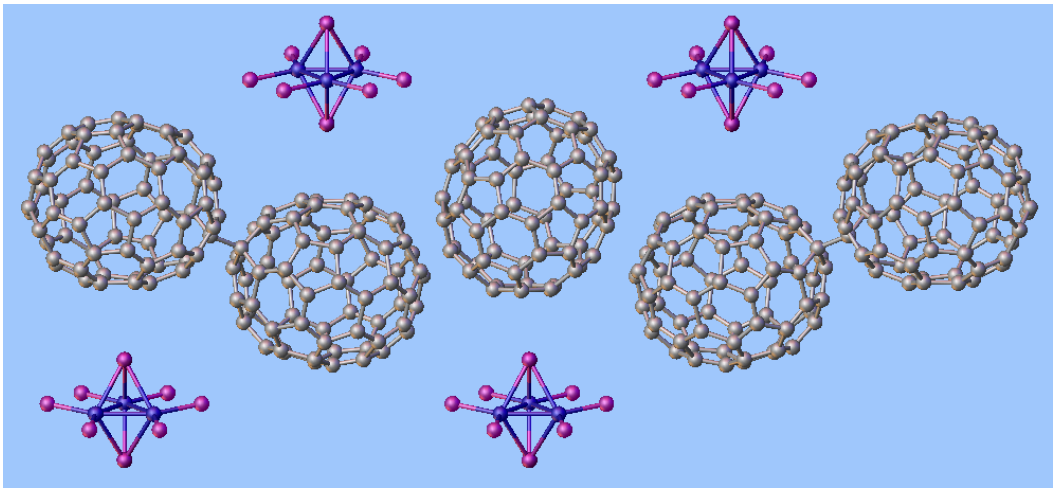

Figure 1.33. A defect in $Ni_3I_2$-$C_{70}$ in which one $C_{70}$ monomer occurs between two $C_{140}$ dimers.

In $Ni_3I_2$-$C_{70}$, the fullerene dimer is also disordered by a rotation around the intercage C-C axis. The minor second orientation of the dimer was also located by random rotation around the bridging bond.

All minor disordered positions of the fullerene in the $C_{70}$ cocrystals were refined as rigid fragments with a single group isotropic ADP.

In all structures, several toluene and 1-methylnapthalene molecules were identified in difference maps, placed as rigid fragments, and oriented by trial and error. In some cases, it was possible to subsequently relax the geometry of the solvent molecules, while stabilizing them with similarity restraints. In all cases, anisotropic ADPs were refined with some combination of RIGU and SIMU restraints.

### 1.3.2 $Ni_3I_2(dppm)_3$ (**1**)

$Ni_3I_2(dppm)_3$ was synthesized via literature procedure reported by Kubiak et al.[40] Anhydrous $NiI_2$ (0.28 g, 0.9 mmol) was dissolved in 60 °C methanol (90-100 mL) and stirred overnight. In a separate vessel, $Ni(COD)_2$ (0.5 g, 1.8 mmol) and dppm (1.04 g, 2.7 mmol) were dissolved in toluene (10 mL) to form a dark red solution. The intermediate solution was added to the $NiI_2$ solution resulting in the immediate formation of **1** as a dark green precipitate. The halide-capped cluster was isolated via filtration and washed with hexanes. The cluster was recrystallized from hot toluene to obtain dark green crystals (1.25 g, 87%). $^{31}P$ NMR ($C_6D_6$) δ -14.0.

### 1.3.3 $Ni_3Te_2(dppm)_3$ (**2**)

$Ni_3Te_2(dppm)_3$ was prepared via modified literature synthesis.[41] $Ni(COD)_2$ (0.58 g, 2.1 mmol) and dppm (0.82 g, 2.1 mmol) were combined in toluene (15 mL) to form a dark red intermediate in solution. A solution of synthesized 'Te atom transfer reagent', $TeP(Pr^n)_3$ (1.80 g, 6.4 mmol), in toluene (10 mL) was added to the intermediate solution.[49] The resulting dark brown solution was stirred overnight before the solvent volume was reduced (8-10 mL) under vacuum resulting in precipitation of **2** as a dark

brown/black solid that was isolated via filtration. The cluster was recrystallized from 2:1 toluene/hexanes (0.72 g, 65%).

1.3.4 $Ni_3Se_2(dppm)_3$ (**3**)

Selenium powder (0.30 g, 3.8 mmol) was suspended in toluene (15 mL) before dppm (0.99 g, 3.8 mmol) was added and the mixture was stirred until all Se was consumed (15 hours). This solution was treated with a solution of $Ni(COD)_2$ (0.58 g, 2.1 mmol) and dppm (0.82 g, 2.1 mmol) in toluene (15 mL) to form a dark brown solution. The reaction was stirred for 12 hours before the solvent volume was reduced under vacuum and the product mixture was filtered. The dark brown solid product was recrystallized from 2:1 toluene/hexanes (0.25 g, 12%).

1.3.5 $Ni_3S_2(dppm)_3$ (**4**)

Elemental sulfur (0.175 g, 5.7 mmol) was suspended in toluene (5 mL) before dppm (1.048 g, 2.7 mmol) was added. All of the sulfur was consumed and a fine white precipitate was formed. This precipitate immediately dissolved with the addition of toluene (50 mL). In a separate vessel, $Ni(COD)_2$ (0.25 g, 0.9 mmol) and dppm (0.35 g, 0.9 mmol) were dissolved in toluene (8 mL). The resulting red solution was added to the reaction flask and an immediate color change to dark brown was observed. The reaction was allowed to stir for 12 hours before the solvent volume was reduced and the concentrated solution was filtered. The isolated dark brown solid was recrystallized from 2:1 toluene/hexanes (0.35 g, 18%).

1.3.6 $Co_4S_4(PPr^i_3)_4$ (**5**)

The procedure for the preparation of **5** has been reported by Holm and coworkers.[42] Anhydrous cobalt(II) chloride ($CoCl_2$) (0.26 g, 2 mmol) was suspended in THF (10 mL) and $PPr^i_3$ (0.64 g, 4 mmol) was added. A solution of bis(trimethylsilyl)sufide (0.43 g, 2.4 mmol) in 10 mL of THF was added to the reaction flask and the mixture was stirred for 2 days before the solvent volume was reduced to obtain a dark brown oil. The brown oil was dissolved in THF and large black crystals were obtained from 1:2 THF/MeCN (0.34 g, 70%). $^{31}$P NMR ($CD_2Cl_2$) δ 58.0.

1.3.7 $Mo_3S_5(PMe_3)_6$ (**6**)

Ammonium polysulfide ($(NH4)_2S_x$) solution was prepared by saturating 130 mL of aqueous yellow $(NH_4)_2S$ with elemental sulfur until a wine-red color was observed. The solution was filtered before use. Red crystalline starting material, $(NH_4)_2[Mo_3S_{13}]$, was synthesized with slight modifications to literature procedure.[84] Ammonium modybdate tetrahydrate ($(NH_4)_6Mo_7O_{24}•4H_2O$) (4.00 g, 3.2 mmol) was dissolved in deionized water (20 mL) and the $(NH_4)_2S_x$ solution was added. The top of the flask was covered with a watch glass and the solution was heated to 93 °C until no liquid remained (3 days). The product mixture was transferred to a frit and washed with deionized water (3 x 30 mL), 95% EtOH (3 x 20 mL), and finally $CS_2$ until all sulfur was dissolved (5 x 10 mL). The remaining red crystalline solid ($(NH_4)_2[Mo_3S_{13}]$) was washed with $Et_2O$ and dried under vacuum for 15 minutes (5.5-5.8 g, 90-95%).

The trinuclear molybdenum cluster, $Mo_3S_5(PMe_3)_6$, was prepared according to literature procedure.[43] The synthesized molybdenum sulfide precursor (0.50 g, 0.68

mmol) was suspended in THF (20 mL) and $PMe_3$ (1.06 g, 14 mmol) was added. The suspension was stirred until a black solution formed (10-15 minutes) before the solution was left undisturbed for 2 days, resulting in the precipitation of black crystalline solid. Crystals were isolated via vacuum filtration, washed with hexanes, and dried *in vacuo* for 3 hours (0.16 g, 25%). $^{31}P\{^1H\}$ NMR ($CDC1_3$): δ 30.4.

1.3.8 **1**•$C_{60}$

Filtered (0.45 μm syringe filter) solutions of $C_{60}$ (11.8 mg, 0.016 mmol) in 1-methylnaphthalene (5 mL) and $Ni_3I_2(dppm)_3$ (25.0 mg, 0.016 mmol) in toluene (5 mL) were layered in a 4-dram vial with a separating layer of toluene (1-2 mL). The vial was left undisturbed for 1 week while the layers slowly diffused resulting in the formation of single crystal rectangular blocks of **1**•$C_{60}$. The supernatant was decanted from the vial and the crystals were washed with hexanes before they were dried *in vacuo* for ~5 h (4.10 mg, 11%).

1.3.9 **1**•$C_{70}$

Filtered (0.45μm syringe filter) solutions of $C_{70}$ (13.3 mg, 0.016 mmol) in 1-methylnaphthalene (5 mL) and $Ni_3I_2(dppm)_3$ (25.0 mg, 0.016 mmol) in toluene (5 mL) were layered in a 4-dram vial with a separating layer of toluene (1-2 mL). The vial was left undisturbed for 1 week while the layers slowly diffused resulting in the formation of single crystal rectangular blocks of **1**•$C_{70}$. The supernatant was decanted from the vial and the crystals were washed with hexanes before they were dried *in vacuo* for ~5 h (9.5 mg, 26%).

1.3.10 **1**•TCNQ

A 0.016 M solution of tetracyanoquinodimethane (TCNQ) (26.0 mg, 0.13 mmol) in toluene (8 mL) was prepared and filtered before use. A 1 mL aliquot of this solution was added to a filtered solution of **1** (20.0 mg, 0.013 mmol) in toluene (5 mL). The resulting solution was shaken gently before it was left undisturbed for 12 hours. Product precipitated from the solution as dark purple crystalline solid.

1.3.11 **2**•$C_{60}$

Filtered (0.45μm syringe filter) solutions of $C_{60}$ (11.8 mg, 0.016 mmol) in 1-methylnaphthalene (5 mL) and $Ni_3Te_2(dppm)_3$ (25.0 mg, 0.016 mmol) in toluene (5 mL) were layered in a 4-dram vial with a separating layer of toluene (1-2 mL). The vial was left undisturbed for 1 week while the layers slowly diffused resulting in the formation of single crystal rectangular blocks of **2**•$C_{60}$. The supernatant was decanted from the vial

and the crystals were washed with hexanes before they were dried *in vacuo* for ~5 h (14.9 mg, 40%).

1.3.12 **2**•$C_{70}$

Filtered (0.45μm syringe filter) solutions of $C_{70}$ (13.3 mg, 0.016 mmol) in 1-methylnaphthalene (5 mL) and $Ni_3Te_2(dppm)_3$ (25.0 mg, 0.016 mmol) in toluene (5 mL) were layered in a 4-dram vial with a separating layer of toluene (1-2 mL). The vial was left undisturbed for 1 week while the layers slowly diffused resulting in the formation of single crystal rectangular blocks of **2**•$C_{70}$. The supernatant was decanted from the vial and the crystals were washed with hexanes before they were dried *in vacuo* for ~5 h (18.8 mg, 48%).

1.3.13 **3**•$C_{60}$

Filtered (0.45μm syringe filter) solutions of $C_{60}$ (8.0 mg, 0.011 mmol) in 1-methylnaphthalene (5 mL) and **3** (16.3 mg, 0.011 mmol) in toluene (5 mL) were layered in a 4-dram vial with a separating layer of toluene (1-2 mL). The vial was left undisturbed for 1 week while the layers slowly diffused resulting in the formation of single crystal rectangular blocks of **3**•$C_{60}$. The supernatant was decanted from the vial and the crystals were washed with hexanes before they were dried *in vacuo* for ~5 h.

1.3.14 **4**•$C_{60}$

Filtered (0.45μm syringe filter) solutions of $C_{60}$ (10.3 mg, 0.014 mmol) in 1-methylnaphthalene (5 mL) and **4** (20.0 mg, 0.014 mmol) in toluene (5 mL) were layered in a 4-dram vial with a separating layer of toluene (1-2 mL). The vial was left

undisturbed for 1 week while the layers slowly diffused resulting in the formation of single crystal rectangular blocks of **4**•$C_{60}$. The supernatant was decanted from the vial and the crystals were washed with hexanes before they were dried *in vacuo* for ~5 h.

1.3.15 **6**•$C_{60}$

Filtered (0.45μm syringe filter) solutions of $C_{60}$ (20 mg, 0.027 mmol) in 1-methylnaphthalene (5 mL) and **6** (25.0 mg, 0.027 mmol) in toluene (5 mL) were layered in a 4-dram vial with a separating layer of toluene (1-2 mL). The vial was left undisturbed for 1 week while the layers slowly diffused resulting in the formation of single crystal rectangular blocks of **6**•$C_{60}$. The supernatant was decanted from the vial and the crystals were washed with hexanes before they were dried *in vacuo* for ~5 h.

## 1.4 Conclusions

### 1.4.1 Conclusions

In summary, new binary superatomic solids were synthesized from metal clusters and fullerene precursors. The fullerene anions pack in the shape complementary cavities provided by the phosphine ligands, resulting in ball and socket packing within in the trinuclear nickel cluster-based solids. Compounds **1**•$C_{60}$, **2**•$C_{60}$, **3**•$C_{60}$, **4**•$C_{60}$, **1**•$C_{70}$, and **2**•$C_{70}$ contain close contacts between the capping ligands (I/Te/Se/S) and the Lewis basic fulleride anions. These contacts are consistent with halogen and chalcogen bonding interactions between the superatomic building blocks.[47,48,50,54] Furthermore, the σ-hole based bonding interactions are corroborated by the results obtained when clusters **5** and **6** were employed as superatomic precursors. Both clusters lack a definitive binding pocket due to the incorporation of bulky (**5**) or small (**6**) monodentate phosphine ligands, decreasing the shape complementarity between the building blocks. In cluster **5**, the bulk of the triisopropylphosphine ligands leaves little of the sulfide capping ligands exposed and hinders fulleride coordination. Additionally, cluster **5** lacks the ability to reduce $C_{60}$, suggesting that the observed bonding interactions may be charge assisted. The weak chalcogen bond donating ability of sulfur may not allow strong enough interaction with fulleride to overcome the lack of shape complementarity in **6**•$C_{60}$, resulting in the dimerized structure obtained.[50] The differing structural arrangements obtained for these binary superatomic solids emphasize the significance of noncovalent interactions in hierarchical assembly.

This work has further demonstrated that the properties of fullerene-based superatomic solids can be tuned though manipulation of the crystalline arrangement of

the fulleride anions. Charge transport measurements of **1**•$C_{60}$, **2**•$C_{60}$, **1**•$C_{70}$, and **2**•$C_{70}$ indicate that all four ionic solids exhibit ohmic conductivity at room temperature and that the $C_{60}$ containing materials are two orders of magnitude more conductive than cluster precursors **1** and **2**. The conductivity of these binary solids is low compared to reported ionic fulleride materials and is likely caused by the high contact resistance associated with the utilized methodology. Additionally, **1**•$C_{60}$ and **2**•$C_{60}$ show no evidence of ferromagnetic ordering as other nickel cluster-fulleride binary solids do, but are paramagnetic with high effective magnetic moments at room temperature.

### 1.4.2 Future Work

This study has provided evidence that the assembly of fullerene-based superatomic solids is directed by noncovalent interactions. However, the exact influence of these interactions as they broadly apply to hierarchical solids remains largely unknown. The future of this project involves extending the scope to include a wider variety of metal chalcogenide superatomic precursors with varied halogen/chalcogen capping and passivating phosphine ligands. Alteration of the metal cluster architecture will result in modification of the size and shape of the phosphine-generated fulleride binding cavities. This can also be accomplished through structural modification of the trinuclear nickel clusters included in this work (**1**-**4**). For example, exchanging the bridging dppm ligand for closely related dmpm ligand (dmpm = $Me_2PCH_2PMe_2$) would increase capping ligand exposure in the trinuclear nickel clusters but would alter the phosphine cavity, potentially resulting in a loss of shape complementarity. Trinuclear nickel clusters containing chelating diphosphine ligands (*i.e.*, dppe = $Ph_2PCH_2CH_2PPh_2$) or monodentate phosphine ligands (*i.e.*, $PEt_3$) are known and may offer a wider range of

cavity morphologies (Figure 1.34).[85,86] Use of these derivative clusters as precursors may yield binary solids with exotic structures and properties.

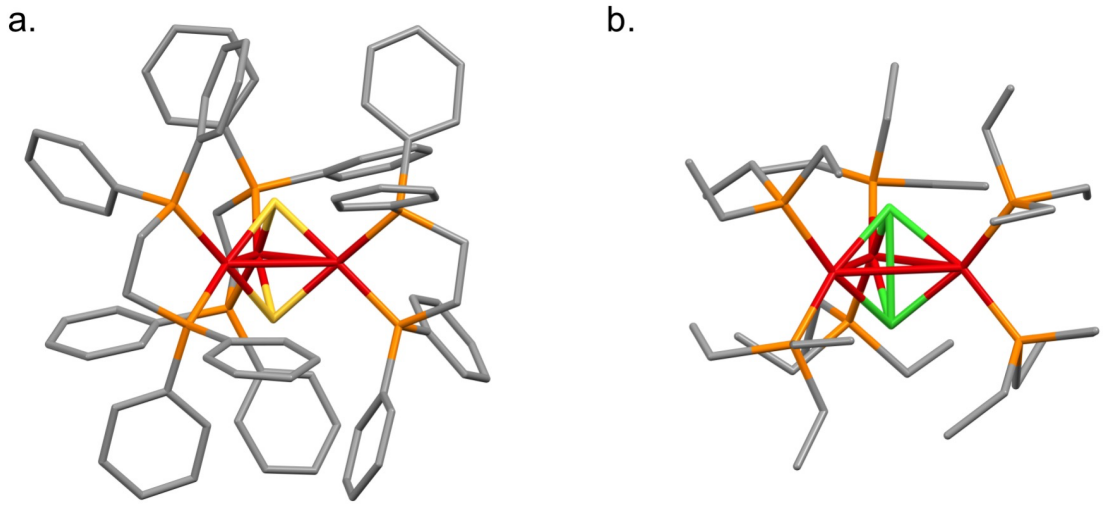


Figure 1.34. Structures of a) $Ni_3S_2(dppe)_3$ and b) $Ni_3Se_2(PEt_3)_6$. Nickel, red; sulfur, yellow; selenium, green; phosphorus, orange; carbon, gray. Hydrogen atoms removed to clarify the view.

Furthermore, continuing superatomic lattice formation with the trinuclear nickel cluster precursors (**1**-**4**) while exchanging the electron acceptor should provide valuable insight into the noncovalent interactions that direct solid assembly. Additionally, treating the trinuclear nickel clusters with shape complementary halogen and chalcogen bond acceptors may allow for determination of the halogen/chalcogen bond donor strength of these metal clusters. Studies including Lewis basic species that lack redox activity as a negative control should confirm the charge-assisted nature of the noncovalent forces observed.

# CHAPTER 2: METAL CHALCOGENIDE CLUSTERS FOR CLUSTER ORGANIC FRAMEWORKS

## 2.1 Introduction

### 2.1.1 Metal-Organic Frameworks

Metal-organic frameworks, known as MOFs, are a class of crystalline coordination polymers that display permanent porosities and exhibit high thermal stability, discrete structures, low densities, and high surface areas.[87] Moreover, the general ease of synthesis and breadth of properties of MOFs make them well suited for a variety of applications. Traditionally, MOFs consist of metal clusters linked through coordination to rigid polytopic organic ligands.[88] These clusters act as nodes in the coordination polymers and are usually self-assembled *in situ*. The structure of the resulting metal cluster, along with the selected organic linker, dictates the structure of the MOF formed. Often, the selected linker features carboxylic acid functional groups that contribute to the overall framework stability by forming strong metal-oxygen-carbon bonds with the cluster nodes.[88] Commonly observed nodes include $Zn_4O(CO_2)_6$ clusters, copper paddle wheel clusters, and $Zr_6O$ clusters.

Yaghi and coworkers pioneered the synthesis of these 3D frameworks. Specifically, MOF-5 is considered to be the first framework to utilize the concept of reticular chemistry.[89] This cubic MOF is comprised of $Zn_4O$ cluster nodes and linear

dicarboxylates. The volume of the pores within this architecture can be controlled through variation of the length, substituting groups, and derivatization of these organic linkers (Figure 2.1). MOF-5 was one of the first frameworks to retain permanent porosity under strenuous conditions (300 ºC, 24 hours) and, upon removal of guest molecules, exhibits pore volumes of 0.61-0.54 $cm^3$ $cm^{-3}$ and a calculated Langmuir surface area = 2900 $m^2$ $g^{-1}$.[89]

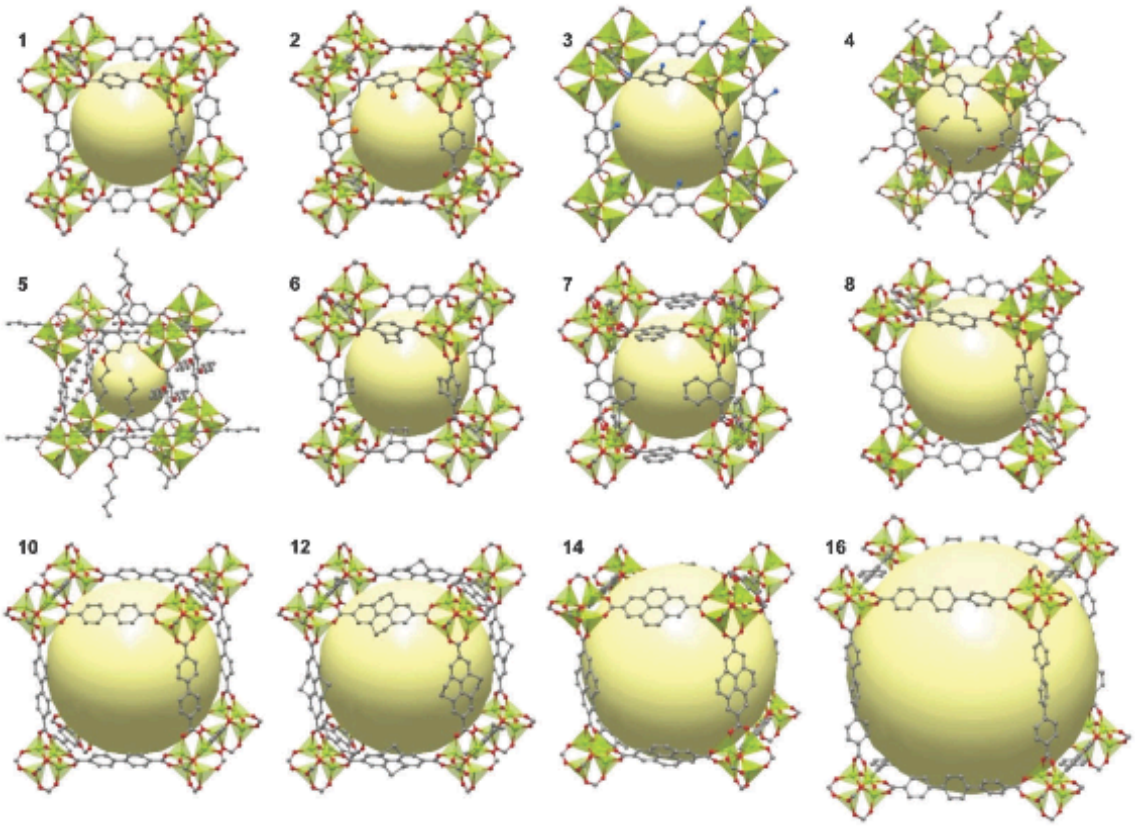


Figure 2.1. Structural variations of MOF-5 topology achieved through utilization of differing organic linkers. (Reprinted with permission from ref 73. Copyright 2015 Royal Society of Chemistry.)

Efforts to expand upon this motif have led to a wide range of functional MOFs. These porous, high surface area materials have been extensively explored for gas storage applications. There is a great interest in hydrogen and methane storage as the gasses act as abundant, clean burning alternatives to fossil fuels. Hydrogen adsorption has been accomplished though both pore size tuning and post synthetic modification of MOFs.[87] Aluminum based frameworks MOF-519 and MOF-520, synthesized by Yaghi, have been shown to efficiently adsorb $CH_4$ better than the current industry standard, HKUST-1.[90] Work has also been done to functionalize MOFs to take up environmentally harmful guest molecules such as $SO_x$, $NO_x$, VOCs, and other industrial byproducts. Navarro *et al.* have prepared a MOF-5 type structure, designed specifically for the capture of nerve and mustard gas agents. The highly chemically, mechanically, and thermally stable framework includes hydrophobic linkers to avoid competitive adsorption of ambient moisture and exhibits a selectivity for small, harmful VOCs that surpassed current MOF and activated carbon standards at the time.[91] The highly tunable MOF motif has also been applied to catalysis. There have been many strategies employed to improve MOF catalytic activity such as incorporation of functionalized organic ligands or coordinatively unsaturated metal centers, post-synthetic modification of inner surfaces, or encapsulation of catalytic nanoparticles or compounds.[87,92,93]

### 2.1.2 Covalent Organic Frameworks

The advantageous properties of MOFs directly led to the design and synthesis of covalent organic frameworks (COFs). In recent years, the formation of these extended solid frameworks through covalent linkages between units has become a popular area of research. These low-density solids are constructed using organic secondary building units

(SBUs) and are stabilized through strong covalent bonds.[94] The utilization of organic building blocks lends covalent organic frameworks a high degree of structural freedom, as pore size and architecture are dependent upon the selected linkers.[95] Furthermore, the functionality of these materials can be tuned through precursor variation. COFs have potential applications in gas storage, catalysis, adsorption, optoelectricity, and organic devices due to their tunable nature and high thermal stability.[95]

Yaghi and coworkers are credited with the initial synthesis of these extended organic solids. It was observed that judicious design and selection of organic SBUs allowed for framework growth in two (COF-1) and three (COF-102) dimensions (Figure 2.2). COF-1 was obtained through use of planar organic building units that form boronate anhydride via condensation of diboronic acid (Scheme 2.1).[94] This platform was based upon the formation of the planar molecule, boroxine ($B_3O_3$), from boronic acid. This framework exhibits high thermal stability, maintaining its structure after removal of solvent guest molecules at 200 ºC. BET analysis indicates that COF-1 possesses a surface area and pore volume within the range of highly porous zeolite materials ($S_{BET}$ = 711 $m^2$ $g^{-1}$, $V_p$ = 0.32 $cm^3$ $g^{-1}$ at $P/P_o$ = 0.90).[94]

Alteration of the organic building blocks allowed Yaghi and coworkers to synthesize the first 3D COFs. This transition primarily involved movement from planar precursors toward tetrahedral building units. Combination of tetrahedral *tetra*(4-dihydroxyborylphenyl)methane (TBPM) and silane (TBPS) with planar hexahydroxytriphenylene (HHTP) yields COFs 102, 103, 105, and 108 (Figure 2.3).[96]

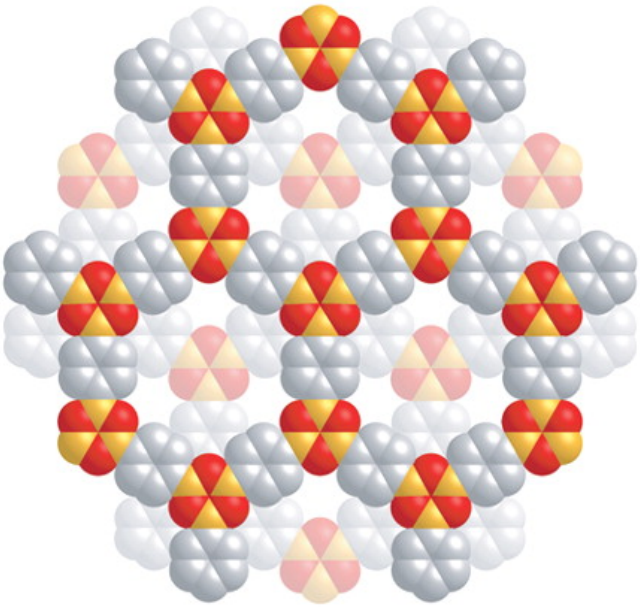

Figure 2.2. Structural representation of COF-1 generated from powder diffraction data viewed down the *c*-axis (carbon, gray; boron, orange; oxygen, red). (Reprinted with permission from ref 80. Copyright 2005 The American Association for the Advancement of Science.)

Scheme 2.1. Synthesis of COF-1. (Reprinted with permission from ref 80. Copyright 2005 The American Association for the Advancement of Science.)

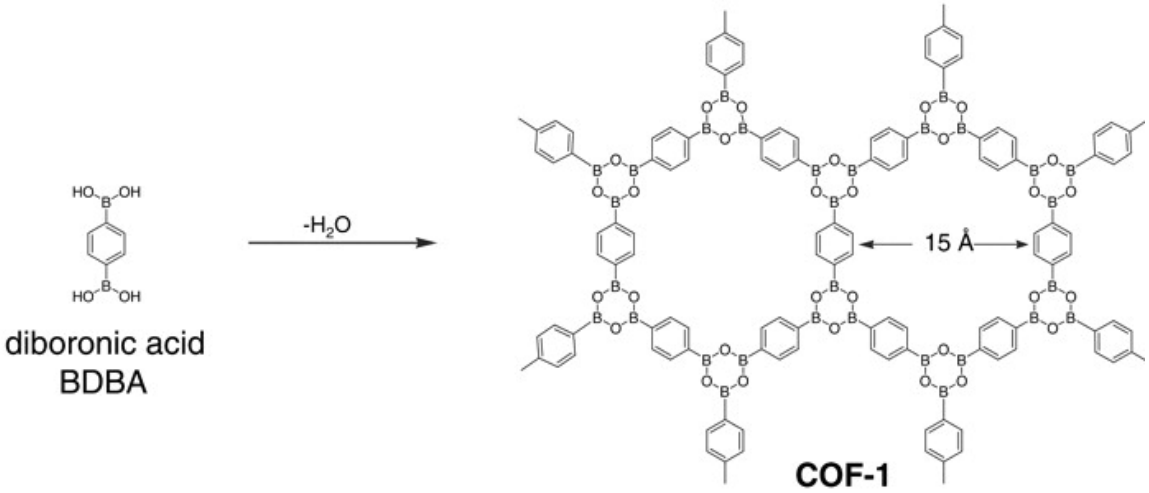

These highly porous, low density frameworks are all thermally stable up to 400 ºC – 500 ºC due to the strong covalent bonds that make up the structure (C-C, C-O, C-B, and B-O).[96] These COFs also exhibit high surface areas: 3472 $m^2$ $g^{-1}$ for COF-102 and 4210 $m^2$ $g^{-1}$ for COF-103.[96] These values surpass those observed for porous carbons and 2D COFs and are comparable to high surface area MOFs.[95] The success of these 3D COFs spurred research into other organic SBUs, such as those capable of forming imine linkages[97], further broadening the rage architectures and applications of 3D COFs.

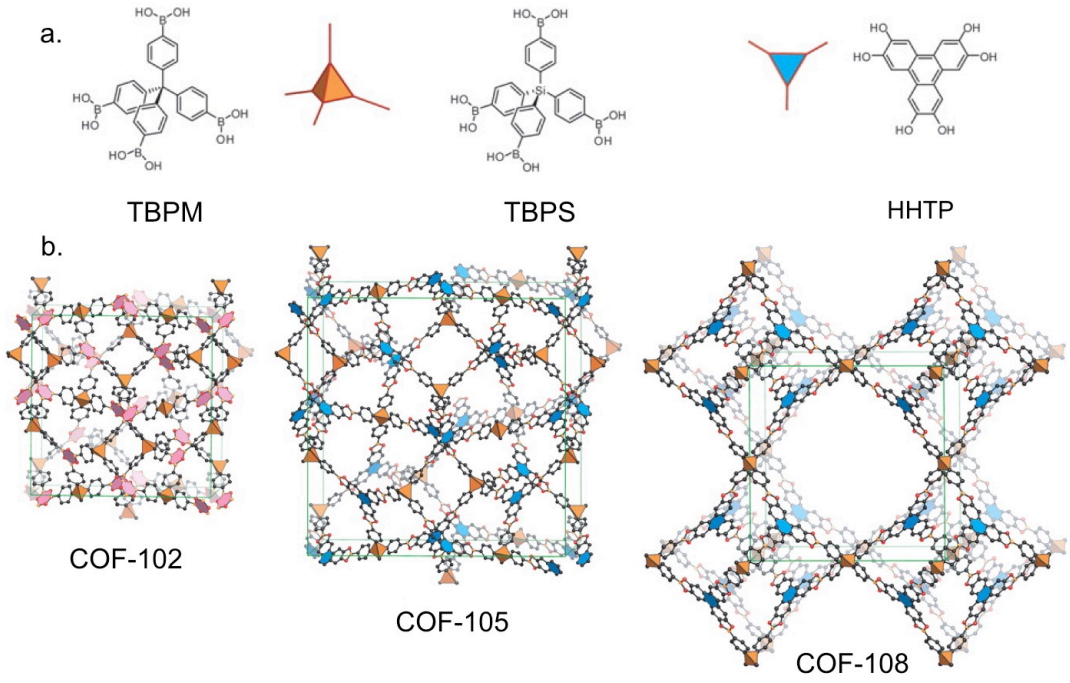


Figure 2.3. a) 3D COF building blocks b) and structural representations of resulting COFs 102, 105, and 108. (Adapted with permission from ref 82. Copyright 2007 The American Association for the Advancement of Science.)

Much like MOFs, the permanent porosity of COFs makes them excellent candidates for gas storage applications. Compiled data indicates that 3D COFs are inherently superior at gas storage than those grown in two dimensions. Selection of organic building blocks with unique electronic properties has also been shown to lead to functional COFs with photoelectric applications (Figure 2.4).[95,98,99] Furthermore, COF properties can be tuned though post modification. Treating 2D COF (CIF-LZU1) with $Pd(OAc)_2$ leads to highly efficient catalysis of Suzuki-Miyaura coupling reactions.[100] The discovery of controlled synthetic methods has led to a rapid increase in COF literature. The bulk of this work can be organized into one of the two structural motifs mentioned: i) two-dimensional and ii) three-dimensional. While the 3D materials exhibit higher surface areas, work on 2D COFs has gained popularity due to the structural similarities to highly functional atomic 2D materials.

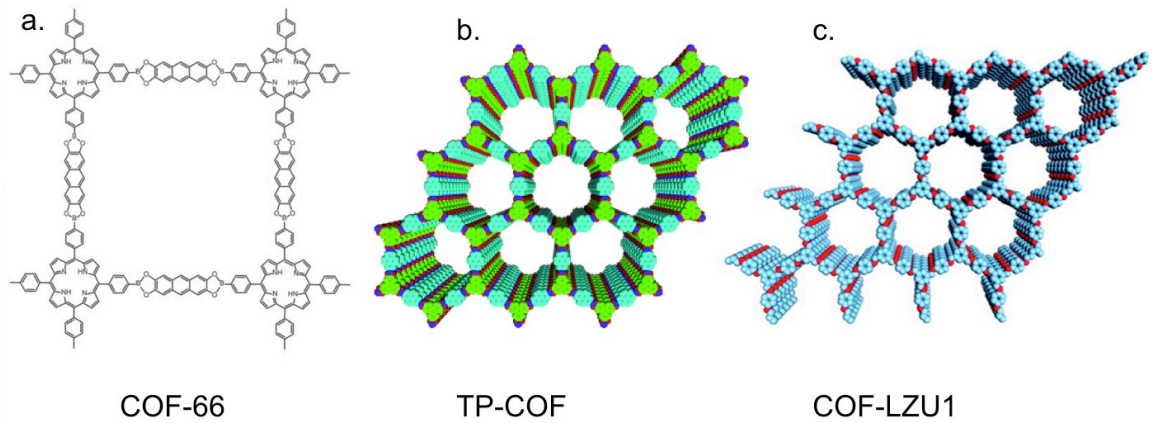


Figure 2.4. Selected a) porphyrin-based (adapted with permission from ref 85. Copyright 2011 American Chemical Society.) b) luminescent (adapted with permission from , ref 84. Copyright 2008 Angewandte Chemie International Edition.) and c) catalytic COFs. (Adapted with permission from ref 86. Copyright 2011 American Chemical Society.)

### 2.1.3 Atomic Two-Dimensional Materials

The high abundance of carbon and the unique properties of its allotropes have made carbon based nanostructures a popular area of research. Graphene, a two-dimensional honeycomb lattice comprised of $sp^2$ hybridized carbon atoms, has been shown to have high surface area, strong mechanical and chemical stabilities, and highly efficient thermal and electrical conductivities.[101,102] These properties have made graphene an excellent candidate for a range of applications (electronics, energy storage, biotechnology).[103] However, large-scale use of the material has been limited by its harsh synthetic conditions and low dispersibility in commonly used solvents. This has led to exploration of other atomic two-dimensional (2D) nanomaterials with honeycomb structures such as hexagonal boron nitride (h-BN), β-silicene, and transition metal dichalcogenides (Figure 2.5).[102]

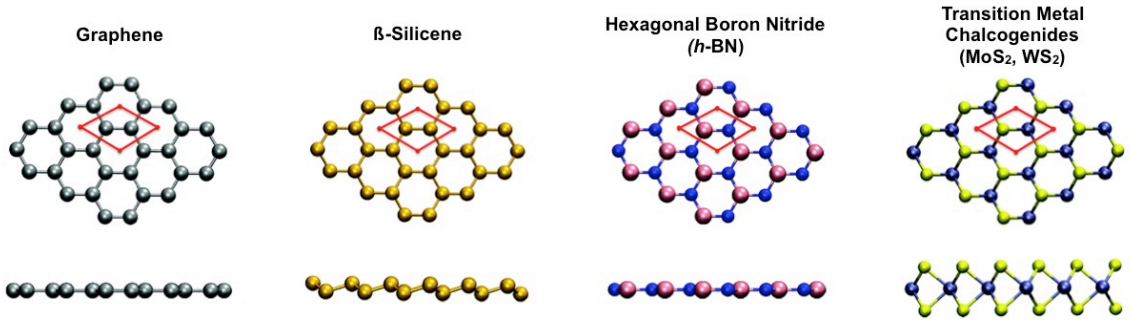


Figure 2.5. Structural representations of selected atomic 2D materials. (Adapted with permission from ref. 88. Copyright 2014 Royal Society of Chemistry.)

While h-BN and β-silicene have been shown to exhibit low density, high thermal conductivity, and high chemical stability like graphene, transition metal dichalcogenides (TMDCs) have gained attention due to their catalytic properties.[104,105] Specifically,

nanocrystals of molybdenum disulfide ($MoS_2$) have been employed as catalysts for the hydrodesulfurization (HDS) of petroleum. $MoS_2$ is a layered bulk solid, comprised of single layered sheets, similar to single graphene sheet stacking in graphite.[106] Unlike graphene, these sheets are three atoms thick, with bridging sulfur atoms above and below the molybdenum centers, and are held together via weak interlayer van der Waals interactions between sulfur atoms (Figure 2.6). Studies have shown that the catalytically active sites reside along the edges of the $MoS_2$ sheets.[106,107,108] However, use of TMDCs on a commercial scale has been limited by the harsh processing conditions and low synthetic yields often associated with atomic materials.

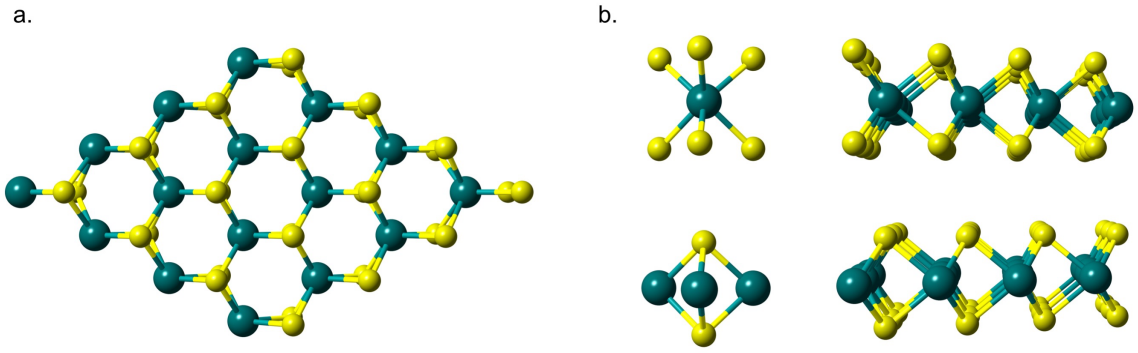


Figure 2.6. Structure of molybdenum disulfide viewed from the a) top and b) side (molybdenum, teal; sulfur, yellow).

### 2.1.4 Coordination Nanosheets (CONASHs)

Metal complex frameworks, known as coordination nanosheets (CONASHs), have emerged as 2D materials with atomic thicknesses achieved through “bottom up” synthesis of coordination bonds. The majority of CONASHs can be obtained from solution state chemical reactions of metal ions with planar organic ligands under ambient

conditions and room temperature (Figure 2.7).[109] This inexpensive technique offers greater opportunities for material design due to the numerous metal-ligand combinations that exist. Inclusion of aromatic thiolene ligands has led to quasi-aromaticity across metal centers resulting in CONASHs with very strong electronic communication throughout (Figure 2.8).[110] The electronic properties of these sheets can be easily tuned through variation of the included metal centers. Notable CONASHs, have been shown to act as chemical sensors, electrical conductors, and catalytic electrodes, as well as hydrogen evolution and ion-exchange materials.[109] Application-based coordination nanosheet research remains a relatively underdeveloped area of study due to its novelty. The knowledge base surrounding metal-organic frameworks (MOFs), covalent organic frameworks (COFs) and their respective applications is significantly greater due to the maturity of the materials.

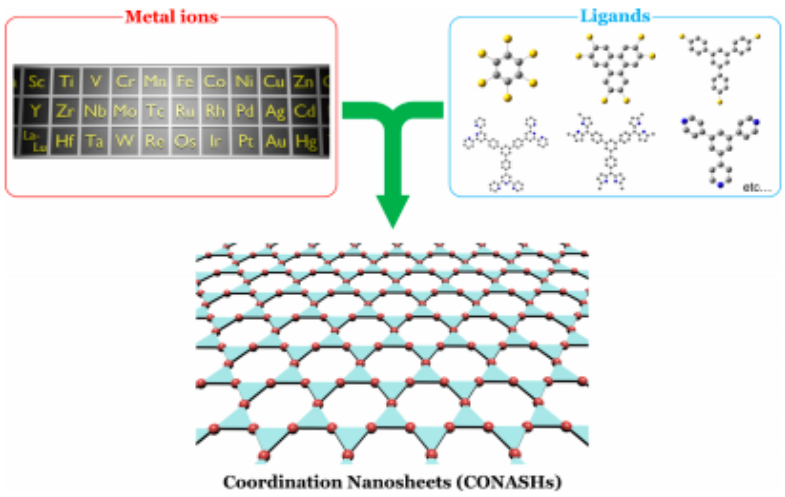


Figure 2.7. Bottom up concept behind the formation of coordination nanosheets. (Reprinted with permission from ref 94. Copyright 2016 The American Chemical Society.)

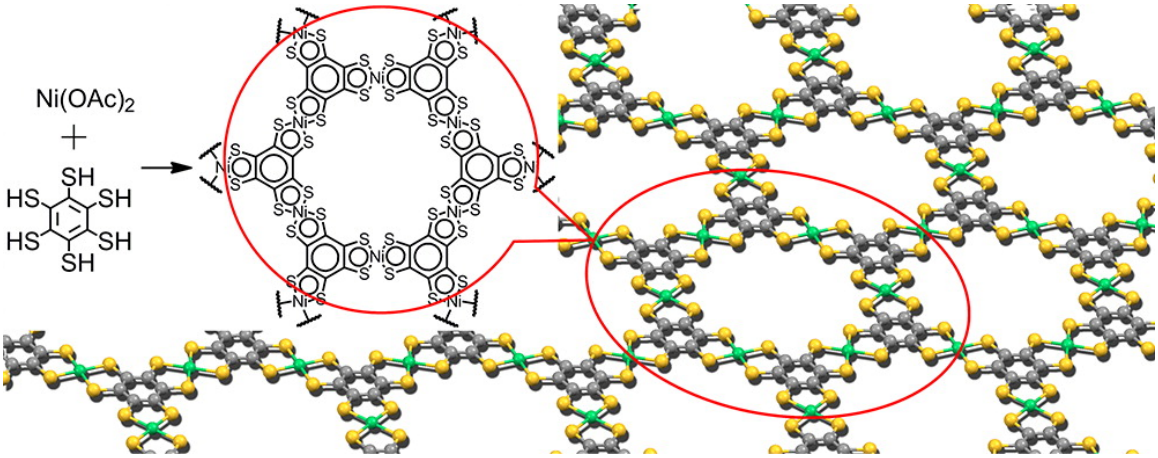


Figure 2.8. Example of coordination nanosheet structure. (Reprinted with permission from ref 95. Copyright 2013 The American Chemical Society.)

### 2.1.5 Research Goals

MOFs, COFs, and CONASHs offer interesting storage opportunities as well as electronic, and catalytic properties. However, strategies for inclusion of *premade* molecular clusters into these frameworks and sheets remain relatively unexplored. The overarching goal of this work is to synthesize a class of functional, porous frameworks by incorporating phosphine stabilized metal chalcogenide clusters.[9,15,111,112] These clusters offer a variety of architectures and unique physical properties such as ferromagnetic ordering and thermal conductivity. Such properties could be programed into high surface area two and three-dimensional materials though cluster utilization.

Furthermore, molecular cluster building blocks offer a unique solution to the challenges of HDS material synthesis. One of the primary objectives of this work is to successfully synthesize a two dimensional, CONASH-like cluster organic framework using bicapped molybdenum clusters as superatomic secondary building units (SBUs). These clusters are specifically targeted due to their structural similarity to $MoS_2$ and

simple room temperature preparation (Figure 2.9).[43] Derivatives of these $Mo_3(\mu_3\text{-}S)_2(\mu_2\text{-}S)_3(PMe_3)_6$ clusters containing functionalized diphosphine ligands should enable formation of 2D materials through existing COF methodologies.

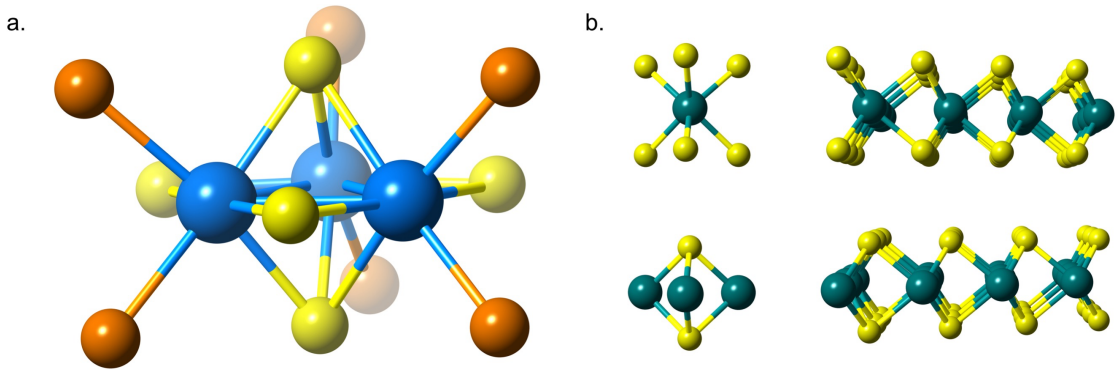


Figure 2.9. Structural comparison of a) bicapped molybdenum cluster and b) $MoS_2$ (molybdenum, blue/teal; sulfur, yellow; phosphorus, orange).

Specifically, replacing the monodentate $PMe_3$ ligands with the chelating diphosphine, 1,2-bis(diphenylphosphino)-4,5-catechol (dpp(CAT) = $(Ph_2P)_2C_6H_2(OH)_2$), should allow cluster organic framework formation with benzene-1,4-diboronic acid. This organic building block covalently links two functionalized clusters through condensation reactions with the hydroxyl moieties. However, the acidic proton of these hydroxyl groups can be abstracted by excess sulfide ($S^{2-}$) during cluster synthesis. Use of a protected diphosphine ligand and subsequent deprotection after cluster formation should mitigate this issue. Therefore, the protected ligand 1,2-bis(diphenylphosphino)-4,5-dimethoxybenzene (dppBzOMe = $(Ph_2P)_2C_6H_2(OMe)_2$) was incorporated. Each cluster can accommodate three of these chelating diphosphine ligands, roughly 120º apart. Hence, a cluster organic framework synthesized in this manner should grow laterally in

the plane of the molybdenum trimer. This two-dimensional growth ensures that the triply bridging sulfide capping ligands remain exposed and should result in porous sheets that are structurally related to bulk $MoS_2$ (Figure 2.10).

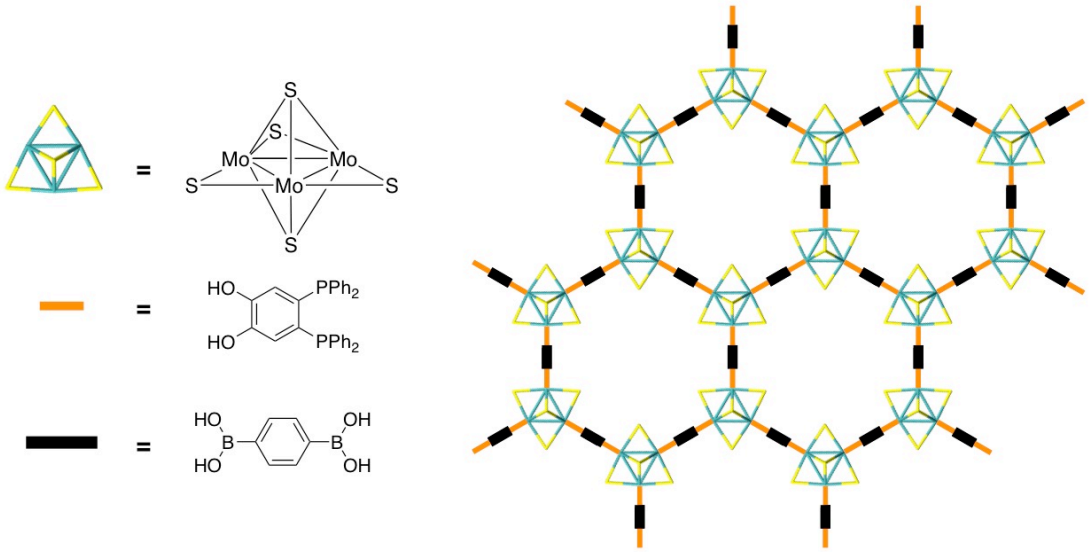


Figure 2.10. Pictorial representation of proposed $Mo_3S_5$ COF (top view).

Additionally, COF synthetic techniques can be used in the formation of three-dimensional porous materials. The second major goal of this work involves using derivatives of the cobalt chalcogenide cluster $Co_4(\mu_3\text{-}S)_4(PPr^i_3)_4$ as superatomic SBUs to form 3D cluster organic frameworks.[42] Use of the smaller, cubane-like cluster rather than the highly tunable $Co_6E_8$ (E = S, Se, Te) motif enables formation of simpler COF architectures, with growth in only four directions. However, isolation of the smaller cluster requires use of bulky phosphine ligands. A ligand containing both isopropyl groups and an aldehyde functionality was designed and synthesized to maintain the required steric conditions while offering opportunities for framework growth. Successful

inclusion of 4-(diisopropylphosphino)benzaldehyde ($PPr^{i}_{2}(C_6H_4CHO)$) into the cobalt cubane cluster should allow for cluster organic framework formation with 1,1'-biphenyl-4,4'-diamine (benzidine) in three dimensions (Scheme 2.2).

Scheme 2.2. Proposed Synthesis for Cobalt Cubane Cluster-based COF.

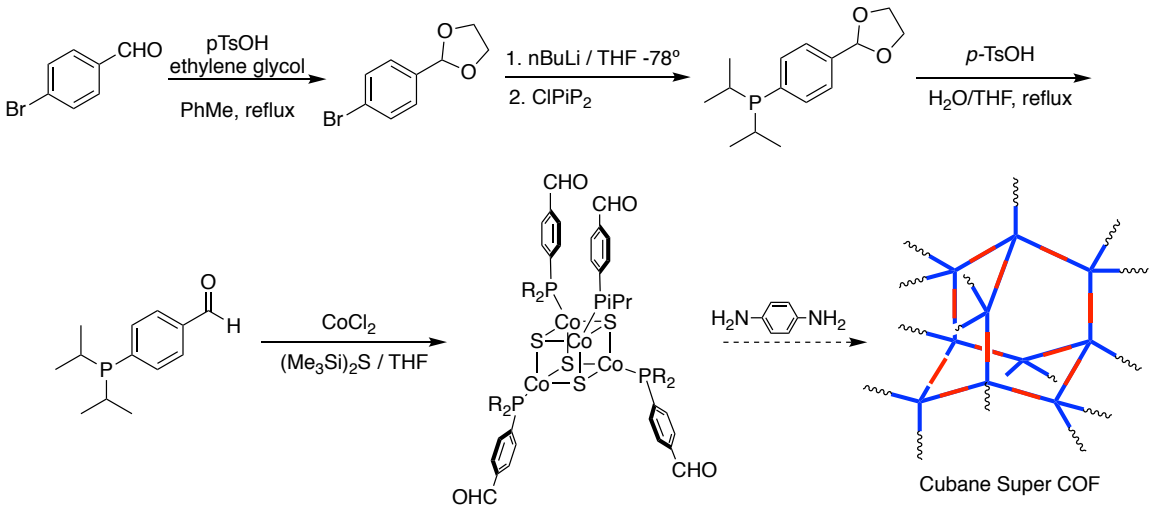

## 2.2 Results and Discussion

### 2.2.1 Synthesis and Characterization of $Mo_3(\mu_3\text{-}S)_2(\mu_2\text{-}S)_3(\kappa^2\text{-}dppbzOMe)_3$ (**8**)

Cluster **8** was obtained by treating molybdenum cluster precursor $(NH_4)_2[Mo_3S_{13}]$ with a solution of dppBzOMe (**7**) in THF (Scheme 2.2). This initially resulted in a dark red suspension that gradually became a black solution over the course of two days. This solution was filtered and crystalline material was isolatioed from 2:1 THF/Hexanes.

Scheme 2.3. Synthesis of Cluster **8**.

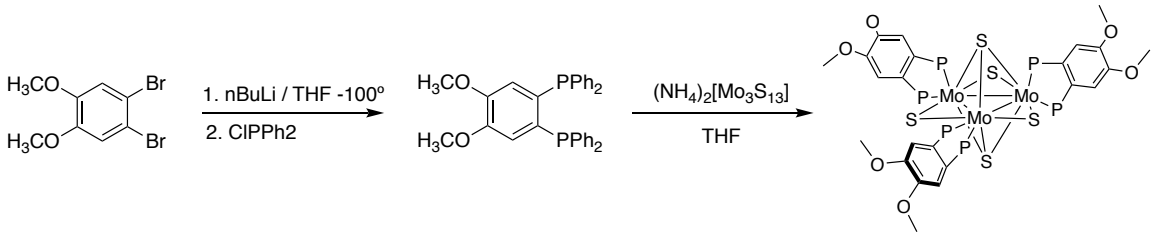


The formation of cluster **8** was confirmed via XRD analysis. As found in the originally reported cluster, the molybdenum atoms are found in an equilateral triangle ($d_{Mo\text{-}Mo}$ = 2.680 Å) (Figure 2.11). Three of the included sulfur atoms surround the periphery of this molybdenum trimer, bridging two adjacent metal atoms in the trimer plane. The metal chalcogenide core is capped by two triply bridging sulfides, centered above and below the molybdenum trimer. Cluster **8** differs from cluster **6** in that the incorporated phosphine ligands are bidentate chelating ligands rather than monodentate ligands. This multidentate coordination causes the phenyl ring backbone of dppBzOMe to

be nearly orthogonal to the plane of the molybdenum core, with some slight distortion due to steric constraints (Figure 2.11).

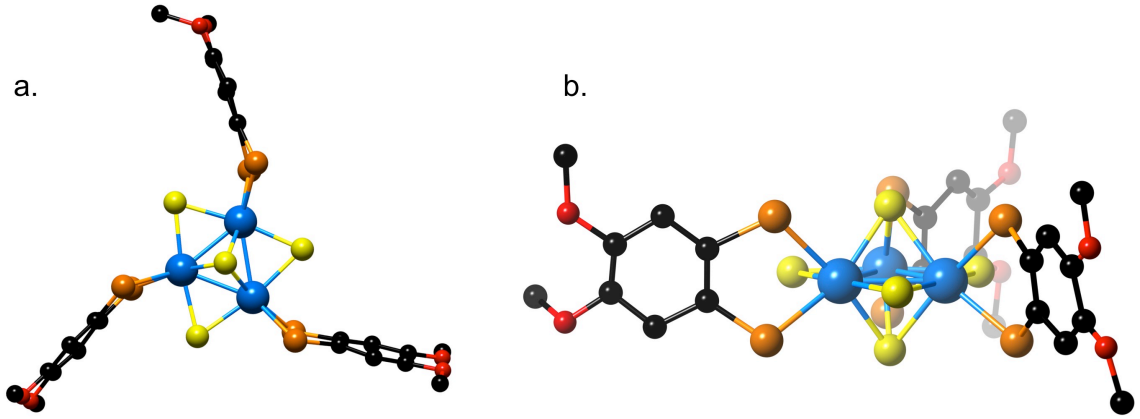


Figure 2.11. Crystal structure of **8** viewed from the a) top and b) side (phenyl substituents and hydrogen atoms removed to clarify the view). Molybdenum, cyan; sulfur, yellow; oxygen, red; carbon, black.

The purity of the solid product obtained was determined via $^{31}P$ NMR spectroscopy. Solid material obtained during the crystallization of **8** was dissolved in deuterated THF ($d_8$-THF) under inert atmosphere. The resulting spectrum contains two sharp peaks, $\delta$ = 43.0 ppm and $\delta$ = -16.6 ppm (Figure 2.12). It was determined that the peak at 43.0 ppm corresponds to (dppBzOMe)$S_2$, which is a byproduct of cluster synthesis (Figure 2.13). The remaining singlet at -16.6 ppm corresponds to cluster **8**, as all of the phosphorus atoms in the cluster are chemically equivalent due to high cluster symmetry. Furthermore, the $^{31}P$ shift for the starting material (dppBzOMe) occurs at slightly downfield at $\delta$ = -12.2 ppm (Figure 2.14).

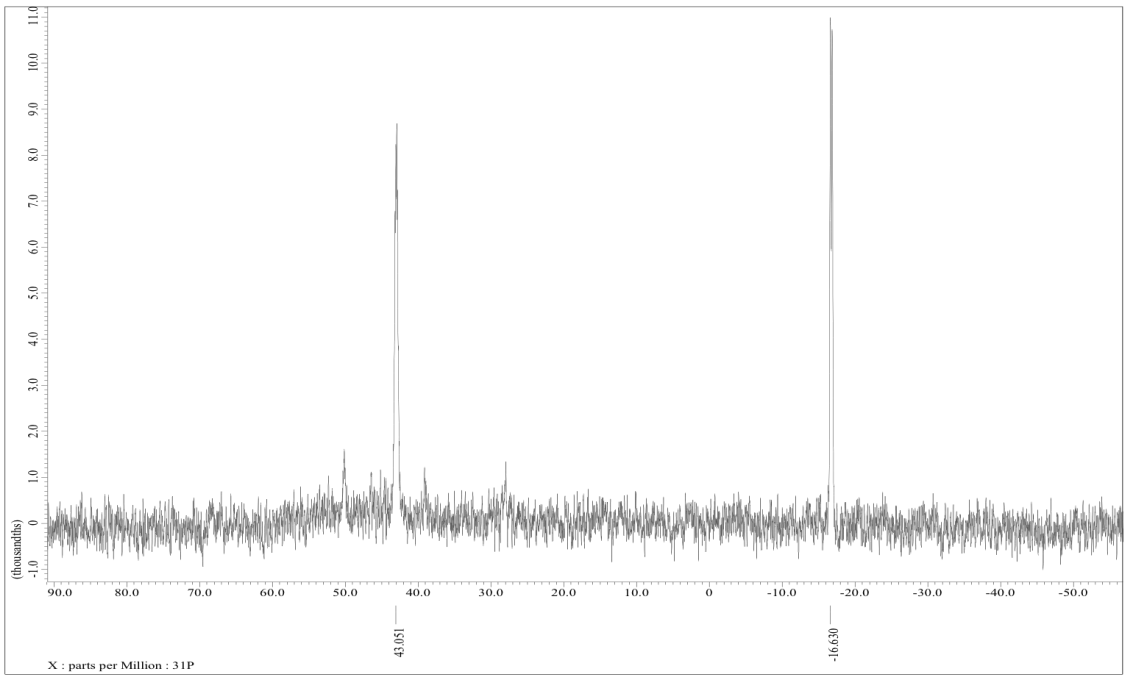


Figure 2.12. $^{31}$P NMR spectrum of solid material obtained from crystallization of **8.**

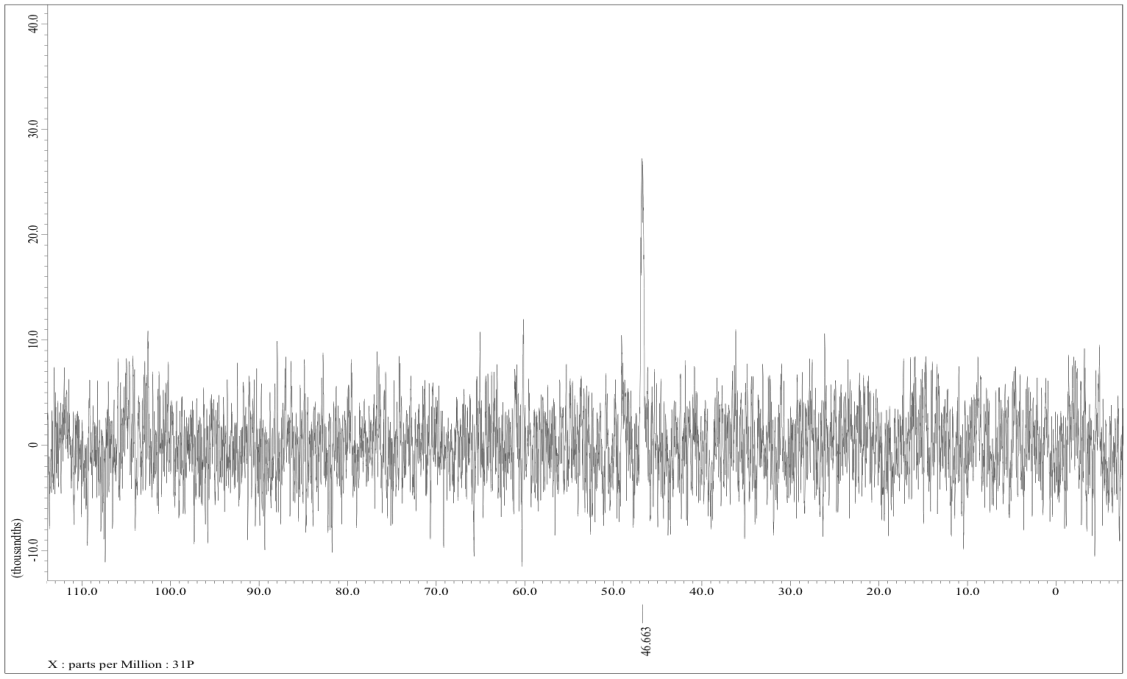


Figure 2.13. $^{31}$P NMR spectrum of (dppBzOMe)$S_2$.

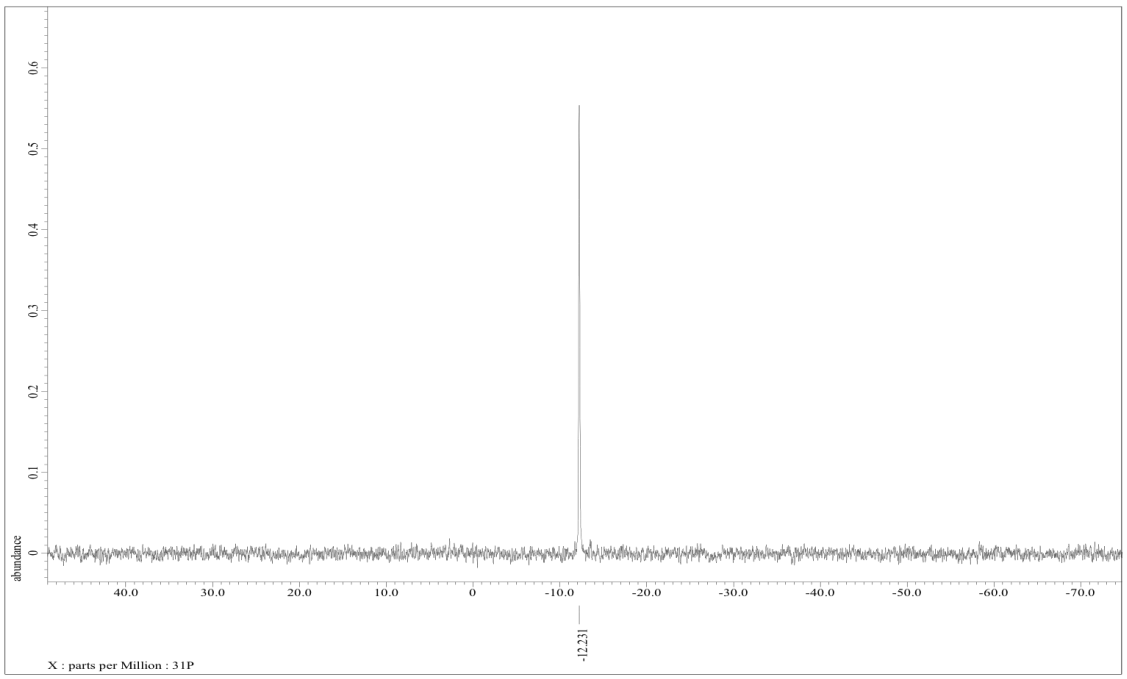


Figure 2.14. $^{31}P$ NMR spectrum dppBzOMe ligand.

The redox activity of cluster **8** was monitored via cyclic voltammetry experiments. In propylene carbonate (PC), the cyclic voltammogram of cluster **8** shows two reversible electrochemical couples (Figure 2.15a). The 50-electron neutral cluster **8** undergoes an oxidation to the 49-electron species $\mathbf{8}^{+}$ at $E_{1/2}$ ($\mathbf{8}^{0/+}$) = -1.166 V versus ferrocene. Similarly, the 48-electron species is formed at $E_{1/2}$ ($\mathbf{8}^{+/2+}$) = -0.22 V against ferrocene. The obtained electrochemical data further corroborates formation of the $Mo_3S_5$ cluster core in cluster **8**. The CV of previously reported, $PMe_3$ containing cluster **6** also exhibits two reversible oxidations (Figure 2.15b). However, cluster **8** seems to be a stronger reducing agent than the parent cluster **6**.

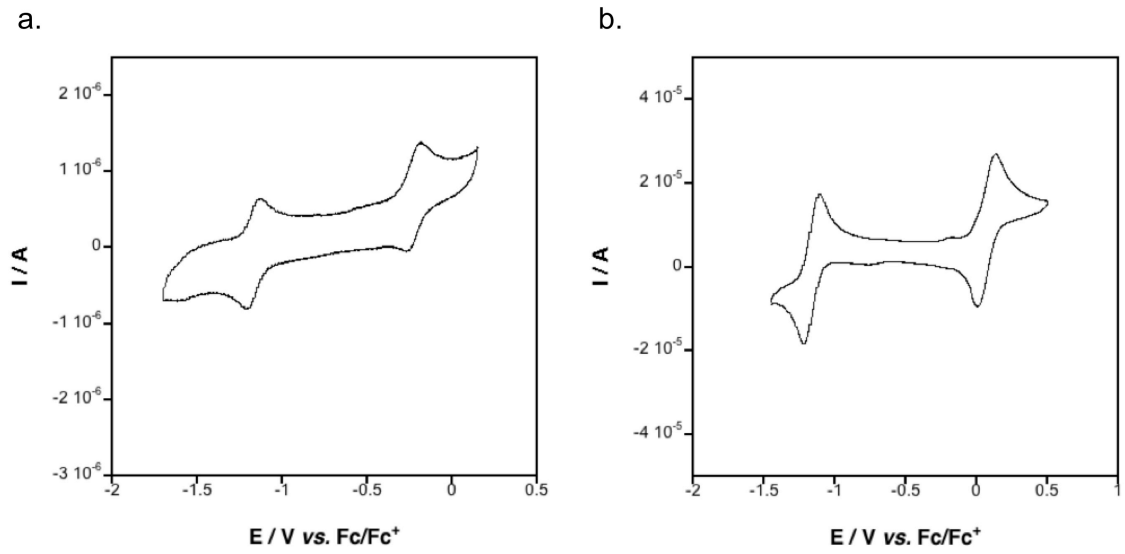


Figure 2.15. Cyclic voltammograms of a) **8** in PC and b) **6** in DCM. Measurements were taken at 100 mV/s against $Fc/Fc^+$ with TBA•$PF_6$ supporting electrolyte, glassy carbon working electrode and Pt counter electrode.

### 2.2.2 Synthesis and Characterization of **11**

The synthesis of cluster **11** was attempted following the literature procedure for closely related cluster **5**.[42] Aldehyde containing ligand, **10**, was dissolved in THF and added to a suspension of $CoCl_2$ in THF. The resulting light blue suspension was treated with bis(trimethylsilyl)sulfide and gradually turned dark brown/black (Scheme 2.4). Solvent removal resulted in a dark brown/black oil. However, crystalline material could not be obtained from this oil after various crystallization attempts.

Scheme 2.4. Proposed Synthesis of Cluster **11**.

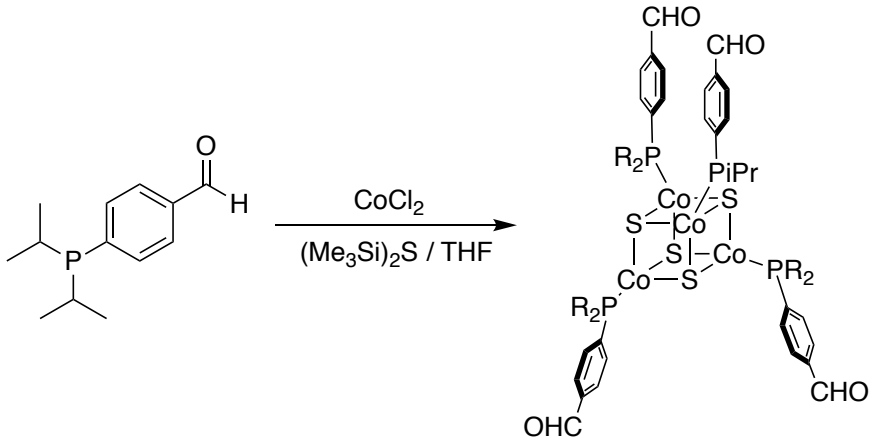


Due to the lack of crystalline material, NMR experiments were completed in an attempt to identify product species. $^{31}P$ spectra of the original cobalt cubane cluster reported by Holm *et al.* (**5**) and the proposed cluster (**11**) were taken in $CD_2Cl_2$. Although the structure and electrochemistry of **5** were reported, NMR data for the cluster was unknown. Single crystals of **5** were dissolved in the selected solvent and transferred to an NMR tube under inert atmosphere. Two phosphorus shifts were observed in the resulting spectrum: $\delta$ = 20.9 ppm and $\delta$ = 58.0 ppm (Figure 2.16). The first shift corresponds to free triisopropylphosphine, a precursor to **5**. The structure of **5** was confirmed via XRD analysis upon crystallization. Therefore, the peak observed at 58.0 ppm must correspond to the cobalt cubane cluster. This value was used as a reference for the region where the chemical shift for cluster **11** might be observed. A sample of the crude oil product was dissolved in $CD_2Cl_2$ and analyzed via NMR spectroscopy. As with cluster **5**, two phosphorus shifts were observed (Figure 2.17). The first and significantly more intense shift occurs at $\delta$ = 12.4 ppm and is in agreement with that obtained for synthesized 4-(diisopropylphosphino)benzaldehyde (**10**) ($\delta$ = 12.0 ppm). The small remaining peak at $\delta$

= 67.5 ppm exists in a similar region as the shift corresponding to the terminal phosphine ligands within **5**. This data suggests that cluster **11** may be forming in very small quantities over the course of the two-day reaction.

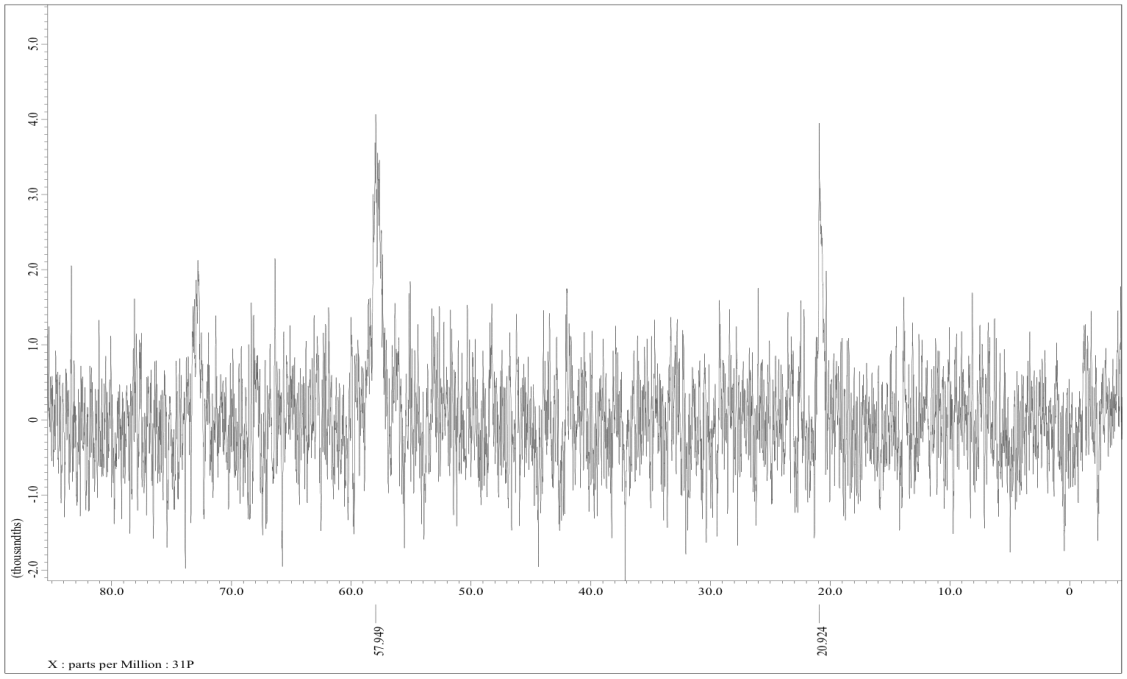


Figure 2.16. $^{31}$P NMR spectrum of cluster **5**.

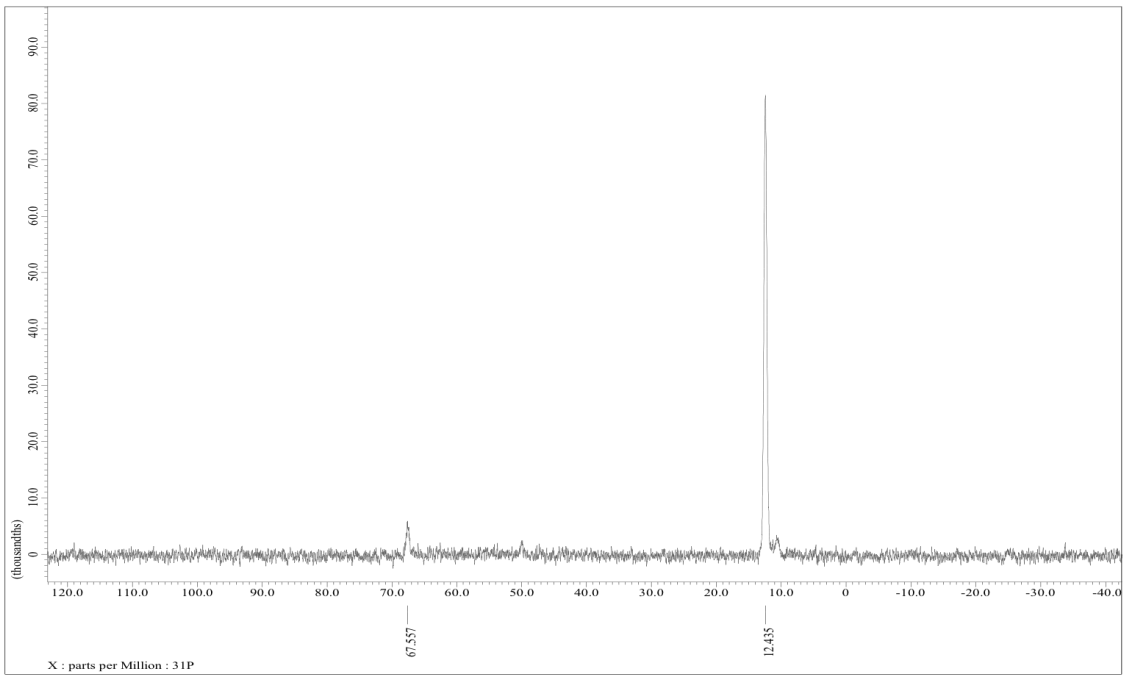


Figure 2.17. $^{31}$P NMR spectrum of b) crude product of cluster **11** reaction.

## 2.3 Experimental Details

### 2.3.1 General Considerations

Ligand precursors were used as obtained from the following: 4,5-dibromoveratrole (Alfa Aesar, 98+%), n-butyllithium (n-BuLi) (Sigma-Aldrich, ~1.6 M in hexanes), chlorodiphenylphosphine ($ClPPh_2$) (Sigma-Aldrich, 99%), 2-(4-bromophenyl)-1,3-dioxolane (Acros Organics, >98.0%), chlorodiisopropylphosphine ($ClPPr^i_3$) (Sigma-Aldrich, 99%), and *p*-toluenesulfonic acid monohydrate (Acros Organics, 99.8%). Molybdenum cluster precursor $(NH_4)_2[Mo_3S_{13}]$ was used as synthesized (described previously).[84] Anhydrous cobalt(II) chloride ($CoCl_2$) (99+%) was used as obtained from Strem and bis(trimethylsilyl)sulfide (98%) was purchased from Alfa Aesar.

Solvents were obtained from commercial suppliers and purified before use. Tetrahydrofuran (THF), diethyl ether ($Et_2O$), and hexanes (all obtained from Fisher Scientific) were dried and purified via double column filtration under nitrogen working gas within an M-Braun MB-SPS-800 solvent purification system. Anhydrous acetonitrile (MeCN) (Sigma-Aldrich, 99.8%) was sparged ($N_2$), degassed (freeze-pump-thaw), and stored over molecular sieves (4 Å, beads 4-8 mesh, Sigma-Aldrich). Ethanol (KOPTEC, 95%) was used as purchased from VWR. All manipulations were performed under inert atmosphere using standard Schlenk techniques or nitrogen-filled glovebox (M-Braun UNIlab Pro SP workstation) unless otherwise stated.

Data for all compounds was collected on an Agilent Gemini diffractometer using mirror-monochromated Mo Kα radiation. Data collection, integration, scaling

(ABSPACK) and absorption correction (face-indexed Gaussian integration[74] or numeric analytical methods[75]) were performed in CrysAlisPro.[76] Structure solution was performed using ShelXT[77]. Subsequent refinement was performed by full-matrix least-squares on $F^2$ in ShelXL.[77] Olex2[79] was used for viewing and to prepare CIF files.[113]

NMR spectra were obtained in specified deuterated solvents on a JEOL 300 MHz instrument and analyzed using Delta software. $^1H$ spectra were referenced to tetramethylsilane; proton decoupled $^{31}P$ spectra were referenced to 85% $H_3PO_4$ as an external reference.

### 2.3.2 1,2-bis(diphenylphosphino)-4,5-dimethoxybenzene (**7**)

Procedural information for the stepwise synthesis of 1,2-bis(diphenylphosphino)-4,5-dimethoxybenzene was obtained from literature.[114] The starting material, 4,5-dibromoveratrole (2.96 g, 10 mmol), was dissolved in 10:1 $Et_2O$/THF (110 mL) and cooled to -100 °C ($LN_2$/IPA). A 1.6 M solution of n-BuLi in hexanes (6.25 mL, 10 mmol) was slowly added to the reaction flask over 15 minutes. The resulting white suspension was stirred at -100 °C for 1 hour before a solution of $ClPPh_2$ (1.8 mL, 10 mmol) in $Et_2O$ (10 mL) was added over 5 minutes. The reaction mixture was stirred while warming to room temperature overnight. The work-up involved exposing the mixture to air and removing all solvent under vacuum to yield an off-white residue. The product was extracted with boiling EtOH and long white crystals were obtained as the solution cooled to room temperature.

The white crystalline product (2.90 g, 7.2 mmol) was dissolved in $Et_2O$ (100 mL) and the resulting solution was cooled to 0 °C (ice water) before n-BuLi (1.6 M in hexanes, 4.52 mL, 7.2 mmol) was slowly added. The resulting white suspension was

stirred at 0 °C for 1 hour. This temperature was maintained as a solution of $ClPPh_2$ (1.59 g, 7.2 mmol) in $Et_2O$ (10 mL) was added. The pale yellow suspension was stirred as it warmed to room temperature overnight. The production mixture was exposed to air before all volatiles were removed under vacuum to yield a pale yellow paste. Extraction with boiling EtOH and subsequent gradual cooling to room temperature allowed isolation of **7** as an off-white crystalline solid (2.66 g, 73%). $^1$H NMR ($C_6D_6$) δ 7.36 (m, 8H), 6.99 (m, 12H), 6.77 (m, 2H), 3.14 (s, 6H). $^{31}$P NMR ($C_6D_6$) δ -12.9 (s).

### 2.3.3 $Mo_3S_5(dppBzOMe)_3$ (**8**)

Literature procedure was adapted for the synthesis of **8**.[43] The red molybdenum precursor, $(NH_4)_2[Mo_3S_{13}]$ (0.126 g, 0.18 mmol), was suspended in THF (20 mL) before **7** (1.0 g, 1.2 mmol) was added. The resulting deep red suspension was allowed to stir for 1 day to yield a dark brown solution. The solution was filtered and the cluster was recrystallized from 2:1 THF/hexanes. $^{31}$P NMR ($CD_2Cl_2$) δ -16.9 (s). MALDI MS m/z 1967.3.

### 2.3.4 (4-(1,3-Dioxolan-2-yl)phenyldiisopropylphosphine (**9**)

2-(4-Bromophenyl)-1,3-dioxolane (1.0 g, 4.4 mmol) was dissolved in THF (15 mL) and cooled to -78 °C before a solution of n-butyllithium in hexanes (1.6 M, 3.02 mL, 4.8 mmol) was added dropwise. The reaction temperature was maintained at -78 °C while the mixture stirred for one hour. A solution of chlorodiisopropylphosphine ($ClPPr^i_2$) (0.705 g, 4.6 mmol) in THF (10 mL) added in to the reaction flask over five minutes. The pale-yellow solution was allowed to slowly warm to room temperature while stirring overnight. The organic product was washed with sparged ($N_2$) deionized water (2 x 10

mL) and brine (15 mL). The aqueous layer was extracted with anhydrous dicholomethane (20 mL) before the combined organic layer was dried over $MgSO_4$ and filtered through a Schlenk filter. Solvent was removed under high vacuum to yield a pale-yellow oil (0.73 g, 73%).$^{1}$H NMR ($(CD_3)_2O$) δ 7.49 (m, 4H), 5.74 (s, 1H), 4.08 (m, 4H), 2.14 (dsept, 2H), 1.04 (dd, 6H), 0.89 (dd, 6H). $^{31}$P NMR ($(CD_3)_2O$) δ 10.6 (s).

2.3.5 4-(diisopropylphosphino)benzaldehyde (**10**)

Ligand **9** (0.731 g, 2.7 mmol) was dissolved in anhydrous THF (10 mL). The resulting pale yellow solution was added to a reaction flask containing a solution of *p*-toluenesulfonic acid (PTSA) (16.0 mg, 0.09 mmol) in sparged ($N_2$) deoinized water via needle and syringe. The mixture was refluxed until the reaction was determined to be complete by TLC and NMR analysis (8 hours).

The yellow reaction mixture was allowed to cool to room temperature and the solvent volume was reduced to 8 mL under vacuum. Deionized water (3 mL) was added to the reaction flask to dilute the reaction mixture before it was extracted with $Et_2O$ (20 mL) under inert atmosphere. The organic layer was dried over $MgSO_4$ and filtered through a Schlenk filter. Solvent was removed from the filtrate under high vacuum to resulting in isolation of **10** as a yellow oil (0.44 g, 74%). $^{1}$H NMR ($(CD_3)_2O$) δ 10.06 (s, 1H), 7.89 (m, 2H), 7.71 (m, 2H), 2.20 (dsept, 2H), 1.09 (dd, 6H), 0.89 (dd, 6H). $^{31}$P NMR ($(CD_3)_2O$) δ 12.0 (s).

2.3.6 $Co_4S_4(P(Pr^i)_2(C_6H_4CHO))_4$ (**11**)

$CoCl_2$ (0.129 g, 1.0 mmol) was suspended in THF (10 mL) with **10** (0.441 g, 2.0 mmol). A solution of $(Me_3Si)_2S$ in THF (5 mL) was added to the reaction flask, causing the suspension to quickly darken from bright blue to black. The reaction mixture was allowed to stir for two days. Solvent was removed under high vacuum to yield a black oil. $^{31}P$ NMR ($CD_2Cl_2$) δ 67.5 (s).

## 2.4 Conclusions

### 2.4.1 Conclusions

While this project is still in its early stages, progress has been made toward metal chalcogenide cluster functionalization for SBUs in hybrid organic frameworks. Existing procedures by Tsuge *et al*. were employed to prepare cluster **8**.[43] The redox active cluster has been designed to incorporate ether protected, chelating phosphine catechol ligands around the known $Mo_3S_5$ metal chalcogenide core. The successful synthesis of cluster **8** has been confirmed via SCXRD structural analysis. The cluster contains a molybdenum trimer core with three doubly bridging sulfide ligands in the trimer plane and two triply bridging sulfide ligands 180º apart, centered above and below the trigular molybdenum core. Furthermore, the cluster contains three protected catechol ligands (**7**) with the methoxybenzene ring nearly orthogonal to the Mo atom trimer. NMR experiments corroborate the formation of cluster **8** but also include starting material (**7**) and side product impurities.

Additionally, a derivative of the reported cobalt cubane cluster (**5**) has been designed for use in cluster organic frameworks. This cluster was functionalized through inclusion of phosphine ligands containing both triisopropyl and benzaldehyde moities to provide the steric bulk required to isolate the cubane core in cluster **11**. Although formation of a product species has been confirmed using NMR spectroscopy, data indicates that the reaction progress was minimal under the attempted synthetic conditions.

### 2.4.2 Future Work

Continuing work is immediately focused on optimization of the recrystallization conditions for cluster **8**. Numerous solvent ratios have been explored, though few have

proven more successful than the currently used THF/hexanes method. Attempts have also been made to move forward to catechol deprotection using the crude product. Trimethylsilyl iodide was initially employed to cleave the methyl substituents but proved to be too mild based on NMR spectral data. Boron tribromide ($BBr_3$) has also been used as an dealkylating agent for the aryl methyl ethers of cluster **8**. Preliminary experiments indicate the formation of multiple products ($^{31}P$ NMR), presumably due, in part, to the impure cluster starting material. However, synthesis of the deprotected cluster could not be confirmed via matrix assisted laser desorption ionization mass spectrometry (MALDI MS). Efforts to recrystallize the crude dealkylated cluster product have been met with little success due to low product solubility.

Isolation of cluster **11** is also a continuing priority. Future attempts to synthesize the functionalized cobalt cubane will involve heating the reaction to improve product yield as well as increasing the reaction duration. Furthermore, cobalt cubane clusters containing selenide capping ligands and stabilized with $PPh_3$ ligands have been reported. Work is currently being done to obtain the sulfide capped analogue, $Co_4S_4(PPh_3)_4$. Successful isolation will determine whether triphenylphosphine stabilized cubane clusters will serve as a viable platform for designing (diphenylphosphino)benzaldehyde functionalized clusters as SBUs for cluster organic frameworks with imine linkages.

The long-term goals of this work are to synthesize 2D and 3D frameworks from the designed SBUs. This is contingent upon successful isolation of functionalized clusters. However, frameworks with covalent linkages are often difficult to obtain due to the crystallization problem often confronted with organic precursors. The conditions for framework crystallization must be determined such that the reaction is sufficiently

reversible. This enables dynamic correction of synthetic errors and leads to more pristine frameworks. Therefore, optimization of the crystallization conditions will prove to be a time-consuming process.

Furthermore, most of the reported MOF and COF synthetic methods require the use of high temperature and aqueous media. The sensitivity of the proposed SBUs has yet to be explored and the high temperature, acid catalyzed reaction may prove to be detrimental to metal chalcogenide cluster stability. These existing methodologies will be explored. However, Dichtel and coworkers recently introduced a low temperature alternative that utilizes metal triflates as catalysts for framework formation. These complexes have proven to be excellent catalysts for a range of COFs due to their excellent water tolerance and high efficiency for mediating imine formation.[115] This method has been shown to produce highly crystalline frameworks at room temperature in as little as 10 minutes. Thus, it may provide the best option for framework formation from potentially chemically sensitive precursors.

REFERENCES


1. Tomalia, D. A.; Khanna, S. N. *Chem. Rev.* **2016**, *116*, 2705–2774.

2. Murray, Christopher B.; Kagan; C. R.; Bawendi, M. G. *Annu. Rev. Mater. Sci.* **2000**, *30*, 545–610.

3. Kannan, R. M.; Nance, E.; Kannan, S.; Tomalia, D. A. *J. Intern. Med.* **2014**, *276*, 579–617.

4. Cademartiri, L.; Bishop, K. J. M.; Snyder, P. W.; Ozin, G. A. *Philos. Trans. R. Soc. A Math. Phys. Eng. Sci.* **2012**, *370*, 2824–2847.

5. Shevchenko, E. V.; Talapin, D. V.; Kotov, N. A.; O'Brien, S.; Murray, C. B. *Nature* **2006**, *439*, 55–59.

6. Woodcock, L. V. *Nature*. 1997, pp 141–143.

7. Wong, S.; Kitaev, V.; Ozin, G. A. *J. Am. Chem. Soc.* **2003**, *125*, 15589–15598.

8. Zhang, H.; Banfield, J. F. *CrystEngComm* **2014**, *16*, 1568–1578.

9. Steigerwald, M. L. *Polyhedron* **1994**, *13*, 1245–1252.

10. Lin, Z.; Williams, I. D. *Polyhedron* **1996**, *15*, 3277–3287.

11. Claridge, S. A.; Castleman, A. W.; Khanna, S. N.; Murray, C. B.; Sen, A.; Weiss, P. S. *ACS Nano* **2009**, *3*, 244–255.

12. Cademartiri, L.; Kitaev, V. *Nanoscale* **2011**, *3*, 3435–3446.

13. Ahmed, E.; Ruck, M.; Mccarley, a X. D. K. E.; Holliday, K.; Urry, G.; Wartik, T.; Moore, E.; Schlesinger, H. I.; Massey, A. G.; Urch, S.; Holliday, K.; Franolic, J.; Long, J. R. J. J. R.; Holm, R.; Kolesnichenko, V.; Messerle, L.; Bettentrup, H.; Welch, E. J.; Crawford, N. R. M.; Bergman, R. G.; Long, J. R. J. J. R.; Hay, D. N. T.; Swenson, D. C.; Messerle, L.; Welch, E. J.; Long, J. R. J. J. R.; Ströbele, M.; Eichele, K.; Meyer, H.; Mos, A.; Stro, M.; Eichele, K.; Meyer, H. *Inorg. Chem.* **2011**, *125*, 3660–3663.

14. Reber, A. C.; Khanna, S. N. *Acc. Chem. Res.* **2017**, *50*, 255–263.

15. Chauhan, V.; Reber, A. C.; Khanna, S. N. *J. Am. Chem. Soc.* **2017**, *139*, 1871–1877.

16. Champsaur, A. M.; Velian, A.; Paley, D. W.; Choi, B.; Roy, X.; Steigerwald, M. L.; Nuckolls, C. *Nano Lett.* **2016**, *16*, 5273–5277.

17. Roy, X.; Lee, C.-H.; Crowther, A. C.; Schenck, C. L.; Besara, T.; Lalancette, R. a; Siegrist, T.; Stephens, P. W.; Brus, L. E.; Kim, P.; Steigerwald, M. L.; Nuckolls, C. *Science* **2013**, *341*, 157–160.

18. Lee, C.; Liu, L.; Bejger, C.; Turkiewicz, A.; Goko, T.; Arguello, C. J.; Frandsen, B. A.; Cheung, S. C.; Medina, T.; Munsie, T. J. S.; D'Ortenzio, R.; Luke, G. M.; Besara, T.; Lalancette, R. A.; Siegrist, T.; Stephens, P. W.; Crowther, A. C.; Brus, L. E.; Matsuo, Y.; Nakamura, E.; Uemura, Y. J.; Kim, P.; Nuckolls, C.; Steigerwald, M. L.; Roy, X. *J. Am. Chem. Soc.* **2014**, 8–13.

19. Chauhan, V.; Sahoo, S.; Khanna, S. N. *J. Am. Chem. Soc.* **2016**, *138*, 1916–1921.

20. Ong, W. L.; O'Brien, E.; Dougherty, P. S. M.; Paley, D.; Higgs, C. F. I.; McGaughey, H., A. J.; Malen, A. J.; Roy, X. *Nat. Mater.* **2016**, *16*, 83–88.

21. Schulz-Dobrick, M.; Jansen, M. *CrystEngComm* **2008**, *10*, 661–664.

22. Gruber, F.; Schulz-Dobrick, M.; Jansen, M. *Chem. Eur. J.* **2010**, *16*, 1464–1469.

23. Gruber, F.; Jansen, M. *Angew. Chem. Int. Ed.* **2010**, *49*, 4924–4926.

24. Schulz-Dobrick, M.; Jansen, M. *Inorg. Chem.* **2007**, *46*, 4380–4382.

25. Schulz-Dobrick, M.; Jansen, M. *Eur. J. Inorg. Chem.* **2006**, *22*, 4498–4502.

26. Schmid, G. *Angew. Chem. Int. Ed.* **2008**, *47*, 3496–3498.

27. Turkiewicz, A.; Paley, D. W.; Besara, T.; Elbaz, G.; Pinkard, A.; Siegrist, T.; Roy, X. *J. Am. Chem. Soc.* **2014**, *136*, 15873–15876.

28. Turkiewicz, A.; Paley, D. W.; Besara, T.; Elbaz, G.; Pinkard, A.; Siegrist, T.; Roy, X. *J. Am. Chem. Soc.* **2014**, *136*, 15873–15876.

29. Schulz-Dobrick, M.; Jansen, M. *Angew. Chem. Int. Ed.* **2008**, *47*, 2256–2259.

30. Konarev, D. V; Troyanov, S. I.; Otsuka, A.; Yamochi, H.; Saito, G.; Lyubovskaya, R. N. *Dalt. Trans.* **2016**, *45*.

31. Barnes, J. C.; Dale, E. J.; Prokofjevs, A.; Narayanan, A.; Gibbs-Hall, I. C.; Juríček, M.; Stern, C. L.; Sarjeant, A. a.; Botros, Y. Y.; Stupp, S. I.; Stoddart, J. F. *J. Am. Chem. Soc.* **2015**, *137*, 2392–2399.

32. Reed, C. A.; Bolskar, R. D. *Chem. Rev.* **2000**, *100*, 1075–1120.

33. Xie, Q.; Perez-Cordero, E.; Echegoyen, L. *J. Am. Chem. Soc.* **1992**, *114*, 3978–3980.

34. Gunnarsson, O. *Rev. Mod. Phys.* **1997**, *69*, 575–606.

35. Iwasa, Y.; Hayashi, H.; Furudate, T.; Mitani, T. *J. Phys. Chem. Solids* **1996**, *54*, 579–585.

36. Schilder, A.; Bietsch, W.; Schwoerer, M. *New J. Phys.* **1999**, *1*, 1–11.

37. Tanaka, K.; Okahara, K.; Yamabe, T.; Yakushi, K.; Kikuchi, K.; Ikemoto, I.; Achiba, Y. *Phys. Rev. B* **1993**, *47*, 7554–7559.

38. Suzuki, A.; Suzuki, T.; Whitehead, R. J.; Maruyama, Y. *Chem. Phys. Lett.* **1994**, *223*, 517–520.

39. Konarev, D. V.; Khasanov, S. S.; Otsuka, A.; Maesato, M.; Saito, G.; Lyubovskaya, R. N. *Angew. Chem. Int. Ed.* **2010**, *49*, 4829–4832.

40. Morgenstern, D. A.; Ferrence, G. M.; Washington, J.; Henderson, J. I.; Rosenhein, L.; Heise, J. D.; Fanwisk, P. E.; Kubiak, C. P. *J. Am. Chem. Soc.* **1996**, *118*, 2198–2207.

41. Ferrence, G. M.; Fanwick, P. E.; Kubiak, C. P. *Chem. Commun.* **1996**, 1575–1576.

42. Deng, L.; Bill, E.; Wieghardt, K.; Holm, R. H. *J. Am. Chem. Soc.* **2009**, *131*, 11213–11221.

43. Tsuge, K.; Imoto, H.; Saito, T. *Inorg. Chem.* **1995**, *34*, 3404–3409.

44. Miiller, T. E.; Kensington, S. *Transit. Met. Chem* **1995**, *539*, 533–539.

45. Tolman, C. A. *Chem. Rev.* **1977**, *77*, 313–348.

46. Cao, J.; Yan, X.; He, W.; Li, X.; Li, Z.; Mo, Y.; Liu, M.; Jiang, Y.-B. *J. Am. Chem. Soc.* **2017**, in press.

47. Prasanna, M. D.; Guru Row, T. N. *Cryst. Eng.* **2000**, *3*, 135–154.

48. Cavallo, G.; Metrangolo, P.; Milani, R.; Pilati, T.; Priimagi, A.; Resnati, G.; Terraneo, G. *Chem. Rev.* **2016**, *116*, 2478–2601.

49. Zingaro, R. A.; Steeves, B. H.; Irgolic, K. *J. Organomet. Chem.* **1965**, *4*, 320–323.

50. Wang, W.; Ji, B.; Zhang, Y. *J. Phys. Chem. A* **2009**, *113*, 8132–8135.

51. Ho, P. C.; Szydlowski, P.; Sinclair, J.; Elder, P. J. W.; Kübel, J.; Gendy, C.; Lee, L. M.; Jenkins, H.; Britten, J. F.; Morim, D. R.; Vargas-Baca, I. *Nat. Commun.* **2016**, *7*, 1–10.

52. Fanfrlík, J.; Přáda, A.; Padělková, Z.; Pecina, A.; Macháček, J.; Lepšík, M.; Holub, J.; Růžička, A.; Hnyk, D.; Hobza, P. *Angew. Chem. Int. Ed.* **2014**, *53*, 10139–10142.

53. Garrett, G. E.; Gibson, G. L.; Straus, R. N.; Seferos, D. S.; Taylor, M. S. *J. Am. Chem. Soc.* **2015**, *137*, 4126–4133.

54. Benz, S.; Macchione, M.; Verolet, Q.; Mareda, J.; Sakai, N.; Matile, S. *J. Am. Chem. Soc.* **2016**, *138*, 9093–9096.

55. Garrett, G. E.; Carrera, E. I.; Seferos, D. S.; Taylor, M. S. *Chem. Commun.* **2016**, *52*, 9881–9884.

56. Lim, J. Y. C.; Marques, I.; Thompson, A. L.; Christensen, K. E.; Felix, V.; Beer, P. D. *J. Am. Chem. Soc.* **2017**, *139*, 3122–3133.

57. Konarev, D. V; Khasanov, S. S.; Simonov, S. V; Yudanova, E. I.; Lyubovskaya, R. N. *CrystEngComm* **2009**, *12*, 3542–3546.

58. Konarev, D. V.; Kuzmin, A. V.; Simonov, S. V.; Khasanov, S. S.; Otsuka, A.; Yamochi, H.; Saito, G.; Lyubovskaya, R. N. *Dalton Trans.* **2012**, *41*, 13841–13847.

59. Konarev, D.V.; Khasanov, S. S.; Otsuka, A.;Yamochi, H.; Saito, G.; Lyubovskaya, R. N. *Inorg. Chem.* **2012**, *51*, 3420–3426.

60. Harris, A. R.; Neufeld, A. K.; O 'mullane, A. P.; Bond, A. M.; Morrison, R. J. S. *J. Electrochem. Soc.* **2005**, *152*, C577–C583.

61. Melby, L. R.; Harder, R. J.; Hertler, W. R.; Mahler, W.; Benson, R. E.; Mochel, W. E. *J. Am. Chem. Soc.* **1962**, *84*, 3374–3387.

62. Form, S.; Kistenmacher, B. Y. T. J.; Emge, T. J.; Blocht, A. N.; Cowan, D. O. *Acta Cryst.* **1982**, *B38*, 1193–1199.

63. Martín, N.; Segura, J. L.; Seoane, C. *J. Mater. Chem.* **1997**, *7*, 1661–1676.

64. Ward, M. D.; Johnson, D. C. *Inorg. Chem.* **1987**, *26*, 4213–4227.

65. Wudl, F.; Bryce, M. R. *J. Chem. Educ.* **1990**, *67*, 717.

66. Sun, L.; Hendon, C. H.; Minier, M. A.; Walsh, A.; Dincă, M. *J. Am. Chem. Soc.* **2015**, *137*, 6164–6167.

67. Takenobu, T.; Chi, D. H.; Margadonna, S.; Prassides, K.; Kubozono, Y.; Fitch, A. N.; Kato, K. ichi; Iwasa, Y. *J. Am. Chem. Soc.* **2003**, *125*, 1897–1904.

68. Maruyama, Y.; Motohashi, S.; Suzuki, K.; Takagi, S.; Ogata, H. *Solid State Commun.* **2000**, *115*, 457–462.

69. Poulten, R. C.; Page, M. J.; Algarra, A. G.; Le Roy, J. J.; López, I.; Carter, E.; Llobet, A.; Macgregor, S. a; Mahon, M. F.; Murphy, D. M.; Murugesu, M.; Whittlesey, M. K. *J. Am. Chem. Soc.* **2013**, *135*, 13640–13643.

70. Holland, P. L.; Cundari, T. R.; Perez, L. L.; Eckert, N. A.; Lachicotte, R. J. *J. Am. Chem. Soc.* **2002**, *124*, 14416–14424.

71. Baker-Hawkes, M. J.; Billig, E.; Gray, H. B. *J. Am. Chem. Soc.* **1966**, *88*, 4870–4875.

72. Burstall, F. H.; Nyholm, R. S. *J. Chem. Soc.* **1952**, 3570–3579.

73. Lever, A. B. P. *Inorg. Chem.* **1965**, *33*, 10–11.

74. Blanc, E.; Schwarzenbach, D.; Flack, H. D. *J. Appl. Cryst.* **1991**, *24*, 1035–1041.

75. Clark, R. C.; Reid, J. S. *Acta Cryst.* **1995**, *51*, 887–897.

76. Version 1.171.37.35 (2014). Oxford Diffraction /Agilent Technologies UK Ltd, Yarnton, England.

77. Sheldrick, G. M. *Acta Cryst.* **2015**, *71*, 3–8.

78. Palatinus, L.; Chapuis, G. *J. Appl. Cryst.* **2007**, *40*, 786–790.

79. Dolomanov, O. V.; Bourhis, L. J.; Gildea, R. J.; Howard, J. A. K.; Puschmann, H. *J. Appl. Cryst.* **2009**, *42*, 339–341.

80. Guzei, I. A. *J. Appl. Cryst.* **2014**, *47*, 806–809.

81. Copp, S. B.; Holman, K. T.; Sangster, J. O. S.; Subramanian, S.; Zaworotko, M. J. *J. Chem. Soc., Dalt. Trans.* **1995**, No. 13, 2233–2243.

82. Ghiassi, K. B.; Wescott, J.; Chen, S. Y.; Balch, A. L.; Olmstead, M. M. *Cryst. Growth Des.* **2015**, *15*, 2480–2485.

83. O'Brien, E.; Paley, D.; Roy, X. Unpublished work.

84. Muller, A.; Krickemeyer, E. *Inorg. Synth.* **2016**, *27*, 47–58.

85. Matsumoto, K.; Saiga, N.; Tanaka, S.; Ooi, S. *J. Chem. Soc., Dalt. Trans.* **1991**, 1265–1271.

86. Cecconi, F.; Ghilardi, C. A.; Midollini, S.; Orlandini, A.; Vacca, A.; Ramirez, J. A. *J. Chem. Soc., Dalt. Trans.* **1990**, 773–779.

87. Silva, P.; Vilela, S. M. F.; Tome, J. P. C.; Almeida Paz, F. A. *Chem. Soc. Rev.* **2015**, *44*, 6774–6803.

88. Li, M.; Li, D.; O'Keeffe, M.; Yaghi, O. M. *Chem. Rev.* **2014**, *114*, 1343–1370.

89. Li, H.; Eddaoudi, M.; O'Keeffe, M.; Yaghi, O. M. *Nature* **1999**, *402*, 276–279.

90. Gándara, F.; Furukawa, H.; Lee, S.; Yaghi, O. M. *J. Am. Chem. Soc.* **2014**, *136*, 5271–5274.

91. Galli, S.; Masciocchi, N.; Colombo, V.; Maspero, A.; Palmisano, G.; López-Garzón, F. J.; Domingo-Garcia, M.; Fernández-Morales, I.; Barea, E.; Navarro, J. A. R. *Chem. Mater.* **2010**, *22*, 1664–1672.

92. Mulfort, K. L.; Farha, O. K.; Stern, C. L.; Sarjeant, A. A.; Hupp, J. T. *J. Am. Chem. Soc.* **2009**, *131*, 3866–3868.

93. Chen, Y. Z.; Xu, Q.; Yu, S. H.; Jiang, H. L. *Small* **2014**, *11*, 71–76.

94. Ockwig, N. W.; Cote, A. P.; Keeffe, M. O.; Matzger, A. J.; Yaghi, O. M. *Science* **2005**, *310*, 1166–1171.

95. Ding, S.-Y.; Wang, W. *Chem. Soc. Rev* **2013**, *42*, 548–568.

96. El-Kaderi, H. M.; Hunt, J. R.; Mendoza-Cortes, J. L.; Cote, A. P.; Taylor, R. E.; O'Keeffee, M.; Yaghi, O. M. *Science* **2007**, *316*, 268–273.

97. Uribe-Romo, F. J.; Hunt, J. R.; Furukawa, H.; Klo, C.; Keeffe, M. O.; Yaghi, O. M. *J. Am. Chem. Soc.* **2009**, *131*, 4570–4571.

98. Wan, S.; Guo, J.; Kim, J.; Ihee, H.; Jiang, D. *Angew. Chem. Int. Ed.* **2008**, *47*, 8826–8830.

99. Wan, S.; Gandara, F.; Asano, A.; Furukawa, H.; Saeki, A.; Dey, S. K.; Liao, L.; Ambrogio, M. W.; Botros, Y. Y.; Duan, X.; Seki, S.; Stoddart, J. F.; Yaghi, O. M. *Chem. Mater.* **2011**, *23*, 4094–4097.

100. Ding, S.-Y.; Gao, J.; Wang, Q.; Zhang, Y.; Song, W.-G.; Su, C.-Y.; Wang, W. *J. Am. Chem. Soc.* **2011**, *133*, 19816–19822.

101. Service, R. F. *Science* **2009**, *324*, 875–877.

102. Miro, P.; Audiffred, M.; Heine, T. *Chem. Soc. Rev.* **2014**, *43*, 6537–6554.

103. Novoselov, K. S.; Fal, V. I.; Colombo, L.; Gellert, P. R.; Schwab, M. G.; Kim, K.; Ko, V. I. F.; Colombo, L.; Gellert, P. R.; Schwab, M. G.; Kim, K. *Nature* **2013**, *490*, 192–200.

104. Pakdel, A.; Bando, Y.; Golberg, D. *Chem. Soc. Rev.* **2014**, *43*, 934–959.

105. Yamada-Takamura, Y.; Friedlein, R. *Sci. Technol. Adv. Mater.* **2014**, *15*, 1-12.

106. Daage, M.; Chianelli, R. R. *J. Catal.* **1994**, 149, 414–427.

107. Hilsenbeck, S. J.; McCarley, R. E.; Thompson, R. K.; Flanagan, L. C.; Schrader, G. L. *J. Mol. Catal. A Chem.* **1997**, *122*, 13–24.

108. McCarty, K. F.; Anderegg, J. W.; Schrader, G. L. *J. Catal.* **1985**, *93*, 375–387.

109. Maeda, H.; Sakamoto, R.; Nishihara, H. *Langmuir* **2016**, *32*, 2527–2538.

110. Kambe, T.; Sakamoto, R.; Hoshiko, K.; Takada, K.; Miyachi, M.; Ryu, J. H.; Sasaki, S.; Kim, J.; Nakazato, K.; Takata, M.; Nishihara, H. *J. Am. Chem. Soc.* **2013**, *135*, 2462–2465.

111. Gray, T. G. *Coord. Chem. Rev.* **2003**, *243*, 213–235.

112. Boardman, B. M.; Widawsky, J. R.; Park, Y. S.; Schenck, C. L.; Venkataraman, L.; Steigerwald, M. L.; Nuckolls, C. *J. Am. Chem. Soc.* **2011**, *133*, 8455–8457.

113. Dolomanov, O. V.; Bourhis, L. J.; Gildea, R. J.; Howard, J. A. K.; Puschmann, H. *J. Appl. Cryst.* **2009**, *42*, 339–341.

114. Chuong, R.; Luck, K. A.; Luck, R. L.; Nguyen, L. P.; Phan, D.; Pignotti, L. R.; Urnezius, E.; Valente, E. J. *J. Organomet. Chem.* **2013**, *724*, 45–50.

115. Matsumoto, M.; Dasari, R. R.; Ji, W.; Cameron, H.; Parker, T. C.; Marder, S. R.; Dichtel, W. R.; Matsumoto, M.; Dasari, R. R.; Ji, W.; Feriante, C. H.; Parker, T. C. *J. Am. Chem. Soc.* **2017**, *139*, 4999–5002.

# APPENDIX A: CYRSTAL DATA FOR **1**•$C_{60}$

Table 1 Crystal data and structure refinement for NS_CB_TCGN11_MO1_X1.

| | |
|---|---|
| Identification code | NS_CB_TCGN11_MO1_X1 |
| Empirical formula | $C_{160}H_{92}I_2Ni_3P_6$ |
| Formula weight | 2630.08 |
| Temperature/K | 100 |
| Crystal system | orthorhomic |
| Space group | *Pnma* |
| a/Å | 29.4642(7) |
| b/Å | 16.8278(5) |
| c/Å | 22.1966(5) |
| α/° | 90 |
| β/° | 90 |
| γ/° | 90 |
| Volume/Å$^3$ | 11005.5(5) |
| Z | 4 |
| $\rho_{calc}$g/cm$^3$ | 1.587 |
| μ/mm$^{-1}$ | 1.219 |
| Crystal size/mm$^3$ | 0.33 × 0.07 × 0.02 |
| Radiation | MoKα (λ = 0.71073 Å) |
| 2Θ range for data collection/° | 7, 53 |
| Index ranges | $-68 \leq h \leq 54$, $-16 \leq k \leq 21$, $-19 \leq l \leq 25$ |
| Reflections collected | 38573 |
| Independent reflections | 18653 [$R_{int}$ = 0.0377, $R_{sigma}$ = 0.0695] |
| Data/restraints/parameters | 11503/1572/1103 |
| Goodness-of-fit on $F^2$ | 1.124 |
| Final R indexes [all data] | $R_1$ = 0.0507, $wR_2$ = 0.0867 |
| Largest diff. peak/hole / e Å$^{-3}$ | 0.73, -0.48 |

# APPENDIX B: CYRSTAL DATA FOR **2**•$C_{60}$

Table 1: Crystal data and structure refinement for NS_CB_TE2_MO2_X3.

| | |
|---|---|
| Identification code | NS_CB_TE2_MO2_X3 |
| Empirical formula | $C_{160}H_{92}Te_2Ni_3P_6$ |
| Formula weight | 2631.48 |
| Temperature/K | 100 |
| Crystal system | orthorhombic |
| Space group | *Pnma* |
| a/Å | 29.4138(7) |
| b/Å | 16.8461(6) |
| c/Å | 22.2484(6) |
| α/° | 90 |
| β/° | 90 |
| γ/° | 90 |
| Volume/Å$^3$ | 11022.8(5) |
| Z | 4 |
| $\rho_{calc}$g/cm$^3$ | 1.585 |
| μ/mm$^{-1}$ | 1.175 |
| Crystal size/mm$^3$ | 0.33 × 0.06 × 0.02 |
| Radiation | MoKα (λ = 0.71073 Å) |
| 2Θ range for data collection/° | 7, 53 |
| Index ranges | $-28 \leq h \leq 39$, $-22 \leq k \leq 17$, $-29 \leq l \leq 21$ |
| Reflections collected | 42149 |
| Independent reflections | 12635 [$R_{int}$ = 0.0655, $R_{sigma}$ = 0.0785] |
| Data/restraints/parameters | 11421/1571/1103 |
| Goodness-of-fit on $F^2$ | 1.089 |
| Final R indexes [all data] | $R_1$ = 0.0466, $wR_2$ = 0.0885 |
| Largest diff. peak/hole / e Å$^{-3}$ | 0.58, -0.54 |

# APPENDIX C: CYRSTAL DATA FOR **1**•$C_{70}$

Table 1 Crystal data and structure refinement for NS_CB_NI3TE2X2_MO1_X1.

| | |
|---|---|
| Identification code | NS_CB_NI3TE2X2_MO1_X1 |
| Empirical formula | $C_{340}H_{184}I_4Ni_6P_{12}$ |
| Formula weight | 550.36 |
| Temperature/K | 100 |
| Crystal system | orthorhombic |
| Space group | *Pnma* |
| a/Å | 30.2143(7) |
| b/Å | 17.2268(5) |
| c/Å | 22.2347(6) |
| α/° | 90 |
| β/° | 90 |
| γ/° | 90 |
| Volume/Å$^3$ | 11573.1(5) |
| Z | 2 |
| $\rho_{calc}$g/cm$^3$ | 1.578 |
| μ/mm$^{-1}$ | 1.163 |
| Crystal size/mm$^3$ | 0.11 × 0.07 × 0.06 |
| Radiation | MoKα (λ = 0.71073 Å) |
| 2Θ range for data collection/° | 7, 52 |
| Index ranges | $-39 \leq h \leq 37$, $-21 \leq k \leq 23$, $-28 \leq l \leq 20$ |
| Reflections collected | 39192 |
| Independent reflections | 13018 [$R_{int}$ = 0.0789, $R_{sigma}$ = 0.1078] |
| Data/restraints/parameters | 11777/2850/1341 |
| Goodness-of-fit on F$^2$ | 1.007 |
| Final R indexes [all data] | $R_1$ = 0.0519, $wR_2$ = 0.1026 |
| Largest diff. peak/hole / e Å$^{-3}$ | 0.77, -0.49 |

# APPENDIX D: CYRSTAL DATA FOR **2**•$C_{70}$

Table 1 Crystal data and structure refinement for NS_CB_NI3TE2_MO1_X4.

| | |
|---|---|
| Identification code | NS_CB_NI3TE2_MO1_X4 |
| Empirical formula | $C_{340}H_{184}Te_4Ni_6P_{12}$ |
| Formula weight | 5503.16 |
| Temperature/K | 100 |
| Crystal system | orthorhombic |
| Space group | *Pnma* |
| a/Å | 29.8596(9) |
| b/Å | 17.1848(6) |
| c/Å | 22.4569(9) |
| α/° | 90 |
| β/° | 90 |
| γ/° | 90 |
| Volume/Å$^3$ | 11523.3(7) |
| Z | 2 |
| $\rho_{calc}$g/cm$^3$ | 1.586 |
| μ/mm$^{-1}$ | 1.128 |
| Crystal size/mm$^3$ | 0.17 × 0.08 × 0.06 |
| Radiation | MoKα (λ = 0.71073 Å) |
| 2Θ range for data collection/° | 7, 57 |
| Index ranges | $-29 \leq h \leq 39$, $-20 \leq k \leq 15$, $-28 \leq l \leq 23$ |
| Reflections collected | 42786 |
| Independent reflections | 13286 [$R_{int}$ = 0.3697, $R_{sigma}$ = 0.5270] |
| Data/restraints/parameters | 13017/2134/1330 |
| Goodness-of-fit on $F^2$ | 1.029 |
| Final R indexes [all data] | $R_1$ = 0.6719, $wR_2$ = 0.7638 |
| Largest diff. peak/hole / e Å$^{-3}$ | 1.07, -0.96 |

# APPENDIX E: CYRSTAL DATA FOR **3**•$C_{60}$

Table 1 Crystal data and structure refinement for NS_NI3SE2_MO1_X2.

| | |
|---|---|
| Identification code | NS_NI3SE2_MO1_X2 |
| Empirical formula | $C_{160}H_{92}Se_2Ni_3P_6$ |
| Formula weight | 2534.22 |
| Temperature/K | 101 |
| Crystal system | monoclinic |
| Space group | $P2_1/n$ |
| a/Å | 24.9814(13) |
| b/Å | 10.8019(4) |
| c/Å | 26.6428(1) |
| α/° | 90 |
| β/° | 110 |
| γ/° | 90 |
| Volume/$Å^3$ | 6723.6(5) |
| Z | 4 |
| $\rho_{calc}g/cm^3$ | 1.469 |
| $\mu/mm^{-1}$ | 2.100 |
| Crystal size/$mm^3$ | 0.08 × 0.11 × 0.22 |
| Radiation | MoKα (λ = 0.71073 Å) |
| 2Θ range for data collection/° | 7, 57 |
| Index ranges | $-30 \leq h \leq 32$, $-10 \leq k \leq 14$, $-35 \leq l \leq 27$ |
| Reflections collected | 36378 |
| Independent reflections | 14657 [$R_{int}$ = 0.0731, $R_{sigma}$ = 0.1122] |
| Data/restraints/parameters | 14657/0/775 |
| Goodness-of-fit on $F^2$ | 1.286 |
| Final R indexes [all data] | 1487.15 |
| Largest diff. peak/hole / e $Å^{-3}$ | 1.63, -2.24 |

# APPENDIX F: CYRSTAL DATA FOR **4**•$C_{60}$

Table 1 Crystal data and structure refinement for NS_CB_C60NI3S2_MO1_X1.

| | |
|---|---|
| Identification code | NS_CB_C60NI3S2_MO1_X1 |
| Empirical formula | $C_{160}H_{92}S_2Ni_3P_6$ |
| Formula weight | 2440.40 |
| Temperature/K | 103 |
| Crystal system | orthorhombic |
| Space group | Pnma |
| a/Å | 29.1353(2) |
| b/Å | 16.8540(1) |
| c/Å | 22.1191(1) |
| α/° | 90 |
| β/° | 90 |
| γ/° | 90 |
| Volume/Å$^3$ | 10861.5(1) |
| Z | 7 |
| $\rho_{calc}$g/cm$^3$ | 1.552 |
| μ/mm$^{-1}$ | 1.171 |
| Crystal size/mm$^3$ | 0.07 × 0.07 × 0.21 |
| Radiation | MoKα (λ = 0.71073 Å) |
| 2Θ range for data collection/° | 7, 57 |
| Index ranges | $-38 \leq h \leq 36$, $-22 \leq k \leq 16$, $-20 \leq l \leq 28$ |
| Reflections collected | 36022 |
| Independent reflections | 12193 [$R_{int}$ = 0.1259, $R_{sigma}$ = 0.1708] |
| Data/restraints/parameters | 12193/0/704 |
| Goodness-of-fit on $F^2$ | 1.462 |
| Final R indexes [all data] | $R_1$ = 0.2478, $wR_2$ = 0.4733 |
| Largest diff. peak/hole / e Å$^{-3}$ | 4.17, -1.05 |

# APPENDIX G: CYRSTAL DATA FOR **6**•$C_{60}$

Table 1 Crystal data and structure refinement for NS_CB_C60_MO2_X1.

| | |
|---|---|
| Identification code | NS_CB_C60_MO2_X1 |
| Empirical formula | $C_{78}H_{37}S_5Mo_3P_6$ |
| Formula weight | 1665.26 |
| Temperature/K | 100 |
| Crystal system | triclinic |
| Space group | $P\bar{1}$ |
| a/Å | 15.9995(1) |
| b/Å | 16.1388(1) |
| c/Å | 17.7019(1) |
| α/° | 99 |
| β/° | 111 |
| γ/° | 114 |
| Volume/Å$^3$ | 3585.7(5) |
| Z | 4 |
| $\rho_{calc}$g/cm$^3$ | 2.979 |
| μ/mm$^{-1}$ | 1.678 |
| Crystal size/mm$^3$ | 0.06 × 0.09 × 0.32 |
| Radiation | MoKα (λ = 0.71073 Å) |
| 2Θ range for data collection/° | 7, 57 |
| Index ranges | $-17 \le h \le 17$, $-16 \le k \le 19$, $-23 \le l \le 14$ |
| Reflections collected | 18365 |
| Independent reflections | 12292 [$R_{int}$ = 0.0527, $R_{sigma}$ = 0.0947] |
| Data/restraints/parameters | 12292/0/405 |
| Goodness-of-fit on F$^2$ | 1.214 |
| Final R indexes [all data] | $R_1$ = 0.1431, $wR_2$ = 0.3440 |
| Largest diff. peak/hole / e Å$^{-3}$ | 5.11, -5.66 |

# APPENDIX H: CYRSTAL DATA FOR **1**•TCNQ

Table 1 Crystal data and structure refinement for NS_CB_TCGN11_MO1_X1.

| | |
|---|---|
| Identification code | NS_CB_TCGN11_MO1_X1 |
| Empirical formula | $C_{87}H_4N_4I_2Ni_3P_2$ |
| Formula weight | 1786.74 |
| Temperature/K | 100 |
| Crystal system | monoclinic |
| Space group | C2/n |
| a/Å | 51.9158(11) |
| b/Å | 16.1091(3) |
| c/Å | 21.0634(3) |
| α/° | 90 |
| β/° | 96 |
| γ/° | 90 |
| Volume/Å$^3$ | 17504.1(6) |
| Z | 14 |
| $\rho_{calc}$g/cm$^3$ | 1.991 |
| μ/mm$^{-1}$ | 3.186 |
| Crystal size/mm$^3$ | 0.07 × 0.13 × 0.16 |
| Radiation | MoKα (λ = 0.71073 Å) |
| 2Θ range for data collection/° | 7, 57 |
| Index ranges | $-68 \leq h \leq 54$, $-16 \leq k \leq 21$, $-19 \leq l \leq 25$ |
| Reflections collected | 38573 |
| Independent reflections | 18653 [$R_{int}$ = 0.0377, $R_{sigma}$ = 0.0695] |
| Data/restraints/parameters | 18653/0/1392 |
| Goodness-of-fit on F$^2$ | 1.019 |
| Final R indexes [all data] | $R_1$ = 0.1119, $wR_2$ = 0.2392 |
| Largest diff. peak/hole / e Å$^{-3}$ | 2.72, -3.00 |

# APPENDIX I: CYRSTAL DATA FOR **8**

Table 1 Crystal data and structure refinement for TRIA3.

| | |
|---|---|
| Identification code | TRIA3 |
| Empirical formula | $C_{96}H_{84}O_6P_6S_5Mo_3$ |
| Formula weight | 1967.57 |
| Temperature/K | 101 |
| Crystal system | triclinic |
| Space group | $P\bar{1}$ |
| a/Å | 14.860(3) |
| b/Å | 14.8649(2) |
| c/Å | 25.393(3) |
| α/° | 85 |
| β/° | 82 |
| γ/° | 62 |
| Volume/Å$^3$ | 4922.7(12) |
| Z | 2 |
| $\rho_{calc}$g/cm$^3$ | 1.327 |
| μ/mm$^{-1}$ | 0.629 |
| Crystal size/mm$^3$ | 0.03 × 0.06 × 0.11 |
| Radiation | MoKα (λ = 0.71073 Å) |
| 2Θ range for data collection/° | 7, 57 |
| Index ranges | $-19 \leq h \leq 17$, $-18 \leq k \leq 19$, $-24 \leq l \leq 31$ |
| Reflections collected | 35082 |
| Independent reflections | 19205 [$R_{int}$ = 0.3839, $R_{sigma}$ = 0.8629] |
| Data/restraints/parameters | 19205/0/1099 |
| Goodness-of-fit on F$^2$ | 0.891 |
| Final R indexes [all data] | $R_1$ = 0.4834, $wR_2$ = 0.5486 |
| Largest diff. peak/hole / e Å$^{-3}$ | 4.06, -0.87 |

APPENDIX J: I-V CURVE FOR **1** and **1**•$C_{60}$

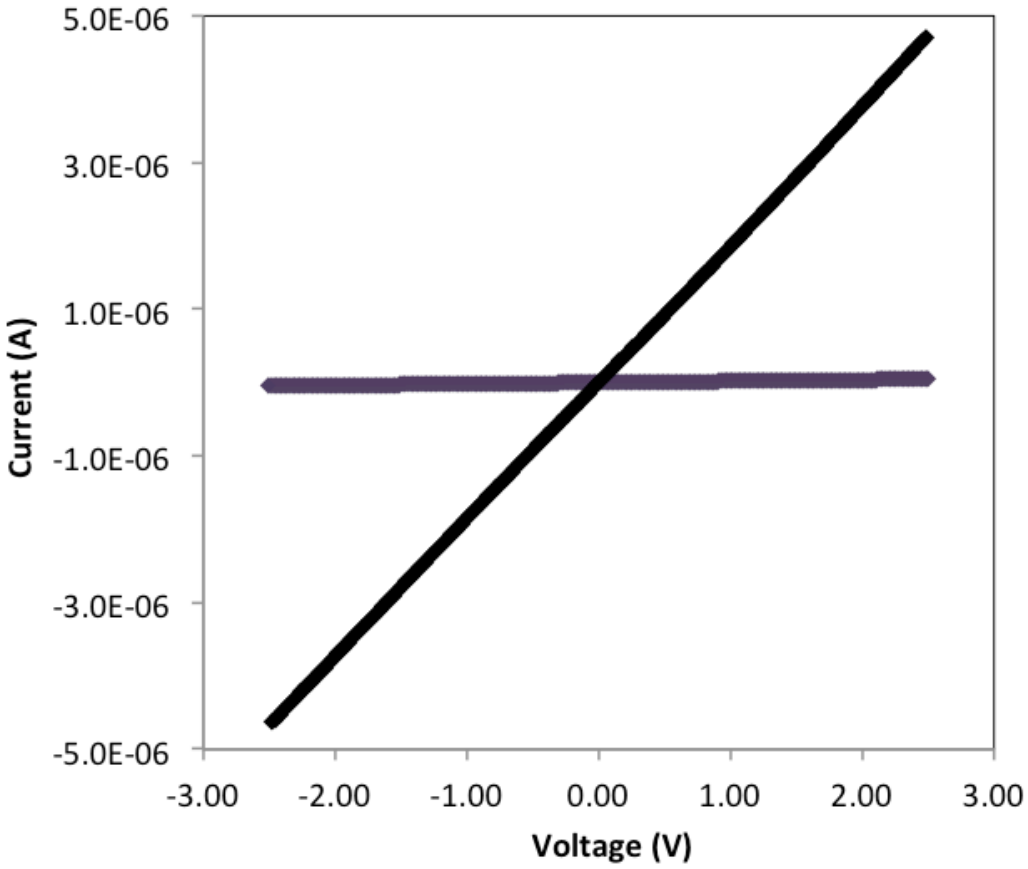

APPENDIX K: I-V CURVE FOR **2** and **2**•$C_{60}$

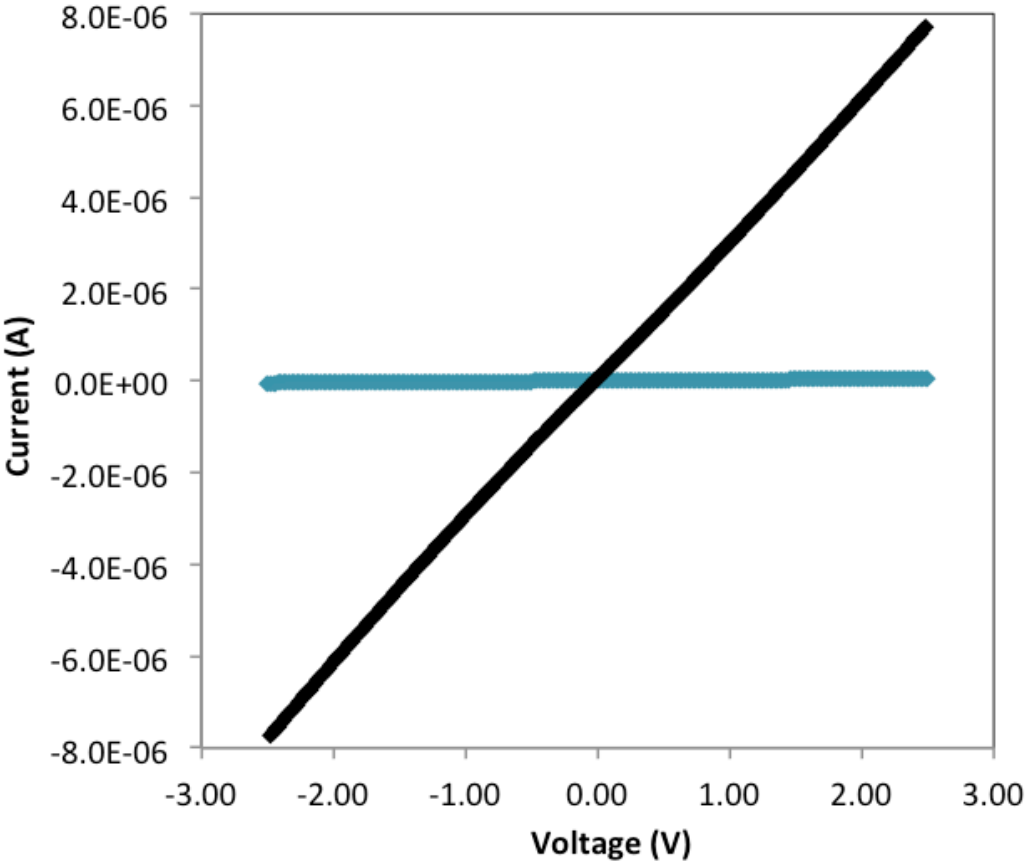

APPENDIX L: I-V CURVE FOR **1** and **1**•$C_{70}$

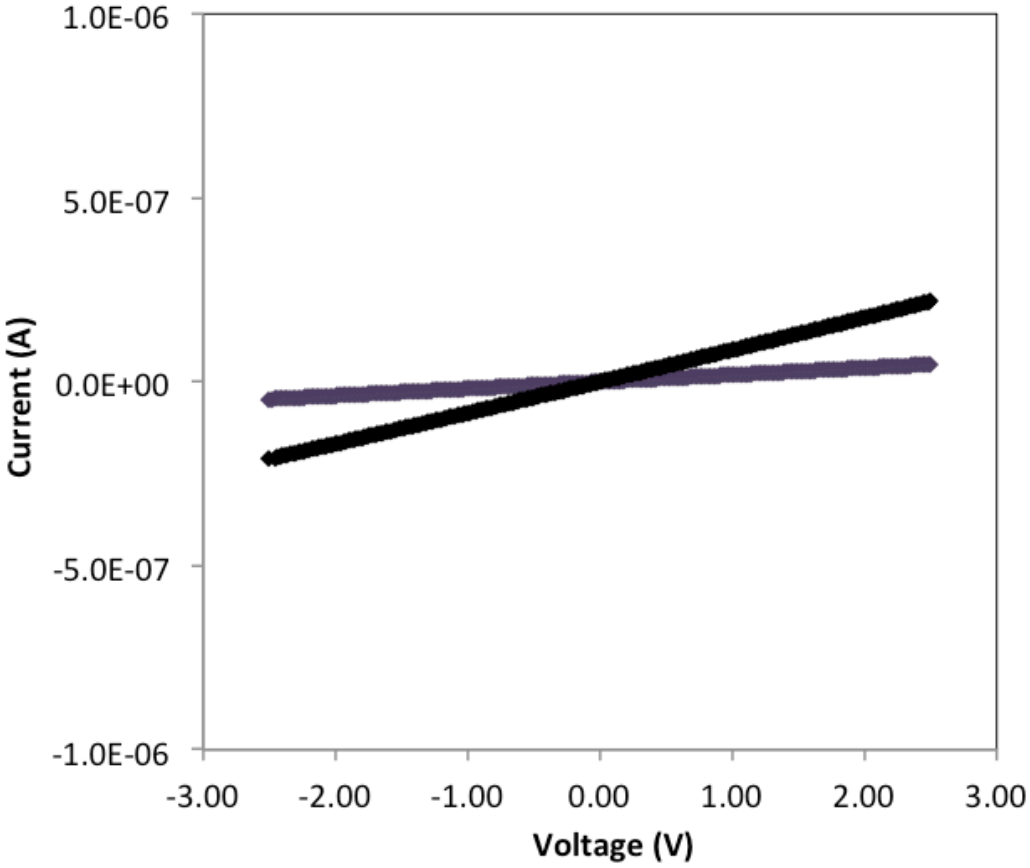

APPENDIX M: I-V CURVE FOR **2** and **2**•$C_{70}$